ISSN 2074-272X

науково-практичний журнал 2020/4

Електротехніка і Електромеханіка

Electrical Engineering & Electromechanics

Електричні машини та апарати
Електротехнічні комплекси та системи
Техніка сильних електричних та магнітних полів. Інженерна електрофізика
Електроізоляційна та кабельна техніка
Електричні станції, мережі і системи
Ювілеї

З 2015 р. журнал індексується у міжнародній наукометричній базі Web of Science Core Collection: Emerging Sources Citation Index

«ELECTRICAL ENGINEERING & ELECTROMECHANICS»

SCIENTIFIC & PRACTICAL JOURNAL
Journal was founded in 2002
Founders:
National Technical University «Kharkiv Polytechnic Institute» (Kharkiv, Ukraine)
State Institution «Institute of Technical Problems of Magnetism of the NAS of Ukraine» (Kharkiv, Ukraine)

INTERNATIONAL EDITORIAL BOARD

Sokol Ye.I.	**Editor-in-Chief**, Professor, Corresponding member of NAS of Ukraine, Rector of NTU "KhPI", Ukraine
Korytchenko K.V.	**Deputy Editor,** Professor, National Technical University "Kharkiv Polytechnic Institute" (NTU "KhPI"), Ukraine
Rozov V.Yu.	**Deputy Editor,** Professor, Corresponding member of NAS of Ukraine, Director of State Institution "Institute of Technical Problems of Magnetism of the NAS of Ukraine"(SI "ITPM NASU"), Kharkiv, Ukraine
Batygin Yu.V.	Professor, Kharkiv National Automobile and Highway University, Ukraine
Bíró O.	Professor, Institute for Fundamentals and Theory in Electrical Engineering, Graz, Austria
Bolyukh V.F.	Professor, NTU "KhPI", Ukraine
Colak I.	Professor, Nisantasi University, Istanbul, Turkey
Doležel I.	Professor, University of West Bohemia, Pilsen, Czech Republic
Féliachi M.	Professor, Technological Institute of Saint-Nazaire, University of Nantes, France
Gurevich V.I.	Ph.D., Honorable Professor, Central Electrical Laboratory of Israel Electric Corporation, Haifa, Israel
Ida N.	Professor, The University of Akron, Ohio, USA
Kildishev A.V.	Associate Research Professor, Purdue University, USA
Kuznetsov B.I.	Professor, SI "ITPM NASU", Ukraine
Kyrylenko O.V.	Professor, Member of NAS of Ukraine, Institute of Electrodynamics of NAS of Ukraine (IED of NASU), Kyiv, Ukraine
Nacke B.	Professor, Gottfried Wilhelm Leibniz Universitat, Institute of Electrotechnology, Hannover, Germany
Podoltsev A.D.	Professor, IED of NASU, Kyiv, Ukraine
Rainin V.E.	Professor, Moscow Power Engineering Institute, Russia
Shkolnik A.A.	Ph.D., Central Electrical Laboratory of Israel Electric Corporation, member of CIGRE (SC A2 - Transformers), Haifa, Israel
Trichet D.	Professor, Institut de Recherche en Energie Electrique de Nantes Atlantique, Nantes, France
Vinnikov D.	Professor, Tallinn University of Technology, Estonia
Yatchev I.	Professor, Technical University of Sofia, Sofia, Bulgaria
Yuferov V.B.	Professor, National Science Center "Kharkiv Institute of Physics and Technology", Ukraine
Zagirnyak M.V.	Professor, Member of NAES of Ukraine, rector of Kremenchuk M.Ostrohradskyi National University, Ukraine
Zgraja J.	Professor, Institute of Applied Computer Science, Lodz University of Technology, Poland

ISSUE 4 / 2020

TABLE OF CONTENTS

Editorial office address: Dept. of Electrical Apparatus, NTU «KhPI», Kyrpychova Str., 2, Kharkiv, 61002, Ukraine
phones: +380 57 7076281, +380 67 3594696, **e-mail:** a.m.grechko@gmail.com (**Grechko O.M.)**

ISSN (print) 2074-272X
ISSN (online) 2309-3404

© National Technical University «Kharkiv Polytechnic Institute», 2020
© State Institution «Institute of Technical Problems of Magnetism of the NAS of Ukraine», 2020

Printed 21 August 2020. Format 60 x 90 ⅛. Paper – offset. Laser printing. Edition 200 copies.
Printed by Printing house «Madrid Ltd» (18, Gudanova Str., Kharkiv, 61024, Ukraine)

UDC 621.313:536.2.24:539.2 **doi: 10.20998/2074-272X.2020.4.01**

V.F. Bolyukh, I.S. Schukin

EXCITATION WITH A SERIES OF PULSES OF A LINEAR PULSE ELECTRODYNAMIC TYPE CONVERTER OPERATING IN POWER AND HIGH-SPEED MODES

Purpose. *The aim of the article is to increase the efficiency of linear pulse electrodynamic type converter (LPEC) when operating in high-speed and force modes by reducing the amplitude of the recoil force by exciting its windings with a series of pulses from the capacitive energy storage (CES).* ***Methodology.*** *Using the LPEC mathematical model, in which the equations describing the interconnected electrical, magnetic, mechanical and thermal processes are presented in a recursive form, the electrodynamic and electromechanical characteristics of LPEC are simulated by excitation by a single and a series of pulses from CES sections.* ***Results.*** *It was found that when a single pulse is excited by an LPEC operating in a high-speed mode, in which the armature accelerates the actuator, compared with the force mode in which the armature is inhibited, the current amplitude in the windings decreases by 7.5 %, and the amplitudes of electrodynamic force (EDF) – by 21.8 %, impulse values of EDF – by 27.1 %. In this case, the armature winding with the actuating element accelerates to a speed of 7.1 m/s. When excited by a series of pulses from the same sections of the CES during LPEC operation in the force mode, the amplitudes of the current pulses and the EDF are practically unchanged, and when operating in high-speed mode, the amplitudes of the currents and the EDF gradually decrease. Both in power and in high-speed operating modes, an increase in the number of excitation pulses while conserving the energy of the CES leads to a decrease in the main indicators of LPEC. But by reducing the amplitude of the EDF, which manifests itself as a recoil force, the efficiency of LPEC increases.* ***Originality.*** *It is shown that the excitation of LPEC by a series of pulses increases the efficiency of LPEC when operating in high-speed and power modes, providing a minimum amplitude of the EDF, which determines the recoil force acting on the inductor winding.* ***Practical value.*** *For LPEC operating in high-speed mode, it is proposed to reduce the maximum current amplitudes and EDF due to the sequential increase in capacitances of sections of the CES, forming a series of excitation pulses. For LPEC, operating in force mode, it is advisable to use the same capacities of all sections of the CES.* References 22, figures 9.

Key words: **linear pulse electrodynamic type converter, mathematical model, high-speed and force operation mode, excitation by a series of pulses, recoil force, efficiency criterion.**

Представлена математична модель лінійного імпульсного перетворювача електродинамічного типу (ЛІПЕТ), в якій рішення рівнянь, що описують взаємопов'язані електричні, магнітні, механічні та теплові процеси, подані в рекурентному вигляді. Досліджено електромеханічні і електродинамічні характеристики ЛІПЕТ при роботі в швидкісному режимі, що забезпечує прискорення обмотки якоря з виконавчим елементом, та в силовому режимі при загальмованій обмотці якоря. Показано, що при збудженні одиночним імпульсом ЛІПЕТ, який працює в швидкісному режимі, в порівнянні з силовим режимом, відбувається зменшення амплітуди струму в обмотках на 7,5 %, амплітуди електродинамічних зусиль (ЕДЗ) – на 21,8 %, значення імпульсу ЕДЗ – на 27,1 %. При цьому обмотка якоря з виконавчим елементом розганяється до швидкості 7,1 м/с. При збудженні серією імпульсів від однакових секцій ємнісного накопичувача енергії (ЄНЕ) та роботі ЛІПЕТ в силовому режимі амплітуди імпульсів струму і ЕДЗ практично незмінні, а при роботі в швидкісному режимі відбувається послідовне зменшення цих амплітуд. Збільшення кількості імпульсів збудження при збереженні енергії ЄНЕ призводить до зменшення основних показників ЛІПЕТ. Але за рахунок зменшення амплітуди ЕДЗ, яка проявляється як сила віддачі, ефективність ЛІПЕТ збільшується. Для ЛІПЕТ, що працює в швидкісному режимі, запропоновано зменшення максимальних амплітуд струму і ЕДЗ за рахунок послідовного збільшення ємностей секцій ЄНЕ, які формують серії імпульсів збудження. Для ЛІПЕТ, що працює в силовому режимі доцільно використовувати однакові ємності всіх секцій ЄНЕ. Бібл. 22, рис. 9.

Ключові слова: **лінійний імпульсний перетворювач електродинамічного типу, математична модель, швидкісний і силовий режим роботи, збудження серією імпульсів, сила віддачі, критерій ефективності.**

Представлена математическая модель линейного импульсного преобразователя электродинамического типа (ЛИПЭТ), в которой решения уравнений, описывающих взаимосвязанные электрические, магнитные, механические и тепловые процессы, представлены в рекуррентном виде. Исследованы электромеханические и электродинамические характеристики ЛИПЭТ при работе в скоростном режиме, обеспечивающем ускорение обмотки якоря с исполнительным элементом, и в силовом режиме, когда обмотка якоря заторможена. Показано, что при возбуждении одиночным импульсом ЛИПЭТ, работающего в скоростном режиме, по сравнению с силовым режимом происходит уменьшение амплитуды тока в обмотках на 7,5 %, амплитуды электродинамических усилий (ЭДУ) – на 21,8 %, значения импульса ЭДУ – на 27,1 %. При этом обмотка якоря с исполнительным элементом разгоняется до скорости 7,1 м/с. При возбуждении серией импульсов от одинаковых секций емкостного накопителя энергии (ЕНЭ) и работе ЛИПЭТ в силовом режиме амплитуды импульсов тока и ЭДУ практически неизменны, а при работе в скоростном режиме происходит последовательное уменьшение амплитуд токов и ЭДУ. Увеличение количества импульсов возбуждения при сохранении энергии ЕНЭ приводит к уменьшению основных показателей ЛИПЭТ. Но за счет уменьшения амплитуды ЭДУ, которая проявляется как сила отдачи, эффективность ЛИПЭТ увеличивается. Для ЛИПЭТ, работающего в скоростном режиме, предложено уменьшение максимальных амплитуд тока и ЭДУ за счет последовательного увеличения емкостей секций ЕНЭ, формирующих серии импульсов возбуждения. Для ЛИПЭТ, работающего в силовом режиме, целесообразно использовать одинаковые емкости всех секций ЕНЭ. Библ. 22, рис. 9.

Ключевые слова: **линейный импульсный преобразователь электродинамического типа, математическая модель, скоростной и силовой режим работы, возбуждение серией импульсов, сила отдачи, критерий эффективности.**

© V.F. Bolyukh, I.S. Schukin

Introduction. Linear pulse electrodynamic type converters (LPEC) are widely used to accelerate the actuator (A) to high speed in a short active section and to create powerful force pulses on the target with a slight movement of the A [1-3]. Such converters operating in both high-speed and force modes are widely used in many branches of science and technology as electromechanical accelerators of A and shock-force devices [4, 5].

As the analysis shows, LPECs have improved force and speed indicators compared to inductive and electromagnetic converters which are also widely used for similar applications [6].

In the induction-type converter, the armature is made in the form of a single or multi-turn short-circuited winding, in which current is induced from the inductor winding. However, due to the phase shift between the currents in the windings of the inductor and the armature, in addition to the electrodynamic forces of repulsion, parasitic attractive forces also arise. As a result, the efficiency of such a converter decreases [7].

An electromagnetic type converter has an armature made ferromagnetic and an electromagnetic force of attraction acts on it from the side of the inductor winding. However, due to the physical properties of a ferromagnetic, in such a converter electromagnetic processes are slow in nature with relatively low force amplitudes. This also leads to low efficiency of the electromagnetic type converter, especially when operating in high-speed mode [8].

LPEC contains a movable armature winding (AW), which electrodynamically interacts with the stationary indictor winding (IW) [9, 10]. These windings are usually connected in series and are excited from a capacitive energy storage device (CES). Since both windings are wound counterclockwise in magnetic field, electrodynamic repulsive forces (EDF) arise between them. LPEC windings are multi-turn in the form of disks coaxially mounted opposite each other (Fig. 1).

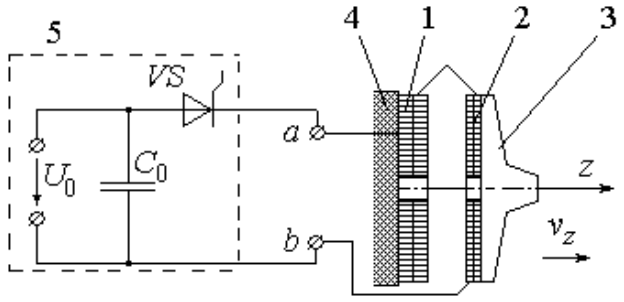

Fig. 1. LPEC diagram:
1 – IW, 2 – AW, 3 – A, 4 – stop, 5 – CES

In the high-speed mode of operation, under the influence of the repulsion EDFs, the AW along with the A axially moves relative to the IW along the *z* axis with speed v_z. However, these same EDFs also affect IW, which leads to the appearance of the recoil force of the LPEC. The recoil force negatively affects the functioning of the converter in many technical objects and systems, reducing their mechanical reliability. For a number of applications, for example, riveting, grooving, marking and other manual percussion instruments, for launch systems, for example, catapults for unmanned aerial vehicles, various autonomous starters, and others, the recoil force negatively affects both the device itself and the operating personnel [11]. The recoil force is especially negative in various measuring devices. For example, in a ballistic laser gravimeter designed to measure the acceleration of gravity, an electromechanical catapult is used, which provides a vertical toss of the A – an angular optical reflector [12]. This reflector is an integral part of the measurement system of a Michelson laser interferometer. The recoil force arising during the tossing of the A causes autoseismic oscillations, which reduce the accuracy of measuring gravitational acceleration [13].

Recently, studies of linear pulsed electromechanical converters have appeared, for the excitation of which from the CES various shapes of current pulses generated by electronic devices are used [14]. Of interest is the excitation of a linear electromechanical induction-type accelerator with superconducting magnets by a series of rectangular pulses [15, 16]. This excitation system is used to recover part of the energy in the power source.

A method of excitation of a linear electromechanical accelerator of induction type by a series of consecutive pulses from sections of the CES is known [17]. However, in this accelerator, each section of the CES is connected to its section of IW, which are offset from each other along the axis of movement of the electrically conductive armature. However, if the IW is made non-partitioned, then such a system does not solve the problem of reducing the recoil force.

Thus, a decrease in the amplitude of the EDFs, manifested in the form of a recoil force, when the LPEC performs its functions in high-speed and force modes, is an urgent task.

The goal of the paper is increasing the efficiency of LPEC when operating in high-speed and force modes by reducing the amplitude of the recoil force by exciting its windings with a series of pulses from sections of the CES.

To excite LPEC from the CES, we use a half-wave polar pulse generated by the starting thyristor *VS*, assuming that its resistance in the forward direction is negligible and in the opposite direction its conductivity is equally small. Note that with such an excitation pulse, at the end of the operating cycle, a part of the energy is stored in the CES, which allows its further use [18, 19].

The mathematical model of LPEC. Consider the mathematical model of LPEC, which uses the lumped parameters of the active elements – IW and AW. This model allows to quickly calculate LPEC indicators when excited by a series of consecutive pulses. To take into account the interconnected electrical, magnetic, mechanical and thermal processes, as well as a number of non-linear dependencies, we present the solutions of the equations describing these processes in a recursive form.

In the calculation, the workflow is divided into a number of numerically small time intervals $\Delta t = t_{k+1} - t_k$ within which we consider all quantities to be unchanged. With this approach, linear equations and relations can be used to determine the excitation current and voltage of the CES on the calculated time interval Δt.

Electrical processes in LPEC when excited by a single current pulse from the CES can be described by the equation [7]:

$$\left[R_1(T_1) + R_2(T_2)\right]\cdot i + \frac{d\psi}{dt} + \frac{1}{C_0}\int_0^t i dt = 0\,, \quad u_C(0) = U_0\,, \quad (1)$$

where n = 1, 2 are the indices of IW and AW, respectively; R_n, T_n are the resistance and temperature of the n-th winding, respectively; i is the current IW and AW; C_0 is the capacity of the CES charged to voltage U_0; u_C is the voltage of the CES;

$$\frac{d\psi}{dt} = \left[L_1 - 2M_{12}(z) + L_2\right]\frac{di}{dt} - 2iv_z(t)\frac{dM_{12}}{dz}\,; \quad (2)$$

where L_n is the inductance of the n-th winding; $M_{12}(z)$ is the mutual inductance between the IW and the AW moving along the z axis at speed v_z.

On a numerically small time interval Δt we assume that all functional dependencies are unchanged: $R_1(T_1) = R_1$, $R_2(T_2) = R_2$, $M_{12}(z) = M_{12}$, $v_z(t) = v_z$.

Substituting equation (2) in (1) we obtain:

$$\left(R_1 + R_2 - 2v_z\frac{dM_{12}}{dz}\right)\cdot i + \left[L_1 - 2M_{12} + L_2\right]\frac{di}{dt} + \frac{1}{C_0}\int_0^t i dt = 0. \quad (3)$$

The solution to equation (3) will be sought in the form:

$$i = A_1\exp(\alpha_1 t) + A_2\exp(\alpha_2 t)\,, \quad (4)$$

where $\alpha_{1,2} = -0{,}5\frac{\Theta}{\Xi} \pm \left[0{,}25\left(\frac{\Theta}{\Xi}\right)^2 - \frac{1}{C_0\Xi}\right]^{0,5}$ are the roots of the characteristic equation; A_1, A_2 are the arbitrary constants;

$$\Xi = L_1 - 2M_{12} + L_2\,;$$

$$\Theta = R_1 + R_2 - 2v_z\frac{dM_{12}}{dz}\,.$$

If $\Theta > 2\sqrt{\Xi C_0^{-1}}$, then after a series of transformations we obtain expressions for arbitrary constants at time t_k:

$$A_{1,2} = \frac{u_C(t_k) + \Theta\cdot i(t_k) + \alpha_{2,1}\Xi\cdot i(t_k)}{\Xi\exp(\alpha_{1,2}t_k)(\alpha_{2,1} - \alpha_{1,2})}\,. \quad (5)$$

Substituting expressions (5) into equation (4), we obtain the expression for the current in a recurrent form:

$$i(t_{k+1}) = \frac{u_C(t_k) + \Theta\cdot i(t_k)}{\Xi(\alpha_2 - \alpha_1)}\left[\exp(\alpha_1\Delta t) - \exp(\alpha_2\Delta t)\right] + \frac{i(t_k)}{\alpha_2 - \alpha_1}\left[\alpha_2\exp(\alpha_1\Delta t) - \alpha_1\exp(\alpha_2\Delta t)\right]. \quad (6)$$

The voltage on the CES:

$$u_C(t_{k+1}) = \frac{u_C(t_k) + \Theta\cdot i(t_k)}{\alpha_2 - \alpha_1}\left[\alpha_2\exp(\alpha_1\Delta t) - \alpha_1\exp(\alpha_2\Delta t)\right] + \Xi\frac{i(t_k)}{\alpha_2 - \alpha_1}\left[\alpha_2^2\exp(\alpha_1\Delta t) - \alpha_1^2\exp(\alpha_2\Delta t)\right] \quad (7)$$

If $\Theta < 2\sqrt{\Xi C_0^{-1}}$, then the roots of the characteristic equation can be represented as:

$$\alpha_{1,2} = -\delta \pm j\omega_1 = \omega_0\exp\left(j(\pi \pm \theta)\right), \quad (8)$$

where $\delta = 0{,}5\Theta\Xi^{-1}$; $\theta = \operatorname{arctg}\left(4\Xi\Theta^{-2}C_0^{-1} - 1\right)^{0,5}$; $\omega_0 = \left(\Xi C_0\right)^{-0,5}$; $\omega_1 = \left(\Xi^{-1}C_0^{-1} - 0.25\Theta^2\Xi^{-2}\right)^{0,5}$.

Substituting the values of the roots (8) in equation (6) and taking into account that

$$2j\sin(\omega_1\Delta t) = \exp(j\omega_1\Delta t) - \exp(-j\omega_1\Delta t)\,,$$

we obtain:

$$i(t_{k+1}) = -\omega_1^{-1}\exp(-\delta\Delta t)\left\{\Xi^{-1}\left[u_C(t_k) + \Theta\cdot i(t_k)\right]\times \sin(\omega_1\Delta t) + \omega_0 i(t_k)\sin(\omega_1\Delta t - \theta)\right\}. \quad (9)$$

The voltage on the CES in this case:

$$u_C(t_{k+1}) = -\omega_0\omega_1^{-1}\exp(-\delta\Delta t)\left\{\left[u_C(t_k) + \Theta\cdot i(t_k)\right]\times \sin(\omega_1\Delta t - \theta) + i(t_k)\omega_0\Xi\sin(\omega_1\Delta t - 2\theta)\right\}. \quad (10)$$

If $\Theta = 2\sqrt{\Xi C_0^{-1}}$, tnen $\delta = \omega_0$ and the current is:

$$i(t_{k+1}) = \exp(-\delta\Delta t)\Delta t\left\{i(t_k)\delta - \Xi^{-1}\times \times\left[u_C(t_k) + \Theta\cdot i(t_k)\right]\right\}. \quad (11)$$

The voltage on the CES in this case:

$$u_C(t_{k+1}) = \left[u_C(t_k) - i(t_k)\Xi\delta + \Theta\cdot i(t_k)\right](\delta\Delta t + 1)\times \times\exp(-\delta\Delta t) + i(t_k)(\Xi\delta - \Theta). \quad (12)$$

The value of the displacement of AW with A relative to IW can be represented as a recurrence relation:

$$h_z(t_{k+1}) = h_z(t_k) + v_z(t_k)\Delta t + \vartheta\cdot\Delta t^2/(m_a + m_2)\,, \quad (16)$$

where $v_z(t_{k+1}) = v_z(t_k) + \vartheta\cdot\Delta t/(m_a + m_2)$ is the speed of AW with A;

$\vartheta = f_z(z,t) - K_T v_z(t_k) - 0{,}125\pi\gamma_a\beta_a D_{e2}^2 v_z^2(t_k)$;

$f_z(z,t) = i^2(t_k)\frac{dM_{12}}{dz}(z)$ is the instantaneous value of axial EDF between windings; m_2, m_a are the masses of AW and A, respectively; h_z is the value of displacement of AW with A; K_T is the dynamic friction coefficient; γ_a is the density of the medium fir movement; β_a is the drag coefficient; D_{e2} is the outer diameter of A.

When LPEC is operating in force mode, there is thermal contact between the IW and the AW through an insulating gasket. The temperature of the n-th LPEC winding can be described by the recurrence relation [20]:

$$T_n(t_{k+1}) = T_n(t_k)\xi + (1-\xi)\left[\pi^{-1}i^2(t_k)R_n(T_n)\left(D_{en}^2 - D_{in}^2\right)^{-1} + 0{,}25\pi T_0 D_{en}H_n\alpha_{Tn} + T_m(t_k)\lambda_a(T)d_a^{-1}\right]\times \times\left\{0{,}25\pi\alpha_{Tn}D_{en}H_n + \lambda_a(T)d_a^{-1}\right\}^{-1}, \quad (17)$$

where $\xi = \exp\left\{-\frac{\Delta t}{c_n(T_n)\gamma_n}\left(0{,}25D_{en}\alpha_{Tn} + \frac{\lambda_a(T)}{d_a H_n}\right)\right\}$;

$\lambda_a(T)$ is the thermal conductivity coefficient of the gasket; d_a is the thickness of the gasket; D_{en}, D_{in} are the outer and inner diameters of the n-th winding, respectively; α_{Tn}, c_n are the heat transfer coefficient and heat capacity of the n-th winding, respectively.

When LPEC is operating in high-speed mode, the temperature of the n-th winding can be described by the recurrence relation [20]:

$$T_n(t_{k+1}) = T_n(t_k)\chi + (1-\chi)\left[T_0 + 4\pi^{-2} i^2(t_k) \times \right.$$
$$\left. \times R_n(T_n)\alpha_{Tn}^{-1} D_{en}^{-1} H_n^{-1}\left(D_{en}^2 - D_{in}^2\right)^{-1}\right], \quad (18)$$

where $\chi = \exp\left\{-0{,}25\Delta t D_{en}\alpha_{Tn} c_n^{-1}(T_n)\gamma_n^{-1}\right\}$.

To calculate the characteristics and indicators of LPEC, we use a cyclic action algorithm that allows to take into account a set of interrelated processes and various nonlinear dependencies, for example, $R_n(T_n)$, $M_{12}(z)$. Based on the current values obtained at time t_{k+1}, the temperatures of the windings T_1 and T_2, the displacement h_z and the speed of the AW v_z, the mutual inductance M_{12} between the windings, etc. are calculated. The value of the calculation step Δt is chosen so that it does not significantly affect the calculation results, providing with the necessary accuracy.

The initial conditions of the mathematical model:
$T_n(0) = T_0$ is the temperature of the n-th winding;
$i_n(0) = 0$ is the current of the ток n-th winding;
$h_z(0) = h_{z0}$ is the distance between IW and AW;
$u_c(0) = U_0$ is the CES voltage;
$v_z(0) = 0$ is the AW speed along the z axis.

The main parameters of LIPET. Let us consider LPEC, in which IW (n = 1) and AW (n = 2) are made in the form of two-layer disk coils. IW is wound with a copper bus bar with cross section of 1.2×5.0 mm^2, and AW is wound with a copper bus bar with cross section of 1.2×2.5 mm^2. Number of turns of the n-th winding N_n = 60, outer diameter D_{en} = 100 mm, inner diameter D_{in} = 8 mm. CES: energy W_0 = 180 J, voltage U_0 = 300 V. The initial distance between the windings is h_{z0} = 1 mm.

When LPEC is operating in high-speed mode, we use A with mass of m_a = 0.5 kg, and evaluate its effectiveness with maximum speed v_{zm} at minimum recoil force. When LPEC is operating in the force mode, we assume that there is no displacement of the AW with the A ($m_a = \infty$), and its efficiency will be estimated using the maximum value of the EDF impulse $P_z = \int f_z(z,t)dt$ at the minimum recoil force.

LPEC excitation by a single pulse is carried out from the CES with capacitance C_0 = 4 mF. When operating in the power mode (Fig. 2), the current amplitude in the LPEC windings is i_m = 1.478 kA, which leads to the appearance of EDF with amplitude of f_{zm} = 10.56 kN between the windings. The value of the EDF impulse at the end of the operating process (1.65 ms) is P_z = 7.88 N·s. Note that the temperature rises of the windings $\theta_n = T_0 - T_n$ are negligible (θ_1 = 0.2 °C, θ_2 = 0.7 °C).

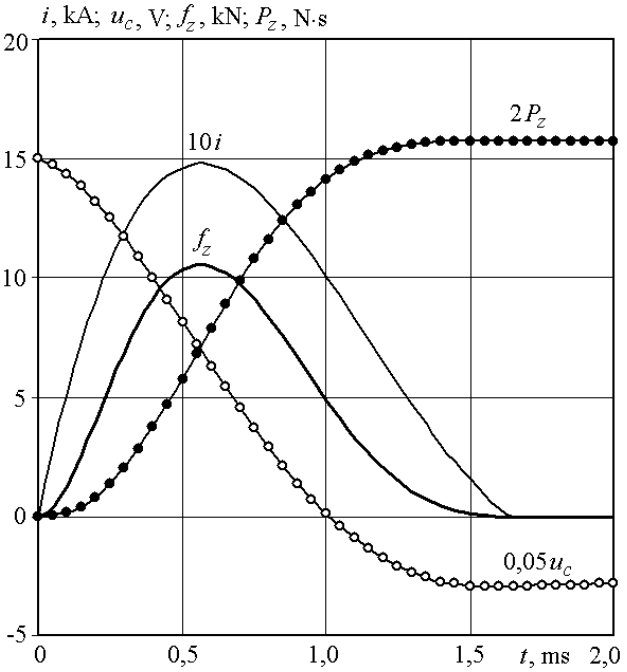

Fig. 2. Electrodynamic characteristics of LPEC when operating in force mode

When operating in high-speed mode, the operating process is delayed up to 2 ms with a decrease in all the main indicators (Fig. 3). The amplitude of the current in the windings decreases to i_m = 1.375 kA, which leads to a decrease in the amplitude of the EDF between the windings to a value of f_{zm} = 8.67 kN. The value of the EDF impulse at the end of the operating process is P_z = 6.2 N·s. The temperature rises of the windings also decrease (θ_1 = 0.18 °C, θ_2 = 0.6 °C). Such a change in the operating process is due to the movement of AW with A, which reach maximum speed of v_{zm} = 7.1 m/s.

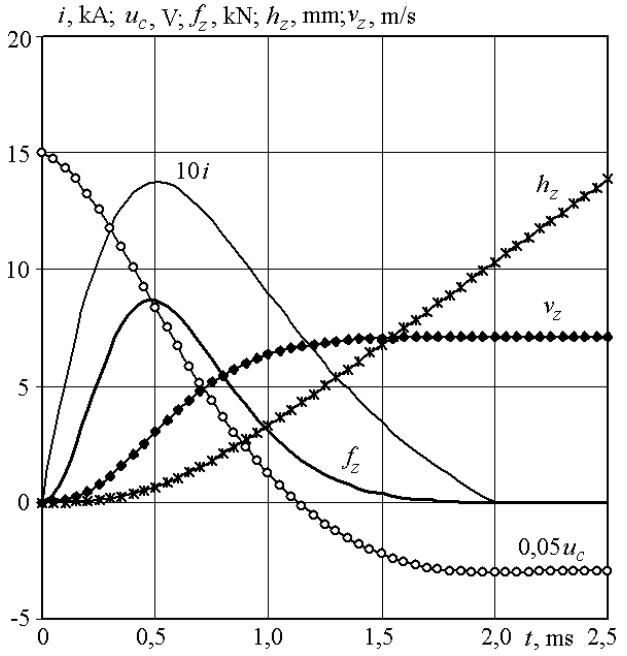

Fig. 3. Electrodynamic characteristics of LPEC when operating in high-speed mode

LPEC excitation by a series of pulses is carried out by sequentially connection in time to the terminals *a* and *b* of the sections of the CES. This forms a parallel connection of the sections of the CES to the converter windings.

Note that the parallel connection of the sections of the CES to the IW of a linear pulse induction accelerator was studied in [21, 22]. However, in these studies, all sections of the CES are connected to the IW simultaneously.

The total capacity of the sections is equal to C_0 = 4 mF. The delay time for connecting the sections determines the repetition period of the excitation current pulses. With this method of excitation, the efficiency of LPEC in force and high-speed modes is evaluated by dimensionless criteria:

$$K_p^* = \frac{P_z}{f_{zm}} \frac{f_{zm}^0}{P_z^0}, \quad K_v^* = \frac{v_{zm}}{f_{zm}} \frac{f_{zm}^0}{v_{zm}^0}, \qquad (19)$$

where $f_{zm}^0, P_z^0, v_{zm}^0$ are the values of the amplitude and impulse of the EDF, the speed of the AW with A, respectively, when excited by a single pulse.

The essence of these criteria is to ensure the greatest value of the EDF impulse for the force mode, and the highest speed of the AW with A for the high-speed mode with minimum amplitude of the EDF which determines the recoil force. These criteria evaluate the efficiency of LPEC when excited by a series of pulses with respect to excitation by a single pulse.

Figure 4 shows the electrodynamic characteristics of LPEC when operating in force mode from five identical sections of the CES connected to the windings in series with a delay of 0.75 ms. For each excitation pulse, the current amplitude is practically unchanged and is i_m = 0.788 kA, which is almost 2 times less than when excited by a single pulse. The amplitude of the EDF decreases even more, reaching f_{zm} = 3 kN. The value of the EDF impulse at the end of the operating process also decreases, but to a lesser extent, amounting to P_z = 4.9 N·s. The temperature rises of the windings also decrease (θ_1 = 0.13 °C, θ_2 = 0.42 °C). However, the efficiency criterion of the converter K_p^* increases by more than 2 times, compared with its excitation by a single pulse.

Figure 5 shows the electromechanical characteristics of LPEC when operating in high-speed mode from five identical sections of the CES connected to the windings in series with a delay of 1 ms. A feature of this converter is a sequential decrease in the amplitudes of the currents i_m and EDF f_{zm} when connecting sections of the CES. Such a decrease in these amplitudes is due to the sequential weakening of the magnetic coupling between the windings due to the displacement of the AW by an value of h_z. In this converter, the largest amplitudes are observed in the first pulse, amounting to current i_m = 0.783 kA, for EDF f_{zm} = 2.95 kN. The value of the EDF impulse in this case is P_z = 3.34 N·s, providing the speed of the AW with A v_z = 3.82 m/s. The temperature rises of the windings are θ_1 = 0.11 °C, θ_2 = 0.37 °C. Thus, in the high-speed mode, all indicators of LPEC, excited by a series of five pulses, decrease in comparison with excitation by a single pulse, but the criterion of converter efficiency K_v^* increases in this case by 58 %.

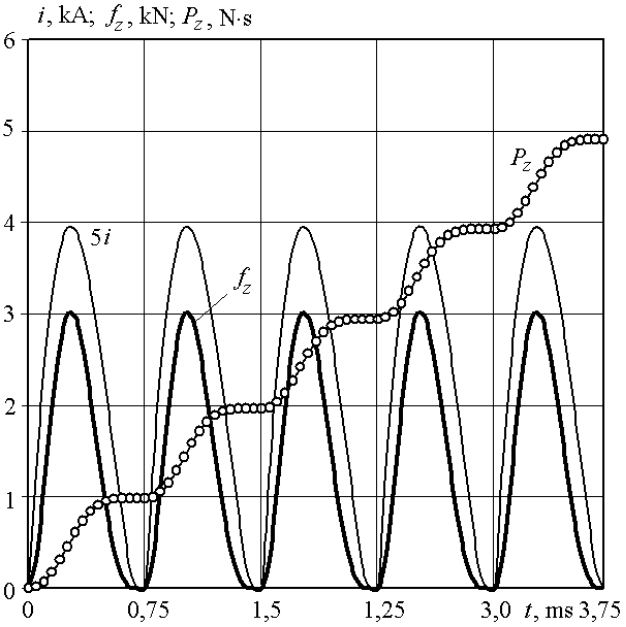

Fig. 4. Electrodynamic characteristics of LPEC when excited from the same sections of the CES

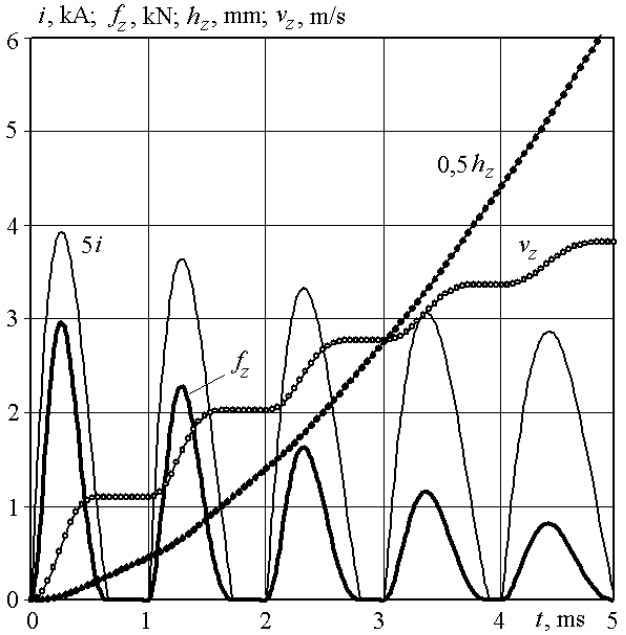

Fig. 5. Electromechanical characteristics of LPEC when excited from the same sections of the CES

To assess the effect of the number of excitation pulses N_i on the LPEC parameters, Fig. 6 is used. Both in force and in high-speed operation modes, with an increase in the number of excitation pulses N_i, a constant voltage of the sections of the CES U_0 = 300 V and conservation of their total energy W_0 = 180 J, all the main indicators decrease. These are the amplitudes of the currents i_m and

the EDF f_{zm}, the value of the impulse of the EMF P_z and the speed of the AW with A v_z. But due to a stronger decrease in the amplitude of the EDF f_{zm}, which manifests itself as the recoil force, from an increase in the number of excitation pulses, the efficiency criteria of LPEC K_p^* and K_v^* also increase.

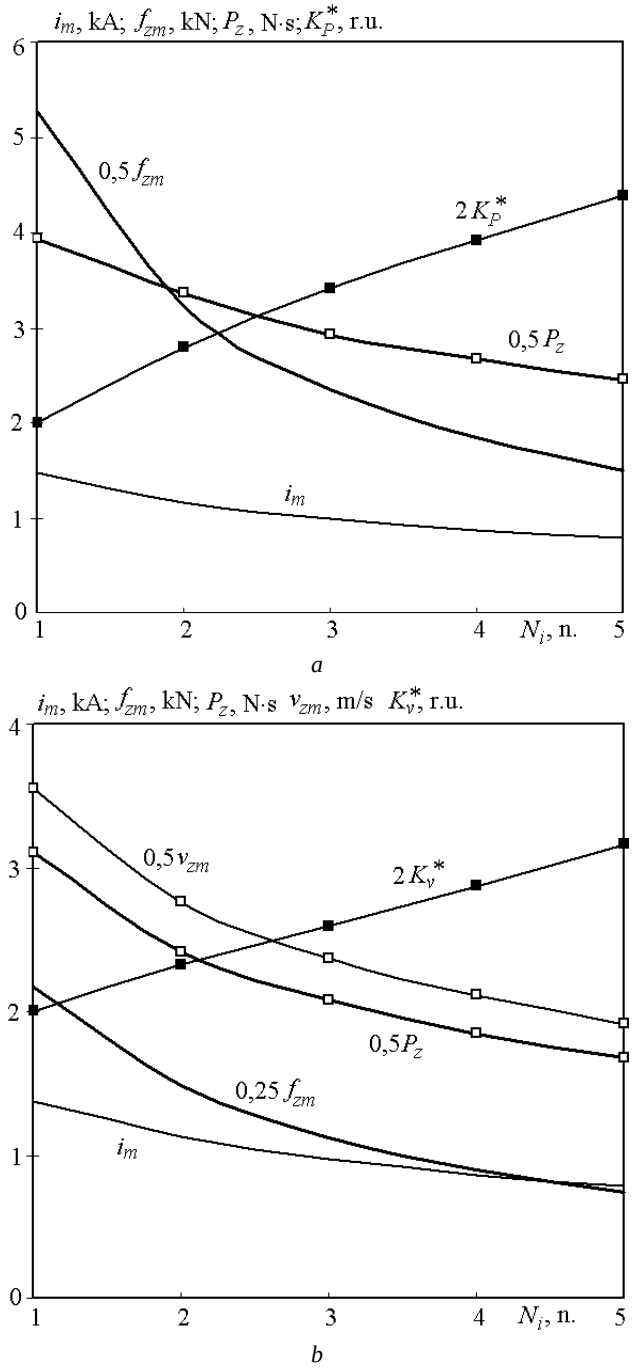

Fig. 6. Dependence of the performance of LPEC in force (*a*) and high-speed (*b*) modes on the number of excitation pulses

The maximum amplitudes of the current and EDF in the first pulse of the series for LPEC operating in high-speed mode can be reduced by sequentially increasing the capacitance of the sections of the CES while maintaining their total value C_0 = 4 mF.

Figure 7 shows the electromechanical characteristics of LPEC when operating in high-speed mode and excitation from five sections of the CES, whose capacitances linearly increase from 0.4 mF in the first section to 1.2 mF in the fifth section.

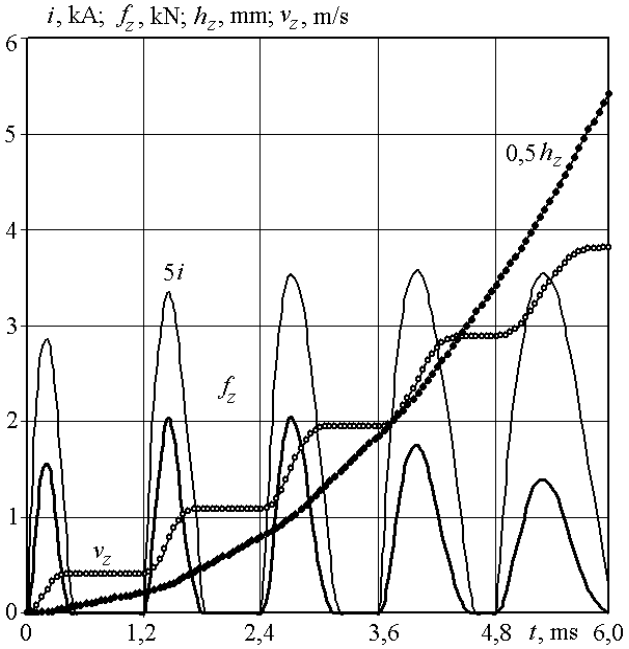

Fig. 7. Electromechanical characteristics of LPEC when operating in high-speed mode and excitation from sections of the CES, the capacities of which increase linearly

With this excitation, of LPEC operating in high-speed mode, the maximum current amplitude is observed not in the first but in the fourth pulse of the series and is i_m = 713.9 A, which is lower than when excited from identical sections of the CES. The maximum amplitude of the EDF is observed in the third pulse of the series and amounts to f_{zm} = 2.04 kN. Note that the decrease in the current amplitude after the fourth pulse of the series is due to the weakening of the magnetic coupling between the IW and AW. A decrease in the amplitudes of the EDF after the third pulse of the series is additionally caused by an increase in the distance between them.

With this method of LPEC excitation, the value of the EDF impulse is P_z = 3.33 N·s, which ensures the speed of the AW with A v_z = 3.81 m/s.

Figure 8 shows the electrodynamic characteristics of LPEC during operation in the force mode and excitation from five sections of the CES, whose capacitances linearly increase from 0.5 mF in the first section to 1.1 mF in the fifth section. With this excitation of LPEC operating in the force mode, the maximum current amplitude arises in the fifth pulse of the series and is equal to i_m = 908 A, which is higher than when excited from identical sections of the CES. The maximum amplitude of the EDF also occurs in the fifth pulse of the series and amounts to f_{zm} = 3.98 kN. The value of the impulse of EDF is P_z = 4.98 N·s.

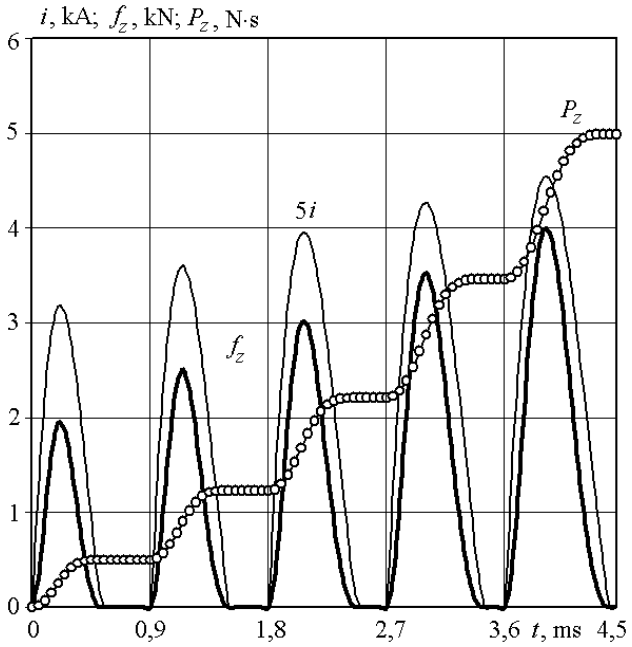

Fig. 8. Electrodynamic characteristics of LIPET when operating in force mode and excitation from sections of the CES, the capacities of which increase linearly

To assess the effect of the regularity of the distribution of capacitances in sections of the CES on the performance of LPEC when operating in high-speed and force modes, Fig. 9 is used, where the indicator of the distribution of capacitances in sections of the CES is used:

$$K_c^* = 2(C_{\max} - C_{\min})(C_{\max} + C_{\min})^{-1},$$

where $C_{\min}$, $C_{\max}$ are the capacitances of the first and fifth sections of the CES, respectively.

Note that at $K_c^* = 0$ the capacitances of all five sections of the CES are the same.

When LPEC is operating in high-speed mode, an increase in the indicator K_c^* substantially changes only the maximum amplitude of the EDF f_{zm} which noticeably decreases in the interval $K_c^* \subset (0, 1)$. This affects the efficiency criterion K_v^*, the maximum value of which will be at $K_c^* = 1$ ($C_{\min}$ = 0.4 mF, $C_{\max}$ = 1.2 mF). If the indicator K_c^* exceeds 1, the efficiency criterion K_v^* decreases due to an increase in the amplitude of the EDF in the last fifth pulse of the series. When LPEC is operating in force mode, an increase in the indicator K_c^* leads to an increase in the maximum amplitude of the EDF f_{zm}, as a result of which the efficiency criterion K_p^* decreases.

Thus, when excitation by a series of pulses from sections of the CES by reducing the amplitude of the recoil force, an increase in the efficiency of LPEC is provided. For a converter operating in high-speed mode, it is advisable to increase the indicator of the distribution of capacitances in sections of the CES to a certain value ($K_c^* = 1$). For a converter operating in force mode, it is advisable to use the same capacitances for all sections of the CES.

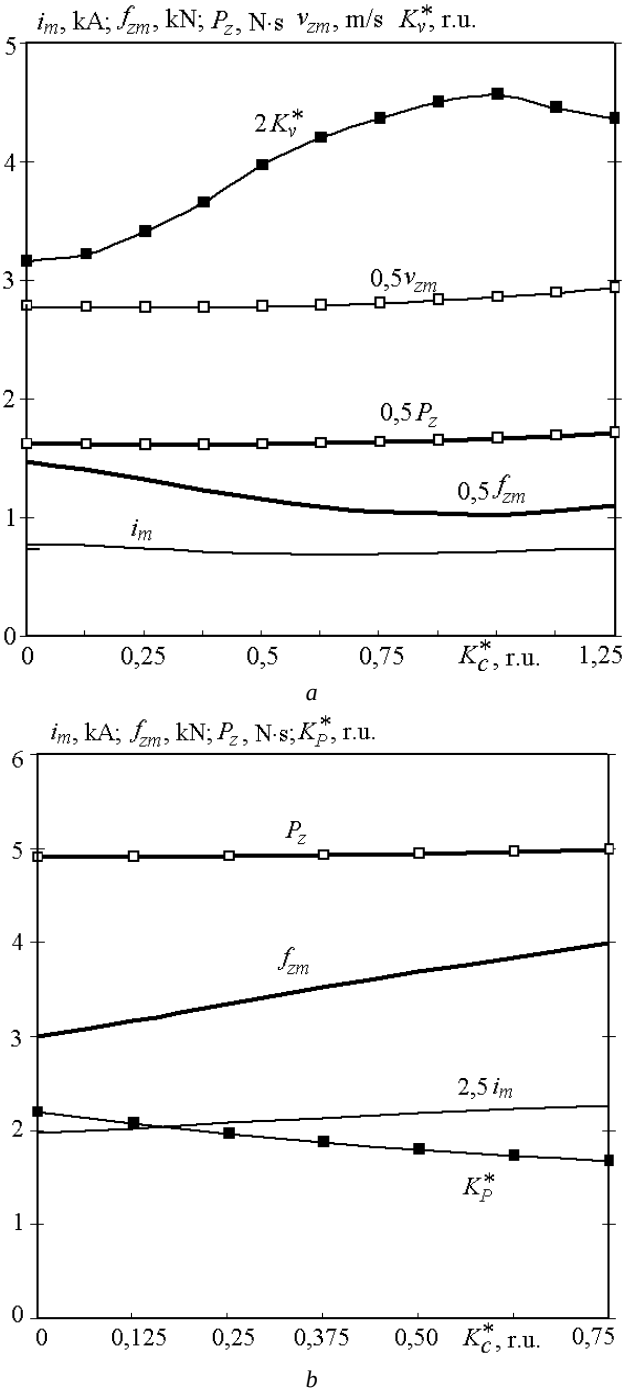

Fig. 9. Dependence of the performance of LPEC in high-speed (*a*) and force (*b*) modes on the indicator of the distribution of capacitances in sections of the CES

Conclusions.

1. It is shown that when the windings are excited by a series of pulses from sections of a capacitive energy storage unit (CES), an increase in the efficiency of a linear pulse electrodynamic type converter (LPEC) is

ensured during operation in high-speed and force modes due to a decrease in the amplitude of the recoil force.

2. A mathematical model of LPEC is presented, in which the solutions of the equations describing the interconnected electrical, magnetic, mechanical and thermal processes are presented in a recursive form.

3. It has been established that at excitation by single-pulse of LPEC operating in a high-speed mode, compared with a force mode, the current amplitude in the windings decreases by 7.5 %, the amplitudes of electrodynamic forces (EDFs) – by 21.8 %, the value of the EDF impulse – by 27.1 %. In this case, the armature winding with the actuating element accelerates to speed of 7.1 m/s.

4. It has been established that at excitation by a series of pulses from the same sections of the CES during LPEC operation in the force mode, the amplitudes of the current pulses and the EDF are practically unchanged, while when operating in high-speed mode, the amplitudes of the currents and EDF decrease sequentially. An increase in the number of excitation pulses while conserving the energy of the CES leads to a decrease in the main indicators of LPEC. But due to a decrease in the amplitude of the EDF, which manifests itself as a recoil force, the efficiency of LPEC is increased.

5. For LPEC operating in high-speed mode, a consistent increase in the capacitances of sections of the CES, forming a series of excitation pulses, is justified. For LPEC, operating in force mode, it is advisable to use the same capacitances of all sections of the CES.

REFERENCES

1. Bissal A., Magnusson J., Engdahl G. Comparison of two ultra-fast actuator concept. *IEEE Transactions on Magnetics*, 2012, vol. 48, no. 11, pp. 3315-3318. **doi: 10.1109/tmag.2012.2198447.**

2. Tomashevsky D.N., Koshkin A.N. Modeling of linear impulse electric motors. *Russian Electrical Engineering*, 2006, no. 1, pp. 24-27. (Rus).

3. J. Young-woo, L. Hyun-wook, L. Seok-won. High-speed AC circuit breaker and high-speed OCD. *Proceeding of the conf.* «22-th international conference on electricity distribution». 2013, 10-13 June, Stockholm. – Paper 608.

4. D.-K. Lim, D.-K. Woo, I.-W. Kim, D.-K. Shin, J.-S. Ro, T.-K. Chung, H.-K. Jung. Characteristic Analysis and Design of a Thomson Coil Actuator Using an Analytic Method and a Numerical Method. *IEEE Transactions on Magnetics*, 2013, vol. 49, no. 12, pp. 5749-5755. **doi: 10.1109/tmag.2013.2272561**.

5. Puumala V., Kettunen L. Electromagnetic design of ultrafast electromechanical switches. *IEEE Transactions on Power Delivery*, 2015, vol. 30, no. 3, pp. 1104-1109. **doi: 10.1109/TPWRD.2014.2362996**.

6. Bolyukh V.F., Kashanskij Yu.V., Schukin I.S. Influence of geometrical parameters of the inductor and armature on the indicators of a linear pulse electromechanical converter of an electrodynamic type. *Electrical engineering & electromechanics*, 2019, no. 3, pp. 11-17. **doi: 10.20998/2074-272X.2019.3.02.**

7. Bolyukh V.F., Kashanskyi Yu.V., Shchukin I.S. Comparative analysis of power and speed indicators linear pulse electromechanical converters electrodynamic and induction types. *Technical electrodynamics*, 2019, no. 6, pp. 35-42. (Rus). **doi: 10.15407/techned2019.06.035.**

8. Bolyukh V.F., Oleksenko S.V., Shchukin I.S. Comparative analysis of linear pulse electromechanical converters electromagnetic and induction types. *Technical electrodynamics*, 2016, no. 5, pp. 46-48. (Rus). **doi: 10.15407/techned2016.05.046**.

9. Mishkin V.N., Tolstik A.I. Comparative evaluation of arresting devices on the electrodynamic and electromagnetic principle of action. *Electromagnetic pulse systems*, 1989, pp. 114-117. (Rus).

10. Balikci A., Zabar Z., Birenbaum L., Czarkowski D. Improved performance of linear induction launchers. *IEEE Transactions on Magnetics*, 2005, vol. 41, no. 1, pp. 171-175. **doi: 10.1109/tmag.2004.839283.**

11. Abdalla M.A., Mohamed H.M. Asymmetric multistage synchronous inductive coilgun for length reduction, higher muzzle velocity and launching time reduction. *IEEE Transactions on Plasma Science*, 2016, vol. 44, no. 5, pp. 785-789. **doi: 10.1109/TPS.2016.2543500.**

12. Bolyukh V.F., Vinnichenko A.I. Concept of an induction-dynamic catapult for a ballistic laser gravimeter. *Measurement Techniques*, 2014, vol. 56, iss. 10, pp. 1098-1104. **doi: 10.1007/s11018-014-0337-z.**

13. Bolyukh V.F., Omel'chenko A.V., Vinnichenko A.I. Effect of self-seismic oscillations of the foundation on the readout of a ballistic gravimeter with an induction-dynamic catapult. *Measurement Techniques*, 2015, vol. 58, no. 2, pp. 137-142. **doi: 10.1007/s11018-015-0675-5.**

14. Zhou Y., Huang Y., Wen W., Lu J., Cheng T., Gaoet S. Research on a novel drive unit of fast mechanical switch with modular double capacitors. *Journal of Engineering*, 2019, vol. 2019, no. 17, pp. 4345-4348. **doi: 10.1049/joe.2018.8148.**

15. Fan G., Wang Y., Hu Y., Yan Z. Research on energy recovery system based on HTSM for synchronous induction electromagnetic launcher system. *IEEE Transaction on Plasma Science*, 2020, vol. 48, no. 1, pp. 291-298. **doi: 10.1109/TPS.2019.2960038.**

16. Guangcheng F., Wang Y., Xu Q., Xinyi N., Yan Z. Design and analysis of a novel three-coil reconnection electromagnetic launcher. *IEEE Transactions on Plasma Science*, 2019, vol. 47, no. 1, pp. 814-820. **doi: 10.1109/TPS.2018.2874287.**

17. Niu X., Li W., Feng J. Nonparametric modeling and parameter optimization of multistage synchronous induction coilgun. *IEEE Transactions on Plasma Science*, 2019, vol. 47, no. 7, pp. 3246-3255. **doi: 10.1109/TPS.2019.2918157.**

18. Bolyukh V.F., Katkov I.I. Influence of the Form of Pulse of Excitation on the Speed and Power Parameters of the Linear Pulse Electromechanical Converter of the Induction Type. *Volume 2B: Advanced Manufacturing*, Nov. 2019, 8 p. **doi: 10.1115/IMECE2019-10388.**

19. Liu X., Yu X., Ban R., Li Z. Analysis of the capacitor-aided meat grinder circuits for an inductive pulsed power supply. *IEEE Transactions on Plasma Science*, 2017, vol. 45, no. 7, pp. 1339-1346. **doi: 10.1109/TPS.2017.2705179.**

20. Bolyukh V.F., Shchukin I.S. The thermal state of an electromechanical induction converter with impact action in the cyclic operation mode. *Russian electrical engineering*, 2012, vol.83, no.10, pp. 571-576. **doi: 10.3103/s1068371212100045**.

21. Vilchis-Rodriguez D.S., Shuttleworth R., Barnes M. Experimental Validation of a Finite Element 2D Axial Thomson Coil Model with Inductance and Resistance Compensation. *13th IET International Conference on AC and DC Power*

Transmission (ACDC 2017), 2017, Manchester, UK, 14-16 Feb. 2017. **doi: 10.1049/cp.2017.0032.**

22. Yadong Z., Ying W., Jiangjun R. Capacitor-driven coil-gun scaling relationships. *IEEE Transactions on Plasma Science*, 2011, vol. 39, no. 1, pp. 220-224. **doi: 10.1109/TPS.2010.2052266.**

Received 18.05.2020

V.F. Bolyukh[1], *Doctor of Technical Science, Professor,*
I.S. Schukin[2], *Candidate of Technical Science, Associate Professor,*
[1] National Technical University «Kharkiv Polytechnic Institute»,
2, Kyrpychova Str., Kharkiv, 61002, Ukraine,
e-mail: vfbolyukh@gmail.com
[2] Firm Tetra, LTD,
18, Gudanova Str., Kharkiv, 61024, Ukraine,
e-mail: tech@tetra.kharkiv.com.ua

How to cite this article:
Bolyukh V.F., Schukin I.S. Excitation with a series of pulses of a linear pulse electrodynamic type converter operating in power and high-speed modes. *Electrical engineering & electromechanics*, 2020, no. 4, pp. 3-11. **doi: 10.20998/2074-272X.2020.4.01.**

UDC 621.313 **doi: 10.20998/2074-272X.2020.4.02**

M. Ben Slimene

PERFORMANCE ANALYSIS OF SIX-PHASE INDUCTION MACHINE-MULTILEVEL INVERTER WITH ARBITRARY DISPLACEMENT

Purpose. This paper presents a d-q model of six-phase induction machine supplied by a two identical voltage source inverters suitable for analysis the dynamic steady under balanced operating condition. In the analytical model, the effects of common mutual leakage inductance between the dual stator have been included. The model has been developed in general reference frame taking into account of 0°, 30° and 60° displacements between two stator winding sets. The main purpose of this work is to conduct a quantitative study to show the advantage of supplying the six-phase induction machine by a multilevel inverter. The voltage and current total harmonic distortion and the torque ripple rate are the main targets. This paper is organized into four sections. After the introduction, the second section includes development of mathematical models concerning the six-phase induction machine. The third presents the effect of displacements of 0°, 30 ° and 60 ° between two stator-winding sets, and a comparison of three cases. After that, we present a comparative study between two, three, five and seven inverter levels when feeding the six-phase induction machine. For this purpose, simulations were carried out to obtain phase currents and torque ripple rates in steady state. References 13, tables 2, figures 13.

Key words: **six phase induction machine, multiphase electric drives, multiphase machines performance, displacements, multi-level inverter.**

Цель. В статье представлена d-q модель шестифазной асинхронной машины, снабженной двумя идентичными инверторами источника напряжения, пригодными для анализа динамической устойчивости при сбалансированных условиях работы. В аналитическую модель включено влияние общей взаимной индуктивности рассеяния между двойным статором. Модель разработана в общей системе отсчета с учетом смещений на 0°, 30° и 60° между двумя наборами обмоток статора. Основная цель данной работы – провести количественное исследование, чтобы показать преимущество питания шестифазной асинхронной машины многоуровневым инвертором. Общее гармоническое искажение напряжения, тока и пульсация крутящего момента являются основными целями исследования. Статья состоит из четырех разделов. После введения, второй раздел содержит разработку математических моделей применительно к шестифазной асинхронной машине. В третьем разделе представлено влияние смещения на 0°, 30° и 60° между двумя наборами обмоток статора, а также сравнение трех указанных случаев. После этого представлено сравнительное исследование двух, трех, пяти и семи уровней инвертора при питании шестифазной асинхронной машины. Для этой цели проведено моделирование с целью получения фазных токов и пульсаций крутящего момента в стационарном состоянии. Библ. 13, табл. 2, рис. 13.

Ключевые слова: **шестифазная асинхронная машина, многофазные электроприводы, производительность многофазных машин, смещения, многоуровневый инвертор.**

Introduction. Multi-phase induction machine has many advantages over conventional three-phase such as reducing torque pulsation, reducing the stator current per phase without increasing the voltage per phase, reducing the rotor harmonic current and higher reliability [1, 2]. In particular, with loss of one or more of stator winding excitation sets, a multi-phase induction machine can continue to be operated with an asymmetrical winding structure and unbalanced excitation, [1].

By dividing the required power between multiple phases, higher power levels can be obtained and the limits of number of machine phases have been removed when employing voltage source inverter [3]. The use of multi-phase machines permits to take advantage of additional degrees of freedom but is likely limited to specialized applications such as electric/hybrid vehicles, aerospace applications, ship propulsion, and high power application [3, 4]. In the literature, a variety of transformations has been proposed for the analysis for multi-phase induction machine.

T.A. Lipo [5] and G.K. Singh [1, 6, 7] derived a *d-q* model for a six-phase machine in dynamic and sinusoidal steady state; the slot leakage coupling between two stators winding sets was incorporated into the model. T.A. Lipo has explained this in detail and has given the technique for finding the slot reactance. Y. Zhao [8] and M.A. Abbas [2] have reported the model for six-phase induction machine supplied by PWM inverter with spatially phase shifted by 30 electrical degrees and where mutual leakage inductances are neglected. R.H. Nelson [9] carried out simulation on three types of six-phase machine using a voltage source inverter where the dual stators are shifted by 0, 30 and 60 electrical degrees and mutual leakage inductances are neglected. Nevertheless, there have been studies where the mutual leakage inductance has been neglected [2, 5, 7-13].

In this paper, an analytical *d-q* model of six-phase induction machine has been developed in a general reference frame and the effect of mutual leakage inductance has been included. The presence of the mutual leakage impedance between the two stars of induction generator is due to the fact their windings share the same slots, and are, therefore, mutually coupled. The mutual leakage coupling has an important effect on the harmonic coupling between the two stator winding sets and depends on the winding pitch and the displacement angle between the two stator winding sets. Subsequently, the six phase induction machine (SPIM) is fed by two identical source inverters taking into account of 0°, 30° and 60° displacements between two stators winding sets and a comparison of three cases has been presented.

The **purpose** of this work is to conduct a quantitative study to show the advantage of supplying the six-phase induction machine by a multilevel inverter.

Modeling of six-phase induction machine. More than three phase windings are housed in the same stator in a multiphase induction motor and thus the current per

© M. Ben Slimene

phase in the motor is reduced. Two sets of three phase windings are moved by 30° electrical spatially (Fig. 1) in the most typical of these structures.

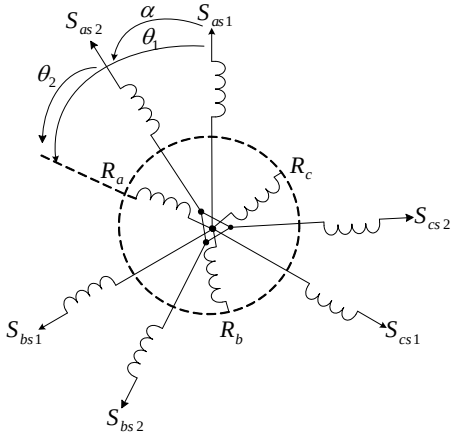

Fig. 1. Schematic representation of the SPIM

In the Fig. 2 the common mutual leakage inductance represents the fact that the two sets of stator windings occupy the same slots mutually coupled by a component of leakage flux.

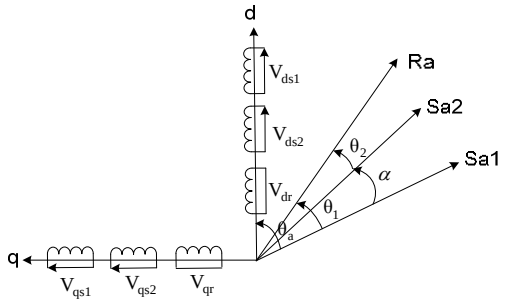

Fig. 2. *d-q* transformation of the SPIM

The electric equations of stator 1, stator 2 and of rotor are respectively expressed by:

$$\left[V_{abc,s1}\right]=\left[R_{s1}\right]\cdot\left[I_{abc,s1}\right]+\frac{d}{dt}\left[\psi_{abc,s1}\right]; \quad (1)$$

$$\left[V_{abc,s2}\right]=\left[R_{s2}\right]\cdot\left[I_{abc,s2}\right]+\frac{d}{dt}\left[\psi_{abc,s2}\right]; \quad (2)$$

$$\left[V_{abc,r}\right]=\left[R_{s1}\right]\cdot\left[I_{abc,r}\right]+\frac{d}{dt}\left[\psi_{abc,r}\right]. \quad (3)$$

The model is based on Park transformation of a three phase system of axes (*a*, *b*, *c*) a two-phase equivalent system of axes (*d*, *q*) creating the same magneto motive force. During the application of the *d-q* transformation and making the necessary manipulations, the equations (1) – (3) in *d-q* become

$$V_{ds1}=R_{s1}i_{ds1}+\frac{d\psi_{ds1}}{dt}-w_a\psi_{qs1}; \quad (4)$$

$$V_{qs1}=R_{s1}i_{qs1}+\frac{d\psi_{qs1}}{dt}+w_a\psi_{ds1}; \quad (5)$$

$$V_{ds2}=R_{s2}i_{ds2}+\frac{d\psi_{ds2}}{dt}-w_a\psi_{qs2}; \quad (6)$$

$$V_{qs2}=R_{s2}i_{qs2}+\frac{d\psi_{qs2}}{dt}+w_a\psi_{ds2}; \quad (7)$$

$$0=R_ri_{dr}+\frac{d\psi_{dr}}{dt}-(w_a-w)\psi_{qr}; \quad (8)$$

$$0=R_ri_{qr}+\frac{d\psi_{qr}}{dt}+(w_a-w)\psi_{dr}, \quad (9)$$

where w is speed of rotation of the coordinate (d, q) relative to the rotor; w_a is speed of rotation of the coordinate (d, q) relative to the stator 1.

Equations of flux are

$$\psi_{ds1}=L_si_{ds1}+L_{ps}i_{ds2}+Mi_{dr}; \quad (10)$$

$$\psi_{qs1}=L_si_{qs1}+L_{ps}i_{qs2}+Mi_{qr}; \quad (11)$$

$$\psi_{ds2}=L_si_{ds2}+L_{ps}i_{ds1}+Mi_{dr}; \quad (12)$$

$$\psi_{qs2}=L_si_{qs2}+L_{ps}i_{qs1}+Mi_{qr}; \quad (13)$$

$$\psi_{dr}=L_ri_{dr}+Mi_{ds1}+Mi_{ds2}; \quad (14)$$

$$\psi_{qr}=L_ri_{qr}+Mi_{qs1}+Mi_{qs2}, \quad (15)$$

where $L_s = L_{s1} = L_{s2} = l_{s1} + l_{sm} + L_m$ – the cyclic inductance of the stator; $L_r = l_r + L_m$ – the cyclic inductance of the rotor; $L_{ps} = l_{sm} + L_m$ – the cyclic mutual inductance between stator 1 and stator 2; L_m – the mutual inductance between stator 1, stator 2 and the rotor; l_{sm} – the mutual leakage inductance between stator 1 and stator 2; l_{s1}, l_{s2} – the stator leakage inductance; l_r – the rotor leakage inductance; R_s – the stator resistance; R_r – the rotor resistance.

The electromagnetic torque can be expressed as

$$C_{em}=n_p\frac{M}{L_r}\left[\left(i_{qs1}+i_{qs2}\right)\psi_{dr}-\left(i_{ds1}+i_{ds2}\right)\psi_{qr}\right]. \quad (16)$$

The analytical *d*-model is developed in a general reference frame and can be used to analyze the behavior of induction machine in any reference frame (Fig. 3).

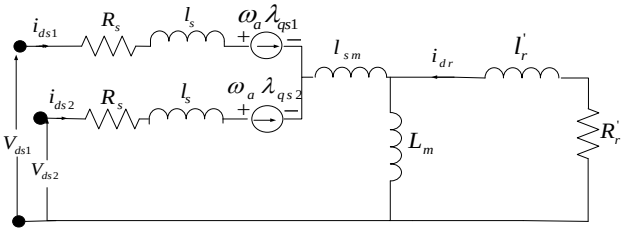

Fig. 3. d-axis equivalent circuit of a SPIM in arbitrary reference frame

The state equation of the form:

$$\dot{X}=AX+BU,$$

where

$X=\left[i_{ds1},i_{qs1},i_{ds2},i_{qs2},\psi_{dr},\psi_{qr}\right]$ – state vector;

$U=\left[V_{ds1},V_{qs1},V_{ds2},V_{qs2}\right]$ – input vector.

After a calculation, we obtain the following matrices

$$A=\begin{bmatrix} -\frac{a_{11}}{a_1} & w_a & -\frac{b_{11}}{a_1} & 0 & \frac{d_1}{a_1T_r} & \frac{d_1}{a_1}w \\ -w_a & -\frac{a_{11}}{a_1} & 0 & -\frac{b_{11}}{a_1} & -\frac{d_1}{a_1}w & \frac{d_1}{a_1T_r} \\ -\frac{b_{11}}{a_1} & 0 & -\frac{a_{11}}{a_1} & w_a & \frac{d_1}{a_1T_r} & \frac{d_1}{a_1}w \\ 0 & -\frac{b_{11}}{a_1} & -w_a & -\frac{a_{11}}{a_1} & -\frac{d_1}{a_1}w & \frac{d_1}{a_1T_r} \\ \frac{M}{T_r} & 0 & \frac{M}{T_r} & 0 & -\frac{1}{T_r} & (w_a-w) \\ 0 & \frac{M}{T_r} & 0 & \frac{M}{T_r} & -(w_a-w) & -\frac{1}{T_r} \end{bmatrix}; \quad (17)$$

$$B=\begin{bmatrix} \frac{1}{a_1} & 0 & -\frac{b_1}{a_1} & 0 \\ 0 & \frac{1}{a_1} & 0 & -\frac{b_1}{a_1} \\ -\frac{b_1}{a_1} & 0 & \frac{1}{a_1} & 0 \\ 0 & -\frac{b_1}{a_1} & 0 & \frac{1}{a_1} \\ 0 & 0 & 0 & 0 \\ 0 & 0 & 0 & 0 \end{bmatrix}, \quad (18)$$

where

$$a_1=\sigma_1 L_s-\frac{(\sigma_2 L_{ps})^2}{\sigma_1 L_s}, \quad b_1=\frac{\sigma_2 L_{ps}}{\sigma_1 L_s}, \quad c_1=\frac{\sigma_2 L_{ps}}{\sigma_1 T_s},$$

$$d_1=\left(1-\frac{\sigma_2 L_{ps}}{\sigma_1 L_s}\right)\frac{M}{L_r}, \quad a_{11}=R_s+\frac{d_1 M}{T_r}, \quad b_{11}=\frac{d_1 M}{T_r}-c_1,$$

$$\sigma_1=1-\frac{M^2}{L_s L_r}, \quad \sigma_2=1-\frac{M^2}{L_{ps} L_r}, \quad T_r=\frac{L_r}{R_r}, \quad T_s=\frac{L_s}{R_S}.$$

Simulation results of the SPIM with arbitrary displacements. In this section, the simulation results for the generalized theory of machine is presented. The dynamic performance behavior of the six-phase machine was determined, and implemented in Matlab/Simulink environment. This simulation results are generated in the Matlab/Simulink environment for the machine performance characteristics. The performance behavior of the machine was determined using the equivalent circuit. To observe the behavior of a six-phase induction machine, the nonlinear mixed model «stator current-rotor flux», which describes the SPIM, was analyzed and simulated. The machine used is characterized by a two poles, 250 V per phase, frequency 50 Hz, and nominal speed 2880 rpm. Figure 4 shows the block diagram necessary to undertake the simulation.

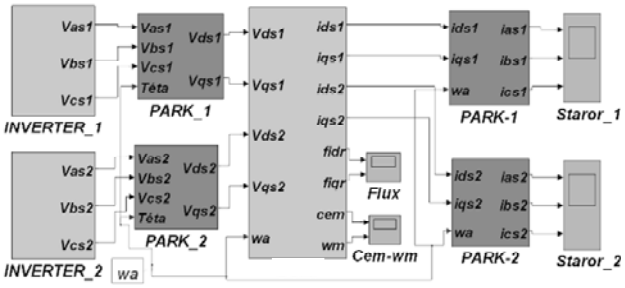

Fig. 4. Simulink structural scheme of six-phase induction machine model

The operating characteristics of the simulation test machine supplied by two identical voltage source inverters are illustrated at Fig. 5, 6 for the displacement angle 0°, 30° and 60° respectively.

The operating is characterized by an unloading start-up and then inserting the load torque from t = 1 s. In the Table 1 presents the torque ripple with different position of angle between the two stator.

Table 1

Torque ripple with displacement angle

Displacement	ΔC_{em}, %
α = 0°	9.4
α = 30°	3.1
α = 60°	9.4

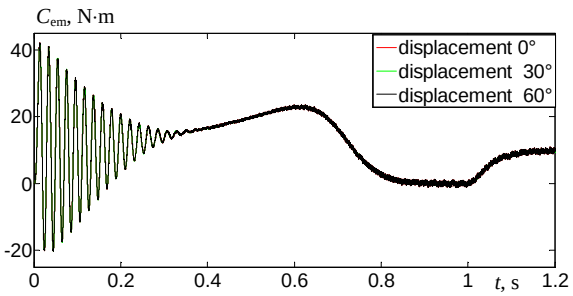

Fig. 5. Characteristic of the electromagnetic torque

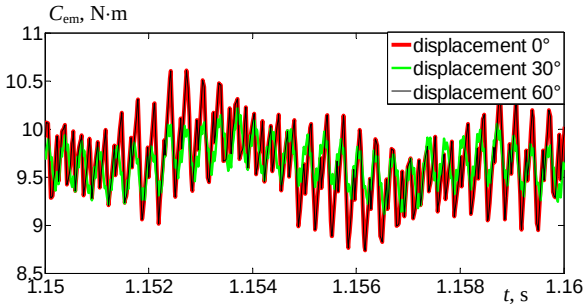

Fig. 6. Zoom on the steady state of electromagnetic torque

Heir it has been clearly shown through results that by varying displacement from low to high value we can minimize the total harmonic distortion (THD) of rotor currents (Fig. 7, 8). The variations in modulation index also affect the speed of six phase induction motor drive. There are fluctuations in the starting of rotor currents and electromagnetic torque.

The performance of a six phase induction motor operating under supply unbalance displacement (0°, 30°, 60°) show in the Fig. 7, 8.

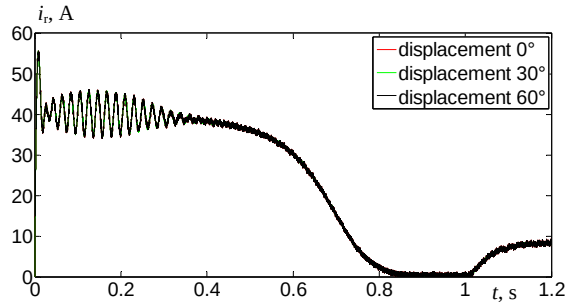

Fig. 7. Characteristic of rotor current i_r

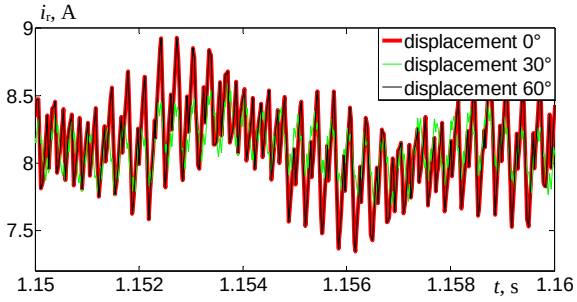

Fig. 8. Zoom on the steady state of rotor current

In Fig. 9, 10 we present the effect of the displacement in the stator current i_{as1}. This results investigates the significance of supply phase shift on the performance of a six induction motor by applying a novel phase shift unbalance definition to the negative and positive sequence components model of the SPIM. The test results reveal that when both phase angle shift and voltage magnitude unbalance occur simultaneously the effect of the phase shift dominates over the effects of the voltage magnitude unbalance. This study shows that phase angle unbalance has a severe consequence on six phase machine performance.

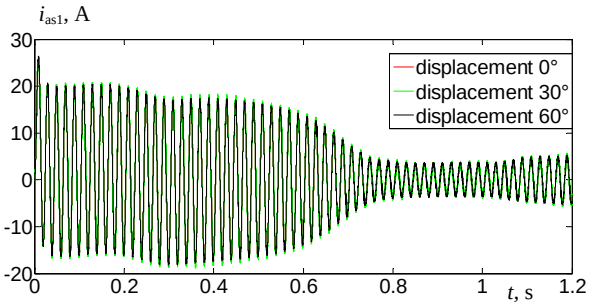

Fig. 9. Characteristic of stator current i_{as1} per phase «A»

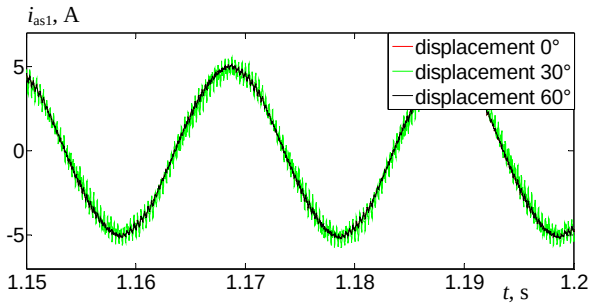

Fig. 10. Appearance of current i_{as1}

Simulation results of the SPIM fed by a multilevel inverter. We aim, in this section, to compare the quality of various wave quantities, namely the line to line voltages, winding currents and electromagnetic torque.

For each *m* level inverter, the simulation results will include the waves previously mentioned and their THD.

The inverters output voltages or winding voltages are displayed in Fig. 11. The number of levels generated by each inverter can be easily identified from the waveforms. The feeding voltages of the motor, represented in (*d*, *q*) axes, are function of the line to line multilevel inverter voltages shown in Fig. 11. These latter will be concerned by the following harmonics study.

During the starting, Fig. 12 shows the electromagnetic torque oscillating in the first moments. The transient torque may reach a peak of 5 N·m. At t = 0.5 s, a load torque of 3 N·m is applied. Besides, the impact of the inverter output voltage quality on the rotor torque is especially visible during the steady state.

In fact, Fig. 12 clearly illustrates that the torque ripple during steady state period decreases gradually and progressively as the inverter number of levels increases. Relative results are resumed in Table 2. It has to be emphasized that less torque ripple leads to better stability operation with minimum mechanical noise.

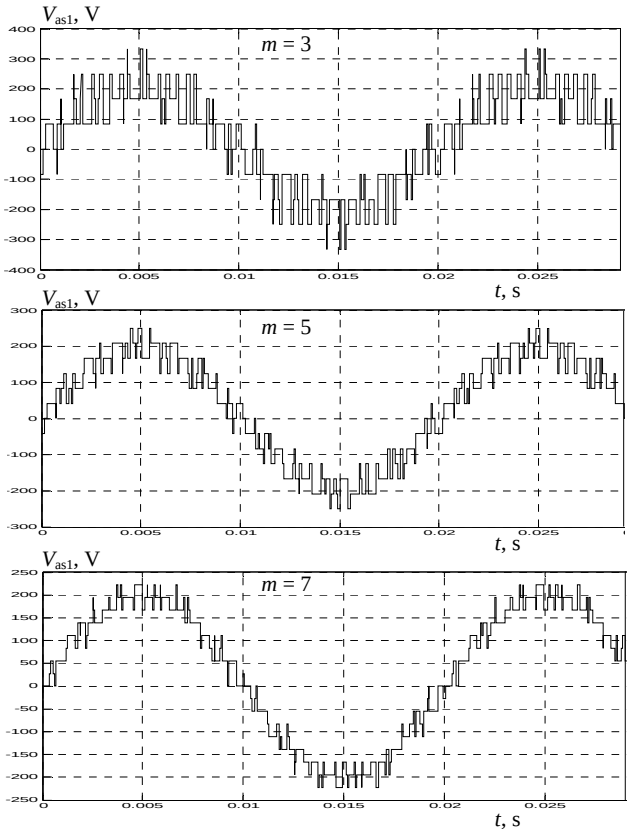

Fig. 11. Waveform of output voltage V_{as1} for m = 3, 5, 7

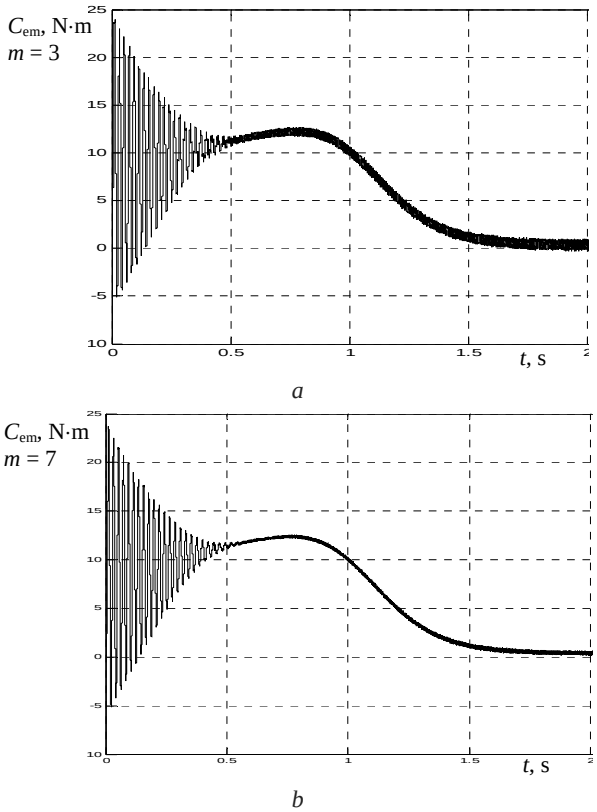

Fig. 12. Electromagnetic torque for m = 3 (*a*) and m = 7 (*b*)

In order to compare the quality of electromagnetic torque, Table 2 details ripple rate of 3 and 7 multilevel inverter output voltages. It also displays the THD corresponding to different voltage levels up to m = 7.

Table 2

Torque ripple with inverter levels number

Levels number	Relative torque ripple rate in %
m = 3	10.52
m = 7	4.96

Figure 13 gives the general shape of the absorbed current during the transient state. In addition, the steady state current, its spectral analysis and its THD are detailed. If the voltage level changes from m = 3 to m = 7, the THD drops from 4.03 % to 2.12 %. As can be seen, the THD varies slowly upper to 5 levels.

The stepped voltage waveform is composed by m levels, which depends on DC sources numbers, such that m = 2S +1. Thus, whatever is the type of cascaded multilevel inverter, the output voltage levels number is always odd (3, 5, 7, 11, ...).

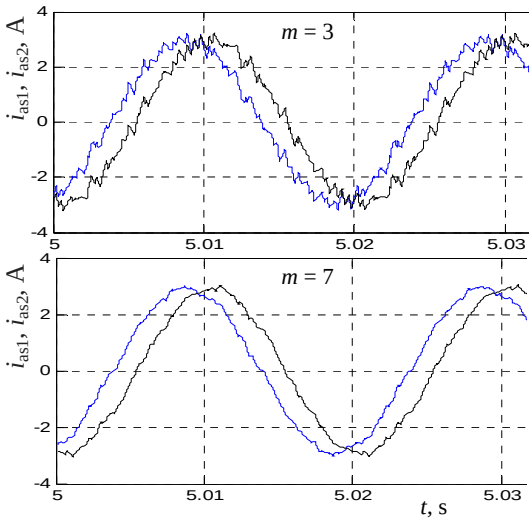

Fig. 13. Stator currents i_{as1}, i_{as2} for m = 3, 7 respectively

Conclusion.

This paper demonstrates the stepwise development of six phase induction machine model to simulate the starting and dynamic behaviors of six-phase split winding induction machines fed by multilevel inverter. The free acceleration characteristics as well as the dynamic response with level inverter variation were tested on the simulation and the results were likewise displayed. This paper also, has investigated the operational impact of supply phase shift on the performance of six-phase induction machine. The phase shift unbalance causes a reduction in motor efficiency, developed torque, and motor power factor. It also leads to undesirable increase in reactive power consumption, which increases energy cost. In the next work we will study the impact of the sensitivity of the mutual leakage flux of SPIM fed by multilevel inverter, we will consider three possible cases where first the mutual leakage flux is suitably modelled, second it is considered as a self-leakage flux and finally it is totally ignored.

REFERENCES

1. Singh G.K., Pant V., Singh Y.P. Voltage source inverter driven multi-phase induction machine. *Computers and Electrical Engineering*, 2003, vol. 29, no. 8, pp. 813-834. **doi: 10.1016/s0045-7906(03)00036-3.**

2. Abbas M.A., Christen R., Jahns T.M. Six-Phase Voltage Source Inverter Driven Induction Motor. *IEEE Transactions on Industry Applications*, 1984, vol. IA-20, no. 5, pp. 1251-1259. **doi: 10.1109/tia.1984.4504591**.

3. Gupta N., Singh Y. Stability and response of extremum seeking feedback scheme for squirrel cage induction generator based WECS. *International Journal of Advanced and Applied Sciences*, 2017, vol. 4, no. 6, pp. 50-55. **doi: 10.21833/ijaas.2017.06.007.**

4. Miranda R.S., Jacobina C.B., Lima A.M.N. Modeling and analysis of six-phase induction machine under fault condition. *2009 Brazilian Power Electronics Conference*, 2009, pp. 824-829. **doi: 10.1109/cobep.2009.5347696.**

5. Lipo T.A. A d-q model for six phase induction machine. *International Conference on Electrical Machines ICEM*, Athens, Greece, 1980, pp. 860-867.

6. Singh G.K., Singh D.K.P., Nam K., Lim S.K. A simple indirect field-oriented control scheme for multiconverter-fed induction motor. *IEEE Transactions on Industrial Electronics*, 2005, vol. 52, no. 6, pp. 1653-1659. **doi: 10.1109/tie.2005.858707.**

7. Pant V., Singh G.K., Singh S.N. Modeling of a multi-phase induction machine under fault condition. *Proceedings of the IEEE 1999 International Conference on Power Electronics and Drive Systems. PEDS'99* (Cat. No.99TH8475), 1999. **doi: 10.1109/peds.1999.794542.**

8. Zhao Y., Lipo T.A. Modeling and control of a multi-phase induction machine with structural unbalance. *IEEE Transactions on Energy Conversion*, 1996, vol. 11, no. 3, pp. 570-577. **doi: 10.1109/60.537009.**

9. Nelson R., Krause P. Induction machine analysis for arbitrary displacement between multiple winding sets. *IEEE Transactions on Power Apparatus and Systems*, 1974, vol. PAS-93, no. 3, pp. 841-848. **doi: 10.1109/tpas.1974.293983**.

10. Khlifi M.A. Analysis of an off-grid self-excited dual wound asynchronous generator for wind power generation. *International Journal of Advanced and Applied Sciences*, 2019, vol. 6, no. 6, pp. 35-42. **doi: 10.21833/ijaas.2019.06.006**.

11. Marwa B.S., Larbi K.M., Mouldi B.F., Habib R. Modeling and analysis of double stator induction machine supplied by a multi level inverter. *2012 16th IEEE Mediterranean Electrotechnical Conference*, March 2012, pp. 269-272. **doi: 10.1109/melcon.2012.6196430.**

12. Tuballa M.L., Abundo M.L.S. Microgrid simulation and modeling for a utility in southern Negros Oriental, Philippines. *International Journal of Advanced and Applied Sciences*, 2018, vol. 5, no. 7, pp. 86-96. **doi: 10.21833/ijaas.2018.07.011.**

13. Al Ahmadi S., Khlifi M.A., Draou A. Voltage and frequency regulation for autonomous induction generators in small wind power plant. *International Journal of Advanced and Applied Sciences*, 2019, vol. 6, no. 1, pp. 95-98. **doi: 10.21833/ijaas.2019.01.013.**

Received 22.06.2020

Ben Slimene Marwa, Ph.D, Assistant Professor,
College of Computer Science and Engineering,
University of Hail, Hail, Kingdom of Saudi Arabia,
22, Aljouf Str., Hail, Kingdom of Saudi Arabia, 8080.
e-mail: Benslimene.marwa@gmail.com

How to cite this article:
Ben Slimene M. Performance analysis of six-phase induction machine-multilevel inverter with arbitrary displacement. *Electrical engineering & electromechanics*, 2020, no. 4, pp. 12-16. **doi: 10.20998/2074-272X.2020.4.02.**

UDC 621.313.2:621.332.5 **doi: 10.20998/2074-272X.2020.4.03**

S.G. Buriakovskyi, A.S. Maslii, O.V. Pasko, V.V. Smirnov

MATHEMATICAL MODELLING OF TRANSIENTS IN THE ELECTRIC DRIVE OF THE SWITCH – THE MAIN EXECUTIVE ELEMENT OF RAILWAY AUTOMATION

Goal. ***To develop a mathematical and imitation model of the electric drive of the railroad switch as a two- and three-mass electromechanical system based on DC and AC motors as the main executive element of railway automation. The modelling is based on the parameters of the SP-6m switches as the main modification of the executive element of the Ukrainian domestic railways automation system.*** ***Methodology.*** ***The authors have presented the mechanical part of the railroad switch as a three-mass construction scheme with serial connection of elastic masses. Special attention is paid to the character of the movement of the switch point tongues, when describing them in the form of two- and three- mass kinematic schemes, as well as to the mechanical state of the traction and connections as nodes, which are most sensitive to the negative effects of some modes of the railroad switch.*** ***Results.*** ***A simulation mathematical model of SP-6m switch for AC and DC motors, which allows to study the influence of various factors, has been developed and tested at the stand of the Automation Laboratory of the Ukrainian State University of Railway Transport, Kharkiv. The deviation in the basic parameters of the switch translation process is less than 5 %.*** ***Originality.*** ***For the first time a mathematical model of an electric drive of the railroad switch is developed, which takes into account elastic relations and load characteristics as an object of controlling the speed of movement of switch point tongues.*** ***Practical significance.*** ***We have created a mathematical model of the electric drive of the railroad switch which allows to examine the influence of various factors, including the influence of the environment on the operation of the switch.*** References 10, table 1, figures 10.

Key words: **electric drive of the railroad switch; electromechanical switch system**.

Розроблено математичні моделі електроприводу стрілочного переводу у вигляді дво- і тримассовой електромеханічних систем на основі двигунів постійного і змінного струму як основного виконавчого елемента системи автоматизації залізниць. Відхилення модельних і експериментальних перехідних процесів для параметрів стрілочного переводу СП-6м не перевищують 5 %. Бібл. 10, табл. 1, рис. 10.

Ключові слова: **електропривод залізничного стрілочного переводу; електромеханічна система стрілочного переводу.**

Разработаны математические модели электропривода стрелочного перевода в виде двух- и трехмассовой электромеханических систем на основе двигателей постоянного и переменного тока как основного исполнительного элемента системы автоматизации железных дорог. Отклонения модельных и экспериментальных переходных процессов для параметров стрелочного перевода СП-6м не превышают 5 %. Библ. 10, табл. 1, рис. 10.

Ключевые слова: **электропривод железнодорожного стрелочного перевода; электромеханическая система стрелочного перевода.**

Introduction. The introduction of safe high-speed railway traffic on the main roads of Ukraine in accordance with the «National Transport Strategy of Ukraine for the Period up to 2030» directly depends on the infrastructure and conditions for ensuring traffic speeds: the condition of the rolling stock, railway track and automation systems. The main executive element of the railway automation systems, providing the throughput, is the turnout switch. Since the mathematical modelLing of the electric drive (ED) of the switch in railway transport has not received sufficient attention, there are practically no models of the electromechanical system (EMS) of the switch.

The goal of the work is the development of a mathematical and simulation model of a switch'selectric drive in the form of a two- and three-mass electromechanical system based on DC and AC motors as the main executive element of the railway automation system.

Research material. A serious problem in the study of switches' electric drives by the method of mathematical modelling was that in the known models the load was not taken into account and they were considered as single-mass electromechanical systems. Switches SP-6, as well as modifications based on them, are the most common in the railway transport system of Ukraine. The main structural elements of the switch are shown in Fig. 1: 1 – the body; 2 – the electric motor; 3 – the reducer with frictional connection 4 built in the same block; 5 – the main shaft with gate gear; 6 – the autoswitch block; 7 – the gate with cam locking mechanism.

The design features of the SP-6 switch and the disadvantages associated with them (the need for periodic adjustment of the friction protective device, the complexity of the autoswitch design, the presence of a technological clearance in the gear transmission of the gearbox), leads to an increase in the switching time, accelerated wear of the links of the kinematic system, which generally affects railway traffic safety.

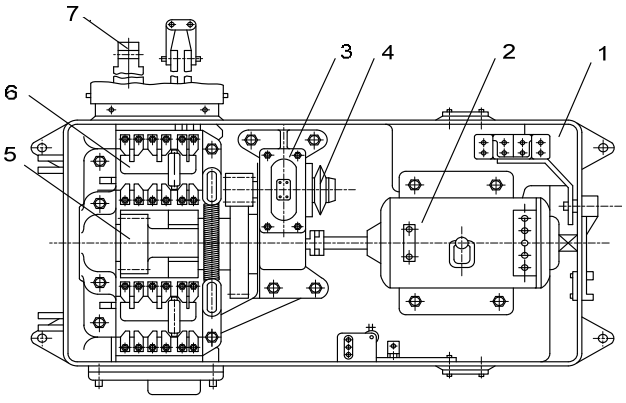

Fig. 1. Design of a of type SP-6m

© S.G. Buriakovskyi, A.S. Maslii, O.V. Pasko, V.V. Smirnov

The indicated disadvantages can be conditionally divided into mechanical (friction clutch, technological clearance) and electrical (position sensor, uncontrolled switching). To study the processes occurring in the switch's electric drive, it is proposed to consider it as an interconnected electromechanical system. Moreover, due to its design features, to study the effect of clearances and control methods on the reliability of the switching process, it is advisable to consider a switch as a multi-mass electromechanical system that takes into account the masses of an electric motor, wits and elastic connections.

For a two-mass electromechanical system (Fig. 2,*a*), the first mass J_1 is the total moment of inertia of the motor, gearbox and gate. The second mass m_2 is the total mass of wits and inter-edge thrust. The working thrust from the gate to the first blade serves as an elastic connection c_{12}. The transformation of the rotary motion of the motor shaft into the translational movement of the gate is carried out in the gearbox. The model takes into account the clearances in the kinematic transmission: the technological clearance φ_{tz} and the clearances l_z in the cotter-pin connections of the thrust attachment with the gate and the blade. The presence of an interstellar thrust in a two-mass system means the existence of elastic connections between the first and second witses. Therefore, further the authors consider the switch namely as a three-mass system (Fig. 2,*b*,*c*). The main reason for this approach is that the presence of elastic coupling elements has a serious impact on the dynamic processes in the mechanism [1-6], and the two-mass model is advisable to use for engineering calculations.

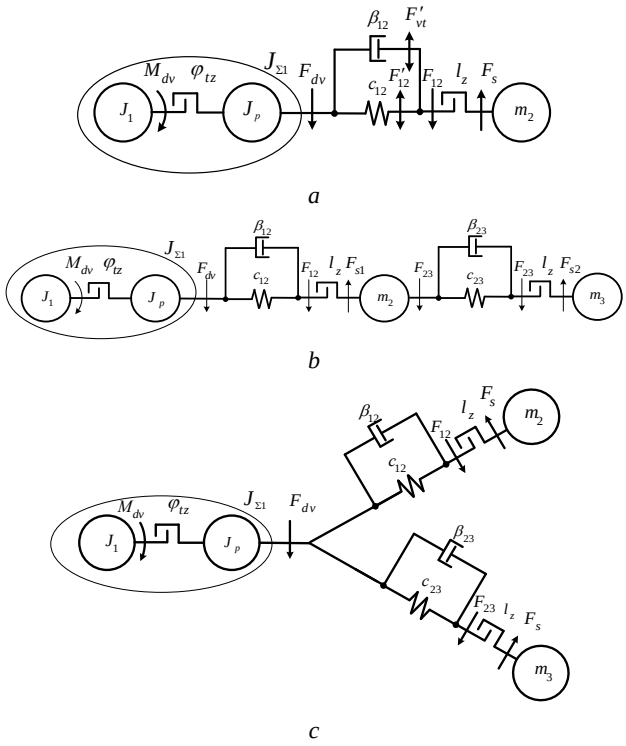

Fig. 2. Two-mass calculation scheme of the switch (*a*); three-mass calculation scheme of the switch with series connection of elastic masses (*b*); three-mass calculation scheme of the switch with parallel connection of elastic masses (*c*)

In the calculation scheme with series connection of elastic masses (Fig. 2,*b*) of such a system, the first mass, as before, is made up of the moments of inertia of the motor shaft and the moment of inertia of the gearbox reduced to the motor shaft. The second and third masses are the first and second wits, respectively; the interstitial thrust acts as an additional elastic connection c_{23}.

The kinematic diagram of the switch (Fig. 3) demonstrates that the working rod does not rest directly on the first wit, but is connected to it from the side of the second wit through the inter-turn rod. The authors consider it most expedient to consider the mechanical part of the switch as a three-mass design scheme with series connection of elastic masses, where: J_1 is the moment of inertia of the motor rotor; J_p is the moment of inertia of the gearbox, reduced to the motor shaft; $J_{\Sigma1}$ is the total moment of inertia of the first mass; M_{dv}, F_{dv} are the electromagnetic torque and thrust force of the motor, respectively; φ_{tz}, l_z are the technological clearance and clearance in the tie rods, respectively; F_{12}, F_{23} are the elastic forces in the working and inter-shaft rods, respectively; F_{s1}, F_{s2} are the resistance forces of the first and second wits, respectively; c_{12}, c_{23} are the elasticity of the working and interstellar rods, respectively; β_{12}, β_{23} are the coefficients of internal viscous friction of the working and inter-shaft rods, respectively; m_2, m_3 are the second and third masses, respectively (Fig. 2,*b*). The representation of the switch as a four-mass system is impractical.

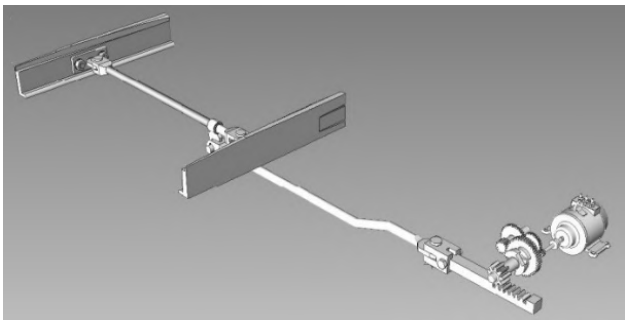

Fig. 3. Kinematic diagram of the SP-6m switch

When switching (Fig. 4), the wits 2 and 7, the connecting (inter-wit) thrust 3, the working thrust 4, the control 5 and 6 rods of the switch head and fastening parts move. The force of switching is spent on overcoming: the resistance of the moved parts along the switching surfaces 1 and the resistance in the hinges.

The force required to overcome the friction of the moving parts of the switch is determined by the friction force that occurs during movement. Its value can be determined as follows. Divide the switch into n equal elements of length l each. Let q_1, q_2, … q_k denote the weight of each element. The weight of the elements will be different both due to the change in the weight of the parts of the wits 2 and 7, and due to the presence or absence of connected rods, switch heads and other movable parts within the elements.

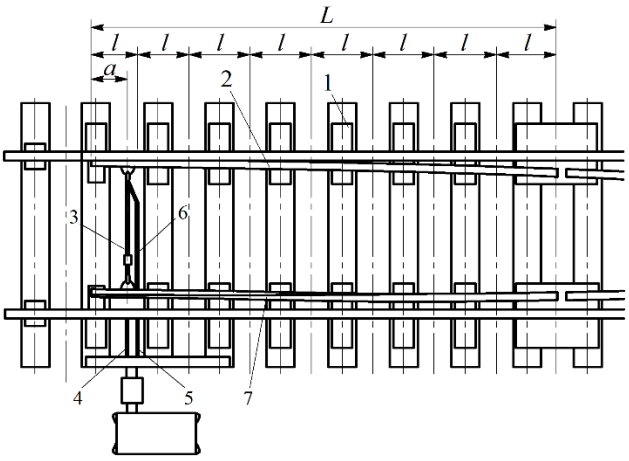

Fig. 4. General view of the mechanism for determining the effort of switching: 1 – switching surface; 2, 7 – wits; 3 – connecting thrust; 4 – working thrust; 5 – first control rod; 6 – the second control rod

Assuming that the wit lies not on separate pillows, but on a solid base and the coefficient of friction between the wit and the base is the same along the entire length of the wit and is equal to ψ, we find the elementary friction forces:

$$F_1 = \psi \cdot q_1, F_2 = \psi \cdot q_2, ..., F_k = \psi \cdot q_k. \quad (1)$$

Moments of elementary forces relative to the root of the wits:

$$M_1 = \psi \cdot q_1 \cdot \frac{1}{2} \cdot l,\ M_2 = \psi \cdot q_2 \cdot \frac{3}{2} \cdot l, ...,\ M_k = \psi \cdot q_k \cdot \frac{2k-1}{2} \cdot l\ . \quad (2)$$

Total moment of friction force:

$$M_1 = \sum_{k=1}^{n} M_k = \frac{1}{2} \cdot \psi \cdot l \cdot \sum_{k=1}^{n} q_1 + 3q_2 + ... + (2k-1)q_k. \quad (3)$$

Consequently, the force required to overcome the frictional forces of the moved parts, applied at a distance $L–a$ from the root (beginning) of the wit, is

$$F = \frac{M_T}{L-a} = \frac{1}{2} \cdot \psi \cdot \frac{l}{L-a} \cdot \sum_{k-1}^{n} q_1 + 3q_2 + ... + (2k-1)q_k. \quad (4)$$

For approximate calculations of the force F and assuming that $q_1 = q_2 = … = q_k = q$, we obtain:

$$F = \frac{1}{2} \cdot \psi \cdot q \cdot \frac{l}{L-a} \cdot \sum_{k=1}^{n} 1 + 3 + ... + (2k-1) = \frac{1}{2} \cdot \psi \cdot q \cdot n^2 \frac{l}{L-a}. \quad (5)$$

Since $L = l \cdot n$ and $Q = q \cdot n$, then

$$F = \frac{1}{2} \psi \cdot Q \frac{L}{L-a}, \quad (6)$$

where L is the wit length, Q is the total weight of the moving parts of the switch.

The coefficient taking into account the influence of friction forces in the joints is usually taken equal to 1.1 [7]. We determine the calculated effort of switching with a pivot or inlay-onlay mount according to the formula:

$$F = 1{,}1 \cdot \frac{1}{2} \psi \cdot Q \frac{L}{L-a} = 0{,}55 \cdot \psi \cdot Q \frac{L}{L-a}. \quad (7)$$

From (7) it follows that the switching force depends on the weight of the moving parts of the switch, the type of rails, the place of fixing the switching rods and the coefficient of friction of the wits on the pillows. All specified quantities, except for the last, are determinable.

The value of the coefficient of friction can range from 0.05 to 0.3 and depends on the condition of the switch, the quality of lubrication of the switch pads, the cleanliness of the treatment of their surfaces, as well as the soles of the wit and other factors.

Maintaining the clearances in the kinematic line (Fig. 5) of the switching within the limits set by the instructions plays one of the key roles in ensuring the safety of the switching of wit.

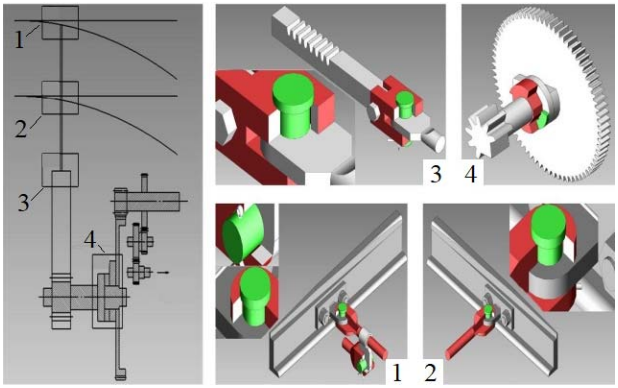

Fig. 5. Clearances in the kinematic line of the switch: 1, 2, 3 – at the points of attachment of the rods, 4 – technological clearance

Such a distance for the safe movement of the wheels of the rolling stock should be no more than 4 mm [8, 9], otherwise emergency situations may arise, such as «cutting the switch», which lead to the derailment of the rolling stock and the destruction of both the roadbed and the accompanying infrastructure. Due to the impact during the development of a technological clearance, works on friction and unregulated switching speed – the linkages of the rods gradually break and the clearances increase. Studies carried out on the railways of Latvia [8] have shown that the rate of increase in the size of the clearance is on average 0.05 mm per month (Table 1).

Table 1

Monthly increase in backlash at points of connection of switch thrusts

Connection place	Maximum increace in backlash (mm)	Average increace in backlash (mm)
Connecting inter-wits thrust – shackle	0.07	0.04
Connecting inter-wits thrust – working thrust	0.06	0.04
Working thrust – gate of the electric drive	0.09	0.05

The design feature of SP-6m switches is the presence of a 46° technological clearance between the third and fourth stages of the gearbox (Fig. 4, 5), which is necessary to facilitate the acceleration of the motor and its stock of some kinetic energy in order to break the wits at the beginning of the switching process [7]. The simulation of the mechanical part of the electric drive is carried out taking into account the real values of the clearances and the presence of the force of internal viscous friction.

The total elastic-viscous force is determined as:

$$F_{12} = \begin{cases} 0, \text{ if } \operatorname{sign}\Delta l \neq \operatorname{sign}\Delta v \text{ and } |F_{vt}| > |F'_{12}|; \\ F_{vt} + F_{12}, \text{ if } \operatorname{sign}\Delta l = \operatorname{sign}\Delta v \text{ and } |F_{vt}| \leq |F_{12}|, \end{cases} \quad (8)$$

where $F_{12} = c_{12} \cdot F_1(l)$ is the elastic force; $F_{vt} = \beta_{12} \cdot \Delta v \cdot F_2(l)$ is the viscous friction force; $F_1(l)$ and $F_2(l)$ are the nonlinear functions:

$$F_1(l) = \begin{cases} 0 & \text{at } |\Delta l| \leq \dfrac{\Delta l_3}{2}; \\ \Delta l - \dfrac{\Delta l_3}{2} & \text{at } \Delta l > \dfrac{\Delta l_3}{2}; \\ \Delta l + \dfrac{\Delta l_3}{2} & \text{at } \Delta l < -\dfrac{\Delta l_3}{2}, \end{cases} \quad (9)$$

$$F_2(l) = \begin{cases} 0 \text{ at } |\Delta l| \leq \dfrac{\Delta l_3}{2}; \\ 1 \text{ at } |\Delta l| > \dfrac{\Delta l_3}{2}. \end{cases} \quad (10)$$

In the three-mass model (Fig. 2,*b*), the elastic-viscous force F_{23} is determined in a similar way.

The implementation of the mathematical model was made in the environment for creating engineering applications Simulink of the MATLAB code. The model was created block by block, in full accordance with the calculation schemes (Fig. 2): motor block, reducer block, block of the first wit, block of the second wit. Clearances – technological one and two clearances in the joints reduced to the fastening of the first and second rail are marked with separate bloks.

The numerical values of the moments of inertia of the gear stages are calculated based on their weight and dimensions. For modelling, mechanical parameters of the working and connecting thrusts are also required – rigidities and viscous friction coefficients c_{12}, β_{12}, c_{23}, β_{23}, respectively. The thrust is a metal rod, the deformation of which occurs along the longitudinal axis:

$$c_{12} = c_{23} = E \cdot \frac{\pi \cdot \left(\dfrac{d}{2}\right)^2}{l}, \quad (11)$$

where E is the modulus of elasticity for steel; d is the thrust diameter диаметр тяги; l is the thrust length.

The rigidity of the working thrust in the model is taken to be equal to the rigidity of the direct connecting thrust due to the fact that these thrusts have the same length and diameter. On the basis of the research results [10], the value of the internal viscous friction coefficient is taken within the limits $1 \cdot 10^3 \ldots 1 \cdot 10^4$.

At present, schemes with both a DC motor (DCM) and an induction motor (IM) are widely used. Due to the possibility of powering the frequency converter (FC) both with DC directly from an autonomous voltage inverter and with AC of a rectifier, the system under development can be integrated into a switch control circuit based on both DCM, for example, sequential excitation motors of the types MSP-0,1, MSP-0,15 and MSP-0,25, which are widely used in Ukraine, and also IM.

Figure 6 shows a block diagram of a three-mass model of a switch with various configurations of a drive motor – DCM and IM.

The equations that describe the electromagnetic and electromechanical processes in the DCM of sequential excitation have the form:

$$\begin{cases} u = (L_a + L_v)\dfrac{di}{dt} + (r_a + r_v)i + e_a; \\ J\dfrac{d\omega}{dt} = M_d - M_s; \\ e_a = k \cdot \omega \cdot \Phi_v; \\ M_d = k \cdot i \cdot \Phi_v, \end{cases} \quad (12)$$

where $k = \dfrac{pN}{2\pi a}$ is the design factor.

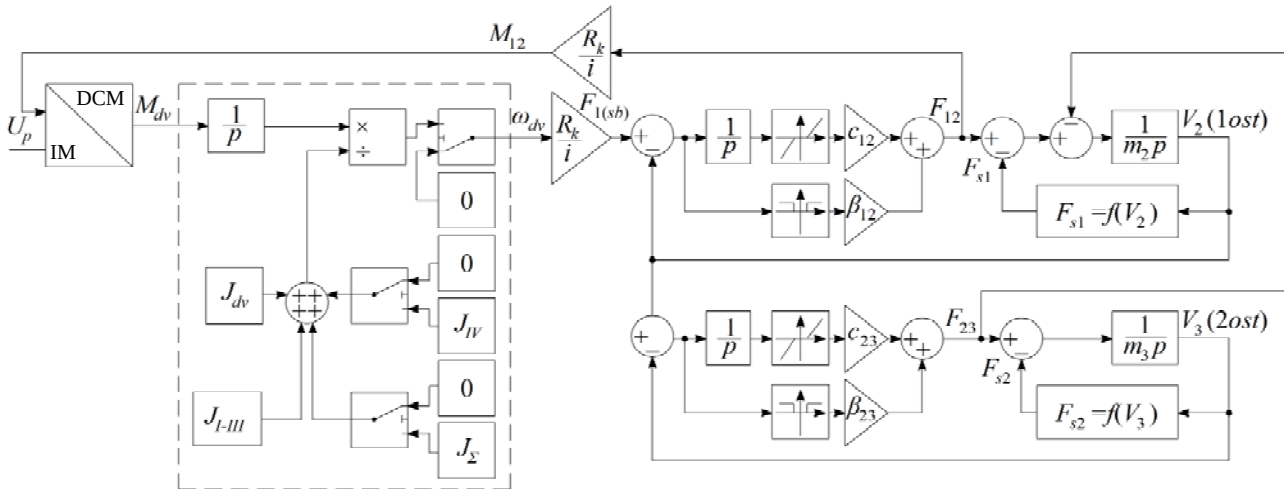

Fig. 6. Block diagram of a three-mass model of a switch with serial connection of masses

The model presented in this paper demonstrates ways of replacing the electric drive of a switch from a DCM to an IM with frequency control. As a solution, we propose a mathematical model of a switch based on a structural diagram (Fig. 6), where instead of a DCM/IM block, a FC-IM block is used. An induction motor is a nonlinear multidimensional object with a rather complex structure, therefore, the mathematical description and modelling of an electric drive with an IM differs from the given system of equations (12) for DCM. The equivalent circuit of the IM in the electric drive is shown in Fig. 7.

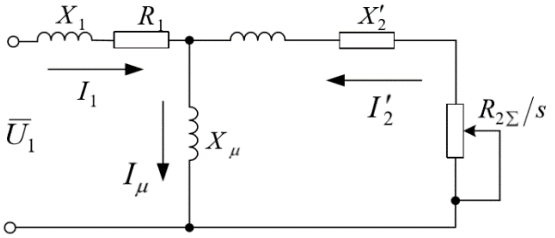

Fig. 7. Phase equivalent circuit of an induction motor

In the mathematical description of the IM, the adopted coordinate system, in which the mathematical description of the object is performed, and the configuration of the model, which depends on the content of the input and output signals of the model, the structure of the control system, and on the characteristics of the motor power source, are of great importance.

The basis for modelling of the configuration of an electric drive in this study was a coordinate system oriented along the rotor flux linkage. When carrying out the simulation, the following assumptions were made: the stator and rotor of a three-phase induction motor have symmetrical windings, the air gap is the same along the entire circumference of the rotor, the magnetic field in the air gap is sinusoidally distributed, the axes of the stator and rotor windings do not coincide, forming an arbitrary angle. To move from a mathematical description of harmonic signals in multiphase coordinates to a mathematical description in orthogonal two-phase coordinates, the concept of a generalized vector is used:

$$\boldsymbol{i} = \frac{2}{3}(i_A + \boldsymbol{a}\cdot i_B + \boldsymbol{a}^2 \cdot i_C), \tag{13}$$

where $\boldsymbol{a} = e^{j\frac{2\pi}{3}}$, $\boldsymbol{a}^2 = e^{j\frac{4\pi}{3}}$ are the vectors taking into account the spatial displacement of the windings;

$$i_A = I_m \cos\omega t,\ i_B = I_m \cos(\omega t - \frac{2\pi}{3}),\ i_c = I_m \cos(\omega t + \frac{2\pi}{3})$$

is the three-phase symmetrical system of stator currents.

Substituting the values of instantaneous currents into equation (13), we find a mathematical description of the spatial vector of the stator current:

$$\boldsymbol{i}_S = \frac{2}{3} I_m (\cos\omega t + e^{j\frac{2\pi}{3}} \cdot \cos(\omega t - \frac{2\pi}{3}) + e^{j\frac{2\pi}{3}} \times \times \cos(\omega t + \frac{2\pi}{3})) = I_m e^{j\omega t}. \tag{14}$$

Thus, for a coordinate system rotating at an arbitrary speed, the following system of equations can be written:

$$\begin{cases} \boldsymbol{u}_S = R_S \boldsymbol{i}_S + \dfrac{d\boldsymbol{\Psi}_S}{dt} + j\omega_k \boldsymbol{\Psi}_S; \\ \boldsymbol{u}_R = R_R \boldsymbol{i}_R + \dfrac{d\boldsymbol{\Psi}_R}{dt} + j(\omega_k - \omega_r)\boldsymbol{\Psi}_R; \\ \boldsymbol{\Psi}_S = L_S \boldsymbol{i}_S + L_m \boldsymbol{i}_R; \\ \boldsymbol{\Psi}_R = L_m \boldsymbol{i}_S + L_R \boldsymbol{i}_R; \\ M = \dfrac{3}{2} pk_R \cdot Mod(\boldsymbol{\psi}_R \times \boldsymbol{i}_S); \\ J\dfrac{d\omega_m}{dt} = M - M_n, \end{cases} \tag{15}$$

where $\omega = p\omega_n$; p is the number of pole pairs in the machine; J is the moment of inertia of the rotor.

For a squirrel-cage motor, the vectors $\boldsymbol{\Psi}_S$, $\boldsymbol{\Psi}_R$ differ from each other due to the presence of scattering of the stator and rotor windings. In this regard, the following is true for them:

$$\begin{aligned} \boldsymbol{\Psi}_S &= (L_m + L_{sl})\cdot \boldsymbol{i}_S + L_m \boldsymbol{i}_R; \\ \boldsymbol{\Psi}_R &= (L_m + L_{rl})\cdot \boldsymbol{i}_R + L_m \boldsymbol{i}_S, \end{aligned} \tag{16}$$

where L_m is the main leakage inductance; L_{sl}, L_{rl} are the leakage inductance of windings.

Here, for the inductances of the stator L_S and rotor windings L_R we have:

$$\begin{aligned} L_S &= (L_m + L_{sl}); \\ L_R &= (L_m + L_{rl}). \end{aligned} \tag{17}$$

When constructing real systems of an AC electric drive, coordinate converters are almost always included in the control system, which are necessary to recalculate real three-phase variables into two-phase model variables and vice versa. For the coordinate system α, β, the direct transformation is as follows:

$$i_A = i_\alpha,\ i_B = -\frac{1}{2} i_\alpha + \frac{\sqrt{3}}{2} i_\beta,\ i_C = -\frac{1}{2} i_\alpha - \frac{\sqrt{3}}{2} i_\beta, \tag{18}$$

and the opposite one:

$$i_\alpha = i_A,\ i_\beta = \frac{i_B - i_C}{\sqrt{3}}. \tag{19}$$

For modelling, the parameters of the SP-6m switch as the main modification of the executive element of the automation system for the domestic railways of Ukraine were taken as the initial data.

For further work with the simulation model, an assessment of its adequacy to the real object was carried out. For this, at the laboratory of the Ukrainian State University of Railway Transport, a Siemens FC was connected to the SP-6 drive and started with a rated load up to a rated speed according to a given tachogram. The results of the experiment on the stand (*a*) and on the model (*b*) are shown in Fig. 8. Analysis of the graphs allows to conclude that the operation of the model and the real object is identical, since the discrepancy in the coordinates of the current and speed is less than 5 %.

The obtained results of modelling of the operation of an electric switching drive with an AC motor are shown in Fig. 9.

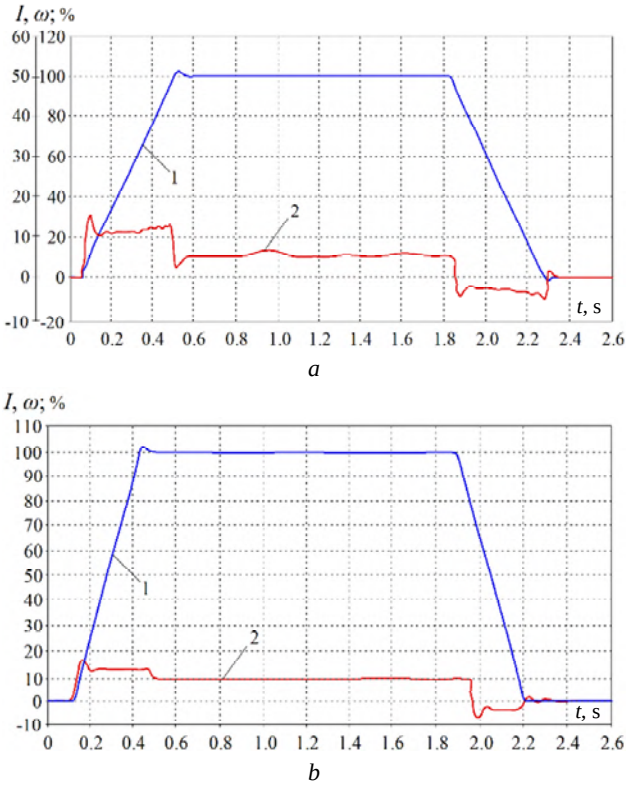

Fig. 8. Oscillogram of movement of the switching drive:
a – obtained on Siemens equipment;
b – mathematical model

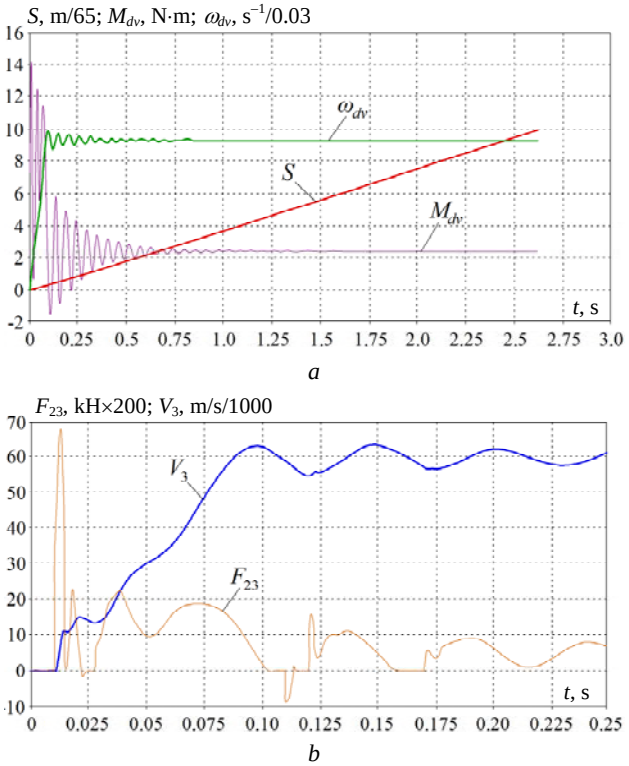

Fig. 9. Oscillograms of transients for a three-mass structure with series connection of masses: *a* - angular speed, displacement and torque of the IM; *b* – force and speed

The occurrence of oscillations in the kinematic line of the switch is confirmed by studies of the state of the switching surfaces, where wave-like traces are visible, which are formed as a result of elastic oscillations of the wits in the process of their switching (Fig. 10).

Fig. 10. State of the switching surfaces

The characteristic mats present on both pillows indicate the emerging elastic vibrations in both thrusts and lead to the vibrations of both wits, which confirms the need to consider the electric drive of the switch as a three-mass EMS. The depth and width of undulating formations, according to the observations of the service personnel, depends on the presence and magnitude of «backlashes» in the kinematic line of the switch.

Conclusions. For the first time, a mathematical and simulation model of an electric switching drive has been developed in the form of a two- and three-mass electromechanical system based on DC and AC motors as the main executive element of the automation system of Ukrainian railways. The initial data of the most common turnout switch SP-6m were taken as the object of modelling. The necessity of taking into account, when modelling an electromechanical system of a switch, the size of the clearances and the dynamics of their change in order to take into account the processes taking place in the mechanical subsystem, is shown. The spread of the deviation values of the main coordinates of the electric switching drive during transients, obtained by the method of simulation and experimentally, does not exceed 5 %.

REFERENCES

1. Kuznetsov B.I., Nikitina T.B., Kolomiets V.V., Bovdui I.V. Improving of electromechanical servo systems accuracy. *Electrical engineering & electromechanics*, 2018, no. 6, pp. 33-37. **doi: 10.20998/2074-272X.2018.6.04.**

2. Buriakovskyi S., Smirnov V., Asmolova L., Obruch I., Rafalskyi O., Maslii A. Analysis of optimization criteria for the process of switch displacement in a DC railroad turnout. *Eastern-European Journal of Enterprise Technologies*, 2019, vol. 6, no. 2 (102), pp. 58-69. **doi: 10.15587/1729-4061.2019.187580**.

3. Sokol Y.I., Buryakovskiy S.G., Masliy Ar.S. Energy-efficient electric drive of multifunctional turnout. *Problemy Kolejnictwa*, 2014, no. 165, pp. 99-107.
4. Lagos R.F., San Emeterio A., Vinolas J., Alonso A., Aizpun M. The influence of track elasticity when travelling on a railway turnout. *Proceedings of the Second International Conference on Railway Technology: Research, Development and Maintenance*, 2014, p. 11. **doi: 10.4203/ccp.104.208**.
5. Papacek F. Turnout of new construction. *International Railway Journal*, 2000, no. 3, pp. 30-32.
6. Krishnan R. *Switched reluctance motor drives. Modeling. simulation, analysis, design and applications*. CRC Press, 2001. 432 p. **doi: 10.1201/9781420041644.**
7. Resnikov J.M. Strelochnye elektroprivody elektricheskoj i gorochnoj centralizacii [Switch electric drives of electric and mining centralization]. Moscow. Transport Publ., 1975. – p.152.
8. *Latvian Railways Newsletter*. Available at: http://ita.times.lv/Automatika/Otzimi1.html (assessed 19 February 2020).
9. Gluzberg B.E. *Klassifikacija defektov i povrezhdenij elementov strelochnyh perevodov* [Classification of defects and damage to the elements of the switchgears]. Moscow. Transport Publ., 1996. 87 p. (Rus).
10. Akimov L.V., Kolotilo V.I., Markov V.S. *Dinamika dvuhmassovyh sistem s netradicionnymi reguljatorami skorosti i nabljudateljami sostojanija* [Dynamics of two-mass systems with non-traditional speed controllers and state observers]. Kharkiv, KhSPU Publ., 2000. 93 p. (Rus).

Received 22.05.2020

S.G. Buriakovskyi[1], *Doctor of Technical Science, Professor,*
A.S. Maslii[2], *Candidate of Technical Science, Associate Professor,*
O.V. Pasko[2], *Candidate of Technical Science, Associate Professor,*
V.V. Smirnov[3], *Candidate of Technical Science,*
[1] Scientific-&-Research Planning-&-Design Institute «Molniya», National Technical University «Kharkiv Polytechnic Institute»,
2, Kyrpychova Str., Kharkiv, 61002, Ukraine,
e-mail: sergbyr@i.ua
[2] Ukrainian State University of Railway Transport,
7, Feierbakh Square, Kharkiv, 61050, Ukraine,
e-mail: a.masliy@ukr.net, zamdek@kart.edu.ua
[3] Company «ELAKS»,
5a, build. 12, Ac. Proskura Str., Kharkiv, 61085, Ukraine,
e-mail: v.smirnov@elaks.kharkov.ua

How to cite this article:
Buriakovskyi S.G., Maslii A.S., Pasko O.V., Smirnov V.V. Mathematical modelling of transients in the electric drive of the switch – the main executive element of railway automation. *Electrical engineering & electromechanics*, 2020, no. 4, pp. 17-23. **doi: 10.20998/2074-272X.2020.4.03.**

UDC 621.3.013 **doi: 10.20998/2074-272X.2020.4.04**

B.I. Kuznetsov, T.B. Nikitina, I.V. Bovdui

SIMPLIFIED MATHEMATICAL MODEL OF GROUP OF OVERHEAD POWER LINES MAGNETIC FIELD

Aim. ***The method for design of simplified mathematical model of the group of overhead power lines magnetic field allowing to reduce the number of conductors which are taken into account in the model and field and allowing to reduce the sensitivity of the model to plant parameters uncertainty is developed.*** ***Methodology.*** ***The method based on the multi-criteria game decision, in which the payoff vector is calculated on the basis of the Maxwell equations quasi-stationary approximation solutions. The game decision based on the stochastic particles multiswarm optimization algorithms. The implementation of the method is carried out when determining the number, configuration, spatial arrangement and currents in conductors based on simplified mathematical model of the group of overhead power line magnetic field in a given space area.*** ***Results.*** ***Computer simulation and field experimental research results of simplified mathematical model on the example of the group of four overhead power lines magnetic field including 21 conductors where based on the developed simplified mathematical model of the magnetic field, the number of conductors taken into account in the model is reduced to 6, and the modeling error does not exceed 4 %.*** ***Originality.*** ***For the first time the method for design of simplified mathematical model of the group of overhead power lines magnetic field based on the stochastic particles multiswarm optimization algorithms, which allows to significantly simplify the simulation by reducing the number of conductors that are taken into account in the model and to reduce the sensitivity of the model to plant parameters uncertainty, and at the same time limit the modeling error at the engineering level to 5-10 %.*** ***Practical value.*** ***Practical recommendations on reasonable choice of the minimal number, configuration, spatial arrangement and currents in conductors for the simplified mathematical model of the group of overhead power line magnetic field.*** References 32, figures 6.

Key words: **overhead power lines, magnetic field, simplified mathematical model, computer simulation, field experimental research.**

Цель. ***Разработан метод построения упрощенной математической модели магнитного поля группы воздушных линий электропередачи, позволяющий уменьшить количество проводников, которые учитываются в модели для снижения чувствительности модели к неопределенности параметров объекта управления.*** ***Методология.*** ***Метод основан на решении многокритериальной стохастической игры, в которой векторный выигрыш вычисляется на основании решений уравнений Максвелла в квазистационарном приближении. Решение игры находится на основе алгоритмов стохастической мультиагентной оптимизации мультироем частиц. Реализация метода осуществляется при определении количества, конфигурации, пространственного расположения и токов в проводниках на основе упрощенной математической модели магнитного поля группы воздушных линий электропередачи в заданной области пространства.*** ***Результаты.*** ***Приводятся результаты компьютерного моделирования и полевых экспериментальных исследований на примере группы из четырех воздушных линий электропередачи, содержащей 21проводник, где на основе разработанной упрощенной математической модели магнитного поля количество учитываемых в модели проводников уменьшено до 6, а погрешность моделирования при этом не превышает 4 %.*** ***Оригинальность.*** ***Впервые разработан метод построения упрощенной математической модели магнитного поля группы воздушных линий электропередачи на основе алгоритмов стохастической мультиагентной оптимизации мультироем частиц, позволяющий существенно упростить моделирование за счет уменьшения количества проводников, которые учитываются в модели для снижения чувствительности модели к неопределенности параметров объекта управления, и при этом ограничить погрешность моделирования на инженерном уровне 5-10 %.*** ***Практическая ценность.*** ***Приводятся практические рекомендации по обоснованному выбору минимального количества, конфигурации, пространственного расположения и токов в проводниках упрощенной математической модели магнитного поля, создаваемого группой воздушных линий электропередачи.*** Библ. 32, рис. 6.

Ключевые слова: **воздушная линия электропередачи, магнитное поле, упрощенная математическая модель, компьютерное моделирование, полевые экспериментальные исследования.**

Introduction. The World Health Organization stated that exposure to extremely low frequency magnetic field (MF) at power frequencies 50-60 Hz could lead to an increased incidence of cancer. This leads to modern world trends on stricter sanitary standards for the power frequency MF. In particular, in Ukraine the reference level is 0.5 μT for living space [1]. Many of overhead power lines (OPL) often pass in the residential areas and generated a MF, the level of which often exceeds Ukraine sanitary standards, that poses a threat to public health [2, 3].

Ukraine's electricity networks are characterized by high density, and especially near high-voltage power substations. There is usually a group of overhead OPL, in the immediate vicinity of which can be located residential buildings. As an example in Fig. 1 is shown a photograph of the location of 4 group of OPL including 21 conductors, generating MF, the magnetic flux density level of which must be reduced in the considered space.

Fig. 1. Group of high voltage power lines

Active contour shielding methods are most economical for securing sanitary standards [3]. The systems of active shielding (SAS) synthesis method

© B.I. Kuznetsov, T.B. Nikitina, I.V. Bovdui

developed in [4-9]. In SAS usually use simultaneous open loop and closed loop control – two degree of freedom system [10-14].

The initial data for the synthesis of the SAS are the parameters of the transmission lines (working currents, geometry and number of wires, location of the transmission lines relative to the protected space) and the dimensions of the shielding space and magnetic flux density sanitary standards level, which should be achieved as a result of shielding [15-22].

The complexity of the synthesis problem solving of SAS is determined by the number of OPL conductors. Naturally, taking into account all OPL conductors that generated MF in the shielding zone, the task of synthesizing the SAE is complicated.

Therefore, it is relevant the approach to synthesis of SAS, which makes it possible to simplify the solution to the synthesis problem by taking into account a smaller number of wires in comparison with the original problem.

In this approach, the problem of approximating of the initial MF measured as a result of experimental studies with the help of several wires is solved. Depending on the required accuracy of approximation, the number of wires taken into account can be reduced to six, three or even two wires, which can significantly simplify the solution to the problem of synthesis of SAS.

The SAS plant parameters are known uncertainty [22-28]. In this case, the main uncertainty in the synthesis of this SAS is the variation of the bus currents in different OPL, which leads not only to a change in the magnetic flux density level, but also to a change in the position of the space-time characteristics (STC) of the MF in the shielding space due to the relative redistribution of the vertical and horizontal components of the magnetic flux density vector generated by various power lines. Therefore, the such simplified mathematical model of the initial magnetic field must be robust [22-28].

The goal of this paper is to develop the method for designing of mathematical model of the group of overhead power lines magnetic field, which allows to significantly simplify the simulation and at the same time limit the modeling error at the engineering level of 5-10 %.

Problem statement. Let us first consider the initial mathematical model of a magnetic field generated by group of OPL. In the future, we will call this model accurate. Consider the group of OPL consisting of K OPL. Each K OPL consists from L_k wires. At first, we conduct experimental research of the magnetic flux density level both in the shielding space and near the power transmission line. Based on the obtained data, we solve the problem of identifying currents in initial OPL wires, at which the sum of the squared errors of the measured and model values of the magnetic flux density at given points is minimized.

Based on the calculated current wires levels we set the instantaneous current value $I_{lk}(t)$ at time t in l_k wire in k OPL in the following form

$$I_{lk}(t) = A_{lk}\sin(\omega t + \varphi_{lk}). \qquad (1)$$

Consider the l_k wire of any rather complex configuration with an instantaneous current value $I_{lk}(t)$ at time t in the form of n vector elementary segments $\mathbf{\Delta L}_i$ of sufficiently short length. Then the total magnetic flux density vector $\boldsymbol{B}_{lk}(Q_i, I_{lk}(t))$ at the considered point Q_i, generated by n elementary segments of a l_k wire with an instantaneous current value $I_{lk}(t)$ can be determined [2, 3] on the basis of a quasistationary solution of the Maxwell equation in the following form

$$\boldsymbol{B}_{kl}(Q_j, I_{lk}(t)) = \frac{\mu_0 I_{lk}(t)}{4\pi}\sum_{i=1}^{n}\frac{\mathbf{\Delta L}_i \times \boldsymbol{R}_i}{|R_i|^3}, \qquad (2)$$

where μ_0 is the vacuum permeability, $\mathbf{\Delta L}_{ix}$ – vector differential element at the direction of current; $\boldsymbol{R}_i$ – vector whose magnitude $|R_i|$ is the distance from the source to the observation point Q_i.

Then the total magnetic flux density vector $\boldsymbol{B}(Q_i, \boldsymbol{I}(t))$ at the point Q_i, generated by all L_k wires by all K OPL can be represented as follows

$$\boldsymbol{B}(Q_j, I(t)) = \sum_{k=1}^{K}\sum_{l=1}^{L_k}\boldsymbol{B}_{kl}(Q_j, I_{lk}(t)), \qquad (3)$$

where the vector of instantaneous currents $I(t)$ at time t of all L_k wires of all K OPL is introduced, whose components are instantaneous current value $I_{lk}(t)$ at time t of l_k wire.

We introduce the vector $\boldsymbol{X}$ of the required parameters, the components of which are the number, configuration, spatial arrangement and currents in conductors of overhead power lines for the simplified mathematical model of the initial magnetic field.

Then for simplified mathematical model the total magnetic flux density vector $\boldsymbol{B}_M(Q_i, I_{Mlk}(t))$ at the same point Q_i, generated by all L_{Mk} wires of model can be represented as follows

$$\boldsymbol{B}_M(Q_j, \boldsymbol{X}, \boldsymbol{I}_M(t)) = \sum_{k=1}^{K}\sum_{l=1}^{L_k}\boldsymbol{B}_{Mkl}(Q_j, \boldsymbol{X}, \ldots \\ \ldots, \boldsymbol{I}_{Mlk}(t)), \qquad (4)$$

in which the total magnetic flux density vector $\boldsymbol{B}_{Mlk}(Q_i, I_{Mlk}(t))$ at the considered point Q_i, generated by n elementary segments of a l_{Mk} wire of model with an instantaneous current value $I_{Mlk}(t)$ can be determined [13] on the basis of a quasistationary solution of the Maxwell equation coherently (1).

The vector of instantaneous model currents $\boldsymbol{I}_M(t)$ at time t of all L_{Mk} wires of model is introduced, whose components are instantaneous current value $I_{Mlk}(t)$ at time t of l_k wire.

Consider the magnetic flux density vector $\boldsymbol{E}(Q_i, \boldsymbol{X}, I_M(t), I(t))$ of error between the initial magnetic flux density vector $\boldsymbol{B}(Q_i, I(t))$ and magnetic flux density vector $\boldsymbol{B}_M(Q_i, I_M(t))$ of approximate mathematical model at the considered points Q_j at time t

$$\boldsymbol{E}(Q_j, \boldsymbol{X}, \boldsymbol{I}_M(t), \boldsymbol{I}(t)) = \boldsymbol{B}(Q_j, \boldsymbol{I}(t)) - \ldots \\ \ldots - \boldsymbol{B}_M(Q_j, \boldsymbol{X}, \boldsymbol{I}_M(t)). \qquad (5)$$

To estimate the simplified mathematical model error we calculate the effective value $E(Q_i, \boldsymbol{X})$ of the error vector $\boldsymbol{E}(Q_i, \boldsymbol{X}, \boldsymbol{I}_M(t), I(t))$ by numerically integrating the squared modulus of the error vector over the time interval T = 20 ms of the period of the magnetic flux density vector change

$$E(Q_i, \boldsymbol{X}) = \frac{\sqrt{2}}{2}\sqrt{\frac{1}{T}\int_0^T \left|\boldsymbol{E}(Q_i, \boldsymbol{X}, \boldsymbol{I}_M(t), \boldsymbol{I}(t), t)\right|^2 dt}\,. \quad (6)$$

Method or designing. In the designing of the simplified mathematical model (3), the mathematical model of the original MF (2) is known inaccurately [19, 20]. In particular, currents in current conductors that have daily, weekly, seasonal variations are approximately known. Therefore, we introduce a vector $\boldsymbol{\delta}$ of the uncertainty parameters from their nominal values used in the design of the approximate mathematical model. Then the problem of design of the robust approximate the mathematical model is reduced to the determination of such a vector $\boldsymbol{X}$ of the required parameters, the components of which are the number, configuration, spatial arrangement and currents in conductors of overhead power lines for the approximate robust mathematical model of the initial magnetic field and the vector of uncertainty parameters $\boldsymbol{\delta}$, at which the maximum value of the magnetic field induction at selected points P_i of the considered space P assumes a minimum value for the required parameter vector $\boldsymbol{X}$, but the maximum value for the vector of uncertainty parameters δ so that

$$\boldsymbol{X}^* = \arg \min_{\boldsymbol{X}\in\boldsymbol{X}} \max_{\boldsymbol{\delta}\in\boldsymbol{\Delta}} \max_{Q_i\in\boldsymbol{Q}} E(\boldsymbol{X}, \boldsymbol{\delta}, Q_i)\,. \quad (7)$$

This technique corresponds to the standard approach to the design of robust systems for the worst-case [29], when the uncertainty parameters δ lead to the greatest deterioration of the approximated model accuracy.

The problem (7) can formulated in the form of the following multi objective game [30-32] with vector payoff

$$\boldsymbol{E}(\boldsymbol{X}, \boldsymbol{\delta}) = \left[E(\boldsymbol{X}, \boldsymbol{\delta}, Q_1), E(\boldsymbol{X}, \boldsymbol{\delta}, Q_2)\ldots \right.$$
$$\left.\ldots E(\boldsymbol{X}, \boldsymbol{\delta}, Q_m)\right]^T, \quad (8)$$

the components of which $E(\boldsymbol{X}, \boldsymbol{\delta}, Q_i)$ are the error between the initial magnetic flux density and magnetic flux density of approximate mathematical model in the m points Q_i of the space under consideration.

In the multi-objective game (8), the first player is the parameter vector of the approximate mathematical model $\boldsymbol{X}$ and its strategy is the minimization of the vector payoff and the second player is a vector $\boldsymbol{\delta}$ of uncertainty parameters and the strategy of this player is maximization of the same vector payoff [32].

Note that the components of the vector payoff (2) are nonlinear functions of the required parameters vectors $\boldsymbol{X}$ and $\boldsymbol{\delta}$ are calculated on the basis of the Maxwell equations solutions in the quasi-stationary approximation [2, 3].

To find the multi-criterion games decision from Pareto-optimal decisions [30] taking into account the preference relations [31], we used special nonlinear algorithms of stochastic multi-agent optimization [32].

Computer simulation results. Consider the results of designing of the simplified mathematical model of a magnetic field generated by group of OPL including 21 conductors. In Fig. 2 are shown layout of group OPL and shielding space. The initial MF in the shielding space generated by two double-circuit 110 kV OPL (OPL-1 and OPL-2), a two-circuit 330 kV OPL (OPL-3) and a single-circuit 330 kV OPL (OPL-4).

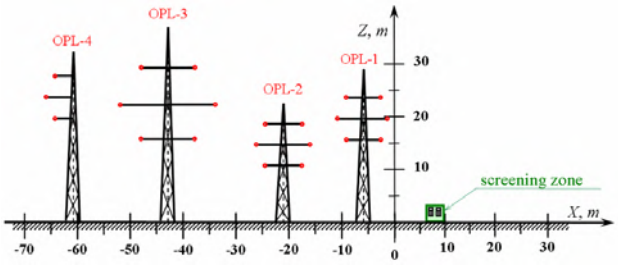

Fig. 2. Layout of group OPL and shielding space

In Figure 3 are shown the isolines of magnetic flux density, calculated for the nominal currents of group of OPL.

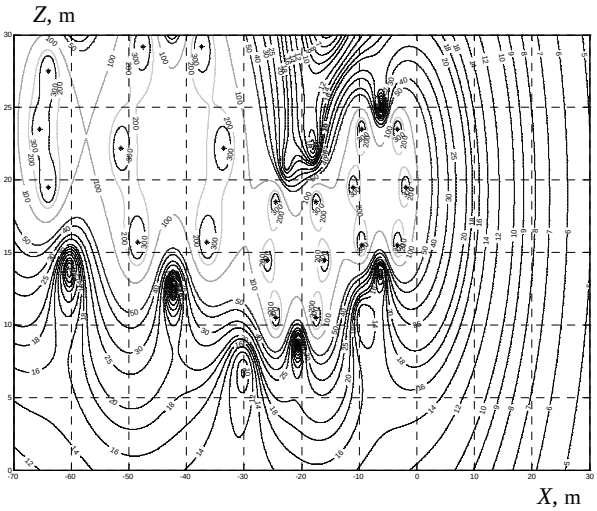

Fig. 3. The isolines of magnetic flux density, calculated for the nominal currents of group of OPL

Modeling of the magnetic flux density created by individual OPL in the shielding space carried out. The currents in the wires of all OPL were assumed to be the same and equal to 500 A. In Fig. 4 are shown the results of calculations of the distribution of the magnetic flux density in the shielding space during operation: *a*) only one OPL-4; *b*) during the operation of two OPL-3 and OPL-4; *c*) during operation of three OPL-2, OPL-3 and OPL-4; and *d*) during operation of four OPL-1, OPL-2, OPL-3 and OPL-4.

Based on the analysis of the dependencies are shown in Figure 4 shows that as the OPL is removed from the shielding space, the magnetic flux density level of generated by this OPL in the shielding space decreases.

However, in the case under consideration, the nominal currents in the OPL-3 and OPL-4 are 2000 A, but the nominal currents in OPL-1 and OPL-2 are 1000 A. Therefore, despite the fact that OPL-3 and OPL-4 are removed from the shielding space at a greater distance than OPL-1 and OPL-2, the influence of OPL-4 and, especially, OPL-3 on the magnetic flux density level in the shielding space can be significant.

Depending on the required accuracy of approximation robust mathematical model the number of power transmission wires taken into account can be reduced to six, three or even two wires. By dint of

approximation robust mathematical model in which only two current wires are taken into account, it is possible to simulate only weakly polarized field, in which the space-time characteristic is a strongly elongated ellipse. If the space-time characteristic of the initial magnetic field is close to a circle, then the minimum number of wires is two.

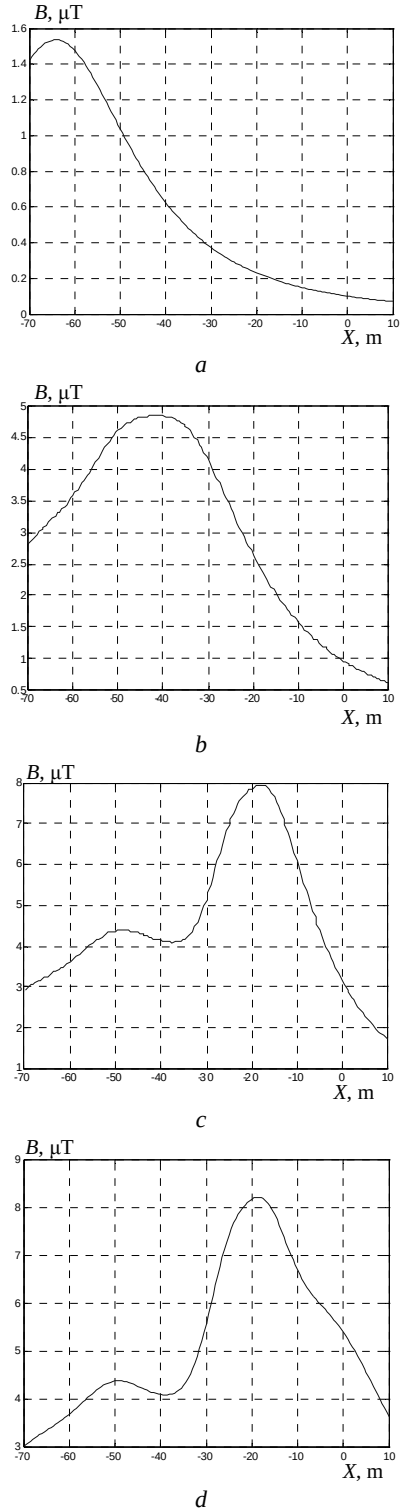

Fig. 4. The magnetic flux density distribution in the shielding space during operation:
a) only one OPL-4;
b) both OPL-3 and OPL-4;
c) OPL-2, OPL-3 and OPL-4;
d) all OPL-1, OPL-2, OPL-3 and OPL-4

Experimental research. Experimental research of the magnetic field generated by these group of OPL in the shielding space, in which it is necessary to reduce the MF level to sanitary standards, are shown that the values of magnetic flux density calculated at the nominal values of power line currents and measured values are very different.

Therefore, initially, based on experimental research of magnetic flux density generated by currents in 21 conductors of the 4 group of OPL were determined. For these currents, the original accurate model of MF (2) is constructed. The approximated model (3) was designing for this accurate model. The simplified model include 6 conductors.

In Fig. 5 are shown the isolines of magnetic flux density of simplified model of the magnetic field generated by group of OPL.

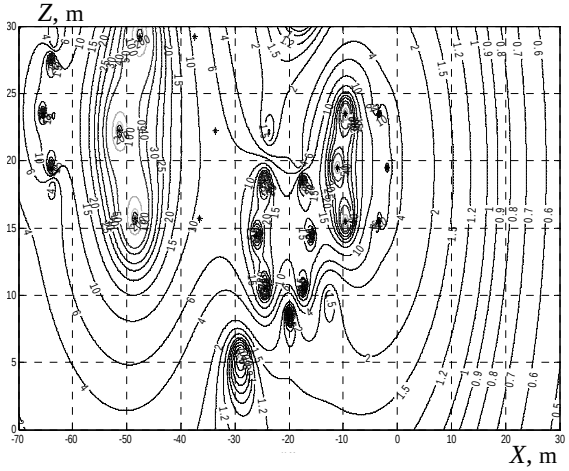

Fig. 5. The isolines of magnetic flux density of approximated model of the magnetic field generated by group of power lines

In Figure 6 are shown the dependences of the magnetic flux density of 1) simplified model and 2) measured values. A comparison of the results of modeling and experimental research of the distribution of magnetic flux density values in the shielding space showed that the error between such an simplified model and experimental measured values of the magnetic flux density level does not exceed 4 %.

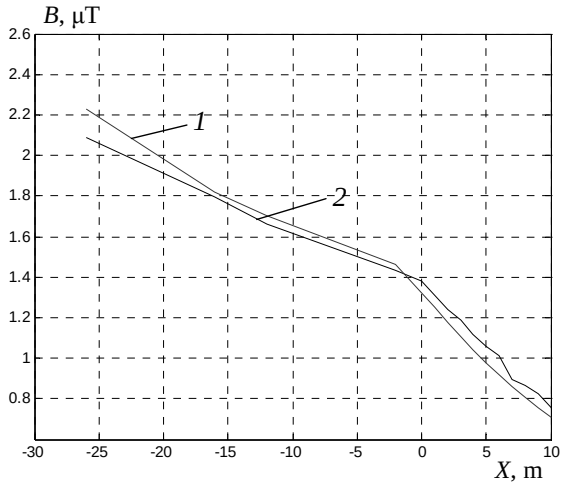

Fig. 6. The dependences of the magnetic flux density of *1* – approximated model and *2* – measured values

In addition, this simplified model use for the synthesis of SAS. Results of comparison of modeling and experimental research confirms the possibility of active shielding of the initial MF in the shielding space with the shielding factor more than 4.

In conclusion, we note that designing of simplified mathematical model of the initial magnetic field is equivalent to synthesis of system of active shielding of magnetic field. When designing of simplified mathematical model, it is necessary to determine the number, configuration, spatial arrangement and currents in conductors of overhead power lines for the simplified mathematical model of the initial magnetic field. This is the vector game solution.

When synthesis of system of active shielding of magnetic field, it is also necessary to determine the number, configuration, spatial arrangement and shielding coils currents, and the control systems parameters**.** This is also the vector game solution.

The components of the game vector payoff in the design of the approximate mathematical model are errors between the magnetic flux density level of the initial and approximated moles. And the components of the game vector payoff in the design of the of system of active shielding of magnetic field are the errors of screening of the initial magnetic field by the screening coils of the system of active shielding of magnetic field.

Therefore, when calculating the components of the game vector gain for designing of simplified mathematical model, it is enough to change the sign in the expression for to calculate the components of the game vector payoff in the design of the system of active shielding of magnetic field.

Therefore, from the point of view of the mathematical statement of the problems of designing of simplified mathematical model and synthesis of robust system of active shielding of magnetic field are tasks of approximating of the initial magnetic field. However, when designing of the simplified mathematical model, the wires are located in the zone of the power transmission line, but when designing the system of active shielding of magnetic field, the shielding coils are located near the shielding space.

Conclusions.

1. For the first time the method of design of simplified mathematical model of the group of overhead power lines magnetic field which can significantly simplify the simulation and at the same time limit the modeling error at the engineering level of 5-10 % is develop. The method based on reducing the number of conductors that are taken into account in the model and on reducing the sensitivity of the model to plant parameters uncertainty. Depending on the required accuracy of simplified mathematical model the number of power transmission wires taken into account can be reduced to six, four, three or even two.

2. The design of simplified mathematical model based on multi-criteria stochastic game decision, which is calculated by multiswarm stochastic multi-agent optimization from Pareto-optimal solutions. Multi-criteria game vector payoff is calculated based on the Maxwell equations solution. The number, configuration, spatial arrangement and currents in conductors of overhead power lines for the simplified mathematical model and resulting magnetic flux density value in the shielding space are determined by the simplified model designing.

3. The results of computer modeling and field experimental studies on an example of a group of four overhead power lines containing 21 conductors confirm the correctness of the developed simplified mathematical model and the possibility of reducing the number of conductors taken into account in the model to 6 while limiting the modeling error to level of 4 %.

4. It shown, that it is equivalent from the point of view of the mathematical statement the problems of designing of simplified mathematical model and synthesis of system of active shielding of magnetic field are tasks of approximating of the initial magnetic field.

REFERENCES

1. *Pravila ulashtuvannya electroustanovok* [Electrical installation regulations]. Kharkiv, Fort Publ., 2017. 760 p. (Ukr).

2. Rozov V., Grinchenko V. Simulation and analysis of power frequency electromagnetic field in buildings closed to overhead lines. *2017 IEEE First Ukraine Conference on Electrical and Computer Engineering (UKRCON)*. Kyiv, Ukraine, pp. 500-503. **doi: 10.1109/UKRCON.2017.8100538**.

3. Rozov V.Yu., Grinchenko V.S., Yerisov A.V., Dobrodeyev P.N. Efficient shielding of three-phase cable line magnetic field by passive loop under limited thermal effect on power cables. *Electrical engineering & electromechanics*, 2019, no.6, pp. 50-54. **doi: 10.20998/2074-272X.2019.6.07.**

4. Active Magnetic Shielding (Field Cancellation). Available at: http://www.emfservices.com/afcs.html (accessed 10 September 2012).

5. Rozov V.Yu., Reutskyi S.Yu., Pelevin D.Ye., Pyliugina O.Yu. The magnetic field of transmission lines and the methods of its mitigation to a safe level. *Technical Electrodynamics*, 2013, no. 2, pp. 3-9. (Rus).

6. Rozov V.Yu., Reutskyi S.Yu. Pyliugina O.Yu. The method of calculation of the magnetic field of three-phase power lines. *Technical electrodynamics*, 2014, no.5, pp. 11-13. (Rus).

7. Salceanu A., Paulet M., Alistar B.D., Asiminicesei O. Upon the contribution of image currents on the magnetic fields generated by overhead power lines. *2019 International Conference on Electromechanical and Energy Systems (SIELMEN).* 2019. **doi: 10.1109/sielmen.2019.8905880.**

8. Bravo-Rodríguez J., Del-Pino-López J., Cruz-Romero P. A Survey on Optimization Techniques Applied to Magnetic Field Mitigation in Power Systems. *Energies*, 2019, vol.12, no.7, p. 1332. **doi: 10.3390/en12071332**.

9. Canova A., Giaccone L., Cirimele V. Active and passive shield for aerial power lines. *25th International Conference on Electricity Distribution Madrid*, 3-6 June 2019. Paper no. 1096, pp. 1-5.

10. Sushchenko O.A., Tunik A.A. Robust optimization of the inertially stabilized platforms. *2012 2nd International Conference «Methods and Systems of Navigation and Motion Control» (MSNMC)*, Kiev, 2012, pp. 101-105. **doi: 10.1109/msnmc.2012.6475102.**

11. Sushchenko O.A. Robust control of angular motion of platform with payload based on H∞-synthesis. *Journal of Automation and Information Sciences*, 2016, vol. 48, no. 12, pp. 13-26. **doi: 10.1615/jautomatinfscien.v48.i12.20**.

12. Sushchenko O.A. Robust control of platforms with instrumentation. *2019 IEEE 2nd Ukraine Conference on Electrical and Computer Engineering (UKRCON)*, Lviv, Ukraine, 2019, pp. 518-521. **doi: 10.1109/ukrcon.2019.8879969**.

13. Zhiteckii L.S., Azarskov V.N., Solovchuk K.Y., Sushchenko O.A. Discrete-time robust steady-state control of nonlinear multivariable systems: a unified approach. *IFAC Proceedings Volumes*, 2014, vol. 47, no. 3, pp. 8140-8145. **doi: 10.3182/20140824-6-za-1003.01985.**

14. Zhiteckii L.S., Solovchuk K.Y. Robust adaptive pseudoinverse model-based control of an uncertain SIMO memoryless system with bounded disturbances. *2019 IEEE 2nd Ukraine Conference on Electrical and Computer Engineering (UKRCON)*, Lviv, Ukraine, 2019, pp. 621-627. **doi: 10.1109/ukrcon.2019.8879824.**

15. Chorna O., Chornyi O., Tytiuk V. Identification of changes in the parameters of induction motors during monitoring by measuring the induction of a magnetic field on the stator surface. *2019 IEEE International Conference on Modern Electrical and Energy Systems (MEES)*. Kremenchuk, 2019. **doi: 10.1109/MEES.2019.8896554.**

16. Chystiakov P., Chornyi O., Zhautikov B., Sivyakova G. Remote control of electromechanical systems based on computer simulators. *2017 International Conference on Modern Electrical and Energy Systems (MEES)*. Nov. 2017. **doi: 10.1109/mees.2017.8248934.**

17. Shenkman A., Sonkin N., Kamensky V. Active protection from electromagnetic field hazards of a high voltage power line. *HAIT Journal of Science and Engineering. Series B: Applied Sciences and Engineering*, Vol. 2, Issues 1-2, pp. 254-265.

18. Korol S., Buryan S., Pushkar M., Ostroverkhov M. Investigation the maximal values of flux and stator current of autonomous induction generator. *2017 IEEE First Ukraine Conference on Electrical and Computer Engineering (UKRCON)*, May 2017. **doi: 10.1109/ukrcon.2017.8100302**.

19. Ostroverkhov M., Buryk M. Control of permanent magnet synchronous motor under conditions of parametric uncertainty. *2019 IEEE International Conference on Modern Electrical and Energy Systems (MEES)*, Sep. 2019. **doi: 10.1109/mees.2019.8896635.**

20. Ostroverkhov M., Pyzhov V., Korol S. Control of the electric drive under conditions of parametric uncertainty and coordinates' interrelation. *2017 International Conference on Modern Electrical and Energy Systems (MEES)*, Nov 2017. **doi: 10.1109/mees.2017.8248953.**

21. Panchenko V.V., Maslii A.S., Pomazan D.P., Buriakovskyi S.G. Determination of pulsation factors of the system of suppression of interfering harmonics of a semiconductor converter. *Electrical engineering & electromechanics*, 2018, no.4, pp. 24-28. **doi: 10.20998/2074-272X.2018.4.04.**

22. Buriakovskyi S.G., Maslii A.S., Panchenko V.V., Pomazan D.P., Denis I.V. The research of the operation modes of the diesel locomotive CHME3 on the imitation model. *Electrical engineering & electromechanics*, 2018, no.2, pp. 59-62. **doi: 10.20998/2074-272X.2018.2.10.**

23. Buriakovskyi S., Maslii A., Maslii A. Determining parameters of electric drive of a sleeper-type turnout based on electromagnet and linear inductor electric motor. *Eastern-European Journal of Enterprise Technologies*, 2016, vol.4, no.1(82), pp. 32-41. (Rus). **doi: 10.15587/1729-4061.2016.75860**.

24. Shchur I., Klymko V. Comparison of different types of electromechanical systems for creating of counter-rotating VAWT. *2017 IEEE First Ukraine Conf. on Electrical and Computer Engineering (UKRCON-2017)*, pp. 373-378. **doi: 10.1109/ukrcon.2017.8100513**.

25. Shchur I. Impact of nonsinusoidalness on efficiency of alternative electricity generation systems. *2010 International School on Nonsinusoidal Currents and Compensation*, Lagow, 2010, pp. 218-223. **doi: 10.1109/isncc.2010.5524483**.

26. Zagirnyak M., Bisikalo O., Chorna O., Chornyi O. A model of the assessment of an induction motor condition and operation life, based on the measurement of the external magnetic field. *2018 IEEE 3rd International Conference on Intelligent Energy and Power Systems (IEPS)*. 2018. pp. 316-321. **doi: 10.1109/ieps.2018.8559564.**

27. Zagirnyak M., Chornyi O., Nykyforov V., Sakun O., Panchenko K. Experimental research of electromechanical and biological systems compatibility. *Przegląd Elektrotechniczny*, 2016, vol.1, no.1, pp. 130-133. **doi: 10.15199/48.2016.01.31**.

28. Zagirnyak M., Serhiienko S., Chornyi O. Innovative technologies in laboratory workshop for students of technical specialties. *2017 IEEE First Ukraine Conference on Electrical and Computer Engineering (UKRCON)*, May 2017. **doi: 10.1109/ukrcon.2017.8100446**.

29. Ren Z., Pham M.-T., Koh C.S. Robust Global Optimization of Electromagnetic Devices With Uncertain Design Parameters: Comparison of the Worst Case Optimization Methods and Multiobjective Optimization Approach Using Gradient Index. *IEEE Transactions on Magnetics*, 2013, vol.49, no.2, pp. 851-859. **doi: 10.1109/tmag.2012.2212713**.

30. Galchenko V.Y., Yakimov A.N. A turmitobionic method for the solution of magnetic defectometry problems in structural-parametric optimization formulation. *Russian Journal of Nondestructive Testing*, 2014, vol.50, no.2, pp. 59-71. **doi: 10.1134/s106183091402003x.**

31. Gal'chenko V.Y., Yakimov A.N., Ostapushchenko D.L. Pareto-optimal parametric synthesis of axisymmetric magnetic systems with allowance for nonlinear properties of the ferromagnet. *Technical Physics*, 2012, vol.57, no.7, pp. 893-899. **doi: 10.1134/s1063784212070110**.

32. Ummels M. *Stochastic Multiplayer Games Theory and Algorithms*. Amsterdam University Press, 2010. 174 p.

Received 25.05.2020

B.I. Kuznetsov[1], *Doctor of Technical Science, Professor,*
T.B. Nikitina[2], *Doctor of Technical Science, Professor,*
I.V. Bovdui[1], *Candidate of Technical Science,*
[1] State Institution «Institute of Technical Problems of Magnetism of the NAS of Ukraine»,
19, Industrialna Str., Kharkiv, 61106, Ukraine,
phone +380 50 5766900,
e-mail: kuznetsov.boris.i@gmail.com
[2] Kharkov National Automobile and Highway University,
25, Yaroslava Mudroho Str., Kharkov, 61002, Ukraine,
e-mail: tatjana55555@gmail.com

How to cite this article:
Kuznetsov B.I., Nikitina T.B., Bovdui I.V. Simplified mathematical model of group of overhead power lines magnetic field. *Electrical engineering & electromechanics*, 2020, no. 4, pp. 24-29. **doi: 10.20998/2074-272X.2020.4.04.**

UDC 681.513, 621.365, 62-83-52 **doi: 10.20998/2074-272X.2020.4.05**

Y.S. Paranchuk, R.Y. Paranchuk

RESEARCH OF ARC FURNACE ELECTRICAL MODE WITH A FUZZY CONTROL MODEL

Goal. The purpose of the paper is to increase the efficiency of arc steelmaking furnace (ASF) operating modes control basing on the improvement of arc lengths control model. Method. The control model is based on the fuzzy set theory, and the structural modelling methodology is used to study the dynamics indices. Results. The structural scheme of a furnace arc lengths fuzzy control system and the electrical mode (EM) coordinate control dynamics parameters values in response to the deterministic and random arc lengths fluctuations were obtained. Scientific novelty. For the first time, a fuzzy model of an EM mismatch signal generation with operational adaptation to its current state in each phase was developed, which enabled by-phase independent control of arc lengths and improved energy efficiency. Practical value. Dynamic accuracy of EM coordinates stabilization at the setpoint level is improved, in particular the arc currents dispersion is reduced, which leads to a corresponding power loss decrease in arc furnace short network, an increase of the furnace productivity, as well as to an improvement of the electromagnetic compatibility of the arc furnace and power supply network. References 17, figures 7.
Key words: **arc steelmaking furnace, electric mode, fuzzy control, autonomy, dispersion.**

Запропоновано нечіткий закон керування електричним режимом (ЕР) дугової сталеплавильної печі (ДСП). Створено структурну Simulink-модель системи керування ЕР на основі нечіткого закону. Проведено комп'ютерні дослідження динаміки регулювання координат ЕР дугової печі ДСП-200 з використанням диференційного та нечіткого законів керування. Результати досліджень показали, що при використанні нечіткого закону зменшуються дисперсія струмів дуг і питомі витрати електроенергії та зростає продуктивність дугової печі. Бібл. 17, рис.7.
Ключові слова: **дугова сталеплавильна піч, електричний режим, нечітке регулювання, автономність, дисперсія.**

Предложен нечеткий закон управления электрическим режимом (ЭР) дуговой сталеплавильной печи (ДСП). Разработано структурную Simulink-модель системы управления ЭР на основе нечеткого закона. Проведены компьютерные исследования динамики регулирования координат ЭР дуговой печи ДСП-200 с использованием дифференциального и нечеткого законов управления. Результаты исследований показали, что при использовании нечеткого закона уменьшаются дисперсия токов дуг удельный расход электроэнергии и увеличивается производительность дуговой печи. Библ. 17 рис.7.
Ключевые слова: **дуговая сталеплавильная печь, электрический режим, нечеткое регулирование, автономность, дисперсия.**

Introduction. Technological processes of the electrometallurgical industry are characterized by the consumption of significant amounts of electricity. Its main electrotechnological units are arc steelmaking furnaces (ASFs), in which high-alloy steels and precision alloys are smelted mainly from scrap metal.

The electrical mode (EM) of the ASF is formed by a set of coordinates such as voltage, current and power of the system of three-phase arcs, and is characterized by transient random and phase-asymmetric nature of the change. The main reason for such a complex nature of the change of EM coordinates is the continuous during melting action of intense random parametric perturbations in the power supply circuit of three-phase arcs without zero conductor and fluctuations of arc lengths, the statistical characteristics of which change during melting in a wide range as well as the imperfection of automatic control systems (ACS).

One of the subsystems in the hierarchical structure of modern ACS of the EM of arc furnaces is a subsystem for adjusting the position of the electrodes. Its main task is the qualitative stabilization of the EM coordinates at the level of the set optimal values, which are operatively formed at the highest level of the hierarchy of the ACS of the EM, and the integral assessment of the quality of their operation is the variance of the EM coordinates and first of all arc currents [1-3].

Scientific problem definition and substantiation of its urgency. Qualitative stabilization of EM coordinates by a lower-level subsystem makes it possible to improve indices of energy efficiency and electromagnetic compatibility and, in addition, further enhances the effectiveness of the implementation of optimal control strategies. Therefore, the task of developing solutions to improve the quality of stabilization of EM coordinates of the ASF at the level of setpoints, and especially for powerful and superpowerful furnaces, is important and relevant, as it will comprehensively improve energy efficiency and electromagnetic compatibility of ASFs and power supply networks.

Review of literature sources. Most modern systems of automatic control (SAC) of the position of the electrodes of the ASF are electromechanical or electrohydraulic regulators of arc power, such as АРДМ-Т or АРДГ, respectively [1-5].

These SAC positions of the electrodes use mainly four models of control signal generation for electrode movement: differential and impedance models and control models by the deviation of voltage and arc current from the specified values [4, 5]. Under the control model (law) we understand the mathematical model of the formation of the EM mismatch signal, which the SAC transforms into the corresponding movements of the electrodes. Each of these models has certain advantages and disadvantages in the regulation of perturbations in different states of the EM.

© Y.S. Paranchuk, R.Y. Paranchuk

The results of the study of dynamics indicators using different laws in the double-circuit structure of the ACS of the electric mode of the ASF are presented in [6, 7]. In such a structure, the laws of control of the EM are particularly pronounced. From the results obtained in [6, 7] it follows that the control laws significantly affect the indices of dynamics, energy efficiency and electromagnetic compatibility in both single- and double-circuit structures of ASF EM ACS. They show that the optimization parameters of the mismatch signal generation models are the dependence of the mismatch signal formation $U_r(U_a, I_a)$ and its coefficients, as well as the dependence of the artificial external characteristic I $I_a(U_a)$ of the double-circuit ASF EM ACS.

Most of the existing arc power regulators in single-circuit ACS operate on a differential model of EM mismatch signal formation [4, 5]:

$$U_r(U_a, I_a) = a \cdot U_a - b \cdot I_a, \qquad (1)$$

where a, b are the constant coefficients that set the constant values of arc voltage, current and power; U_a, I_a are the current values of arc voltage and current; U_r is the signal of the mismatch of the electric mode.

Using model (1), reliable arc ignition is performed in the modes of arc breaks (ABs) and short circuits (SCs), i.e. adequate implementation of extreme perturbations of the EM and close to them is performed. But under the action of small and medium deviations of arc lengths, the mismatch signal according to this model does not always adequately correspond to the real arc length – the state of the EM in this phase. The reason for this is the use of arc current in the model of differential law (1), because the phase current under the current three-phase power supply of three-phase arcs without neutral conductor is determined not only by the arc length (voltage) of this phase, but depends on arc lengths.

This shortcoming is emphasized in [8, 9]. These works indicate that the use of arc currents in electrode motion control models leads to a violation of the autonomy of the phase channels of regulating the lengths (voltages, currents, powers) of arcs.

Known regulation of the EM by the deviation of the arc voltage from the specified value (voltage model)

$$U_{r.1}(U_a) = k \cdot (U_a - U_{a.set}), \qquad (2)$$

where $U_{r.1}(U_a)$ is the dependence of the EM mismatch signal; k is the gain of the regulator; $U_{a.set}$ is the setting of the regulator by arc voltage [4, 5].

According to this law, perfect regulation is obtained in the modes of small and medium deviations of arc lengths, but in extreme perturbations of the EM due to the displacement of the zero point of the arc voltage vector, the dynamics of electrode motion in arc ignition modes deteriorates.

Some EM regulators from Siemens and Danieli use variants of the impedance control law, according to which the arc lengths are adjusted at deviating the full phase impedance from the set value (adaptive impedance regulator) [10-12]. However, when calculating the phase impedances, phase currents are also used, which, for the reasons indicated above, does not make it possible to fully obtain the phase-by-phase autonomy of the arc length regulation process.

In [12, 13], an improved hydraulic drive of the mechanism of movement of the electrodes (MME) with a servovalve with a nonlinear control characteristic and an adaptive nonlinear model of phase impedance stabilization is considered. In [8, 11, 14] the regulation according to the nonlinear model of the admittance is considered. These papers emphasize that such models are easier to set up and have improved dynamic characteristics compared to other EM regulators. But these models in the vicinity of the point of a given EM are sensitive to the action of perturbations of other phases, which a priori negatively affects the dynamic accuracy of stabilization of the coordinates of the EM.

The analysis of other modern technical solutions for EM SAC shows that the improvement of the model of mismatch signal U_r formation in the function of which the signals U_c^{la} of electrode motion control are formed, is an effective factor and an important and urgent task in improving ASF energy efficiency indices.

The goal of this work is to increase the efficiency of control of the operation modes of the arc steelmaking furnace on the basis of improving the model of regulation of arc lengths.

Substantiation of the research direction. The process of EM control and control of ASF coordinates in the conditions of transient random perturbations actions takes place in the conditions of incomplete information about change of parameters of elements and coordinates of electric circuit of three-phase arcs of the ASF, because it is impossible to realize exact operative on-line operational control. Therefore, given the complexity of processes in the power circuit and their mathematical description, the presence of uncertainties in control, it is appropriate for control tasks for ASF EM to use intelligent methods, including the use of fuzzy control models, because indicated features and nature of processes in the ASF correspond to the peculiarities of application and functioning of fuzzy control models [15].

The main results of the investigations. From the above it follows that the main attention of the study should be paid to improving the systems of SAC of arc lengths.

Figure 1 shows a block diagram of an electromechanical power regulator of arc powers type АРДМ-Т, on the basis of which the proposed system of fuzzy adaptive control of the lengths of the arcs of the ASF is based.

The three-phase system of arcs of a ASF (AF) is fed from a secondary winding of the furnace transformer FT with phase voltage U_{2pf}. The electric mode in the given SAC of the АТДМ-Т regulator is regulated by the differential law, and the mismatch signal $U_r(U_a, I_a)$ of the EM is formed in the BC comparison block according to model (1). The current values of the arc voltage U_a and the arc current I_a are generated at the outputs of the sensors of arc voltage VS and arc current CS, respectively. At the output of the CSFB control signal generating block as a function of the mismatch signal U_r, taking into account the insensitivity zone, SAC gain for raising and lowering the electrodes, restrictions on the maximum speed of raising and lowering the electrodes,

the electrode movement control signal U_c^{la} is formed. The electric drive of the EM, which in the АРДМ-Т-12 controller is represented by a reversible system «thyristor converter – DC motor» (ED TC-M), and the mechanism of movement of the electrode (MME) type «gear-rail» transform the control signal U_c^{la} into the corresponding movements of the electrode $\pm\Delta l_a$ in the direction of elimination of disturbances.

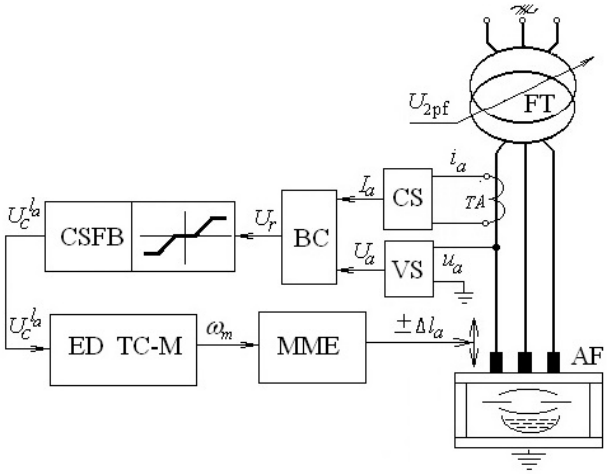

Fig. 1. Functional block diagram of the SAC of arc lengths of the ASF

Figure 2 shows the natural external characteristic $I_a(U_a)$ and the dependence of the arc power $P_a(U_a)$ of the arc steelmaking furnace ДСП-200. This figure also shows the points of the steady state mode of the furnace $A(U_{a.set}, I_{a.set})$ and of the set power of the arcs $B(U_{a.set}, P_{a.set})$, where $U_{a.set}$ = 198.3 V; $I_{a.set}$ = 43.97 A; $P_{a.set}$ = 8.72 MW are the settings for arc voltage, current and power, respectively.

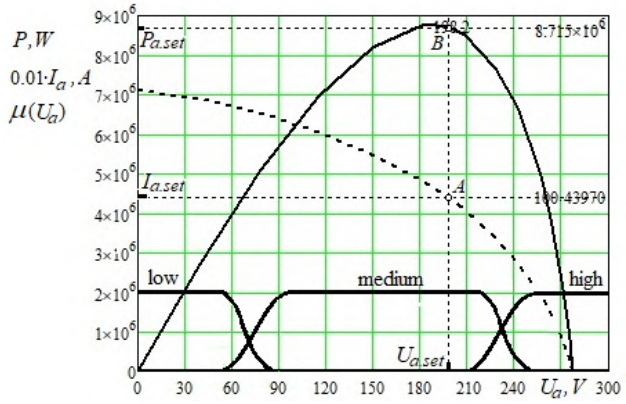

Fig. 2. External characteristic $I_a(U_a)$ and power characteristic $P_a(U_a)$ of arcs of the arc furnace ДСП-200 and membership function $\mu(U_a)$ of the linguistic variable «arc voltage»

The main task of ASF EM SAC is to reduce the dispersion of EM coordinates during melting, i.e. to maximize the operating time of the furnace in the modes around the operating point *A* of the furnace, then the values of all energy efficiency indices will approach the maximum, and the variance of EM coordinates is minimized.

To do this, instead of model (1), in the BC comparison block it is proposed to use a control model adaptive to the change of EM states, which combines a model of a modified differential law based on the principles of fuzzy logic

$$U_{r.2}(U_a, I_a) = a \cdot U_a - b \cdot (I_a - I_{a.set}) \qquad (3)$$

and the voltage law (2).

With such a solution in the on-line mode active in each phase, the law of control $U_r(U_a, I_a)$ is established which corresponds to the current state of the EM in this phase. EM states in phases are identified by the phase arc voltage, because the voltage at the arc column unambiguously and linearly depends on its length $U_a=\alpha + \beta \cdot l_a$, where α, β are the anode-cathode voltage drops at the arc column; l_a is the length of the arc. Operational control of the arc voltage U_a is proposed to be performed by a device that operates on the basis of neural network identification technologies [16]. The above correspondence of voltages on arcs to states of EM (lengths of arcs) is described by shown in Fig. 3 membership functions $\mu(U_a)$. It is proposed to change the control laws (calculation models $U_r(U_a, I_a)$) in phases according to the fuzzy Takagi-Sugeno model.

During the control process, three EM states are identified: the mode of operational short circuit and close to it (these are short arcs), rational modes (medium arcs) as modes around the operating point of furnace *A*, and the mode of arc break and close to it (long arcs) .

The range of low voltages (these are short arcs) in the model of the fuzzy output system Takagi-Sugeno is described by the term *low* (this is the state of short circuit or close modes), medium – *medium*, and long – *high* (these are states of AB or close) to him) (Fig. 2). The terms of the linguistically variable U_a are presented by membership functions of type *gauss2mf*.

In the states of the EM in the vicinity of the operating point *A*, the mismatch signal is calculated according to the voltage law (2), because it allows to implement autonomous (phase-independent) regulation of arc lengths. This increases the dynamic accuracy of the stabilization of the EM coordinates at the level of the settings.

In the states of the EM arising under the influence of extreme perturbations – SC, AB or close to them, active for the formation of the mismatch signal $U_r(U_a, I_a)$ an improved differential law (3) is established, which, in contrast to the voltage one (2), better implements arc ignition processes.

Figure 3 shows the developed block diagram of the BC comparison block (Fig. 1), which implements in each phase of regulation a fuzzy adaptive to the state of the EM model the formation of the mismatch signal

$$\begin{aligned} U_r(U_a, I_a) &= (1 - k(U_a)) \cdot U_{r.1}(U_a) + \\ &+ k(U_a) \cdot U_{r.2}(U_a, I_a). \end{aligned} \qquad (4)$$

The presented block diagram illustrates the implementation of the proposed fuzzy adaptive to the states of the EM model (4) for calculating the mismatch signal $U_r(U_a, I_a)$ of the EM. As a function of this signal in the CSFB block (Fig. 1) the electrode motion control signal U_c^{la} is formed.

Fuzzy adaptation of the control process is realized by the fuzzy inference system FIS, which operates on the basis of the Takagi-Sugeno model (Fig. 3).

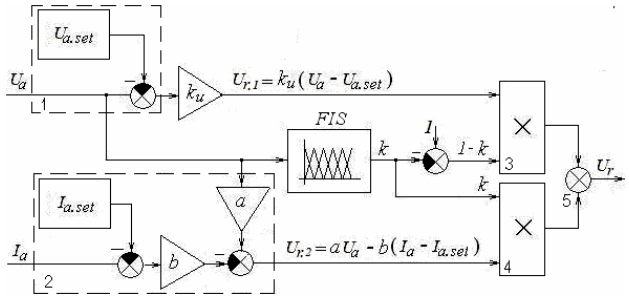

Fig. 3. Block diagram of the BC with adaptive to changing the states of the EM fuzzy model of the formation of the mismatch signal

The input linguistic variable for FIS is the current value of the arc voltage U_a. For its operative processing in the FIS block the following base of rules of fuzzy products is implemented:

1. *if* $U_a \in low$ then $k = 1$ [1] ;
2. *if* $U_a \in medium$ then $k = 0$ [1] ; (5)
3. *if* $U_a \in high$ then $k = 1$ [1] .

The above algorithmic and parametric degrees of freedom of the FIS fuzzy inference system correspond to shown in Fig. 4 dependence $k(U_a)$.

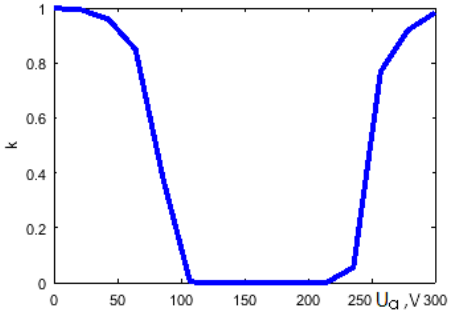

Fig. 4. Dependence $k(U_a)$ of fuzzy inference system FIS

In the process of implementation of EM disturbances in block 1 (Fig. 3), a mismatch signal is continuously formed according to the voltage deviation law $U_{r.1}(U_a)$ (2) and according to the modified differential law $U_{r.2}(U_a, I_a)$ (3) in block 2. These mismatch signals in blocks 3 and 4 are multiplied by 1–k and k, respectively, and then in the adder 5 in accordance with model (4) $U_r(U_a, I_a)$ is calculated. From the proposed fuzzy control model (4) it follows that at point A of the given mode the mismatch signal $U_r(U_{a.set}, I_{a.set}) = 0$.

In the modes of action of extreme perturbations, the control of electrode motion is performed according to the differential law ($k \cong 1$), according to which the control of electrode movements effective for reliable ignition of arcs is realized.

In the modes close to the given ЕЬ ($k \cong 0$) – around the point $A(U_{a.set}, I_{a.set})$ the control of the motion of the electrodes is realized according to the law of deviation of the arc voltage (2). This results in autonomous phase-by-phase control of the electrode movement.

The study of the efficiency of the developed fuzzy adaptive to EM states model of arc length control is performed on the three-phase in the instantaneous coordinates the Simulink model of SAC of the position of the electrodes of the arc furnace ДСП-200 [6, 17]. This model is accepted as the basic one. It studied the dynamics of EM SAC with power regulator АРДМ-Т-12 used on this furnace. Subsequently, in the comparison block of this Simulink model the fuzzy law (4) of formation of the mismatch signal is realized (Fig. 3). On such Simulink model the dynamics of regulation of coordinates of EM is investigated with use of the proposed fuzzy model of regulation of lengths of arcs.

For adequate reproduction in Simulink models of states and dynamics of regulation of EM coordinates in different technological stages of melting, they provide the possibility of realization of models of dynamic volt-ampere characteristics (DVAC) of arcs $u_a(i_a)$ and models of generating random processes of disturbances $f_{la}(t)$ by the lengths of the arcs.

For this purpose in Simulink models the possibility of realization of three models of DVAC is provided: linear $u_a(t) = R_a(t) \cdot i_a(t)$, nonlinear based on the arctangent function

$$u_a(t) = 2 \cdot E_{am} \cdot \arctan(k \cdot i_a(t))/\pi ,$$

and nonlinear based on the Cassie differential equation

$$\theta_a \cdot \frac{dg_a(t)}{dt} = \left(\frac{u_a(t)}{E_{am}} \right)^2 \cdot g_a(t),$$

where $g_a(t)$, $R_a(t)$ are the instantaneous arc conductivity and resistance; E_{am} is the counter-EMF of the arc; $u_a(t)$, $i_a(t)$ are the instantaneous arc voltage and current, θ_a is the arc time constant, which characterizes its thermal inertia.

In Simulink models of EM SAC 3 generators of independent random processes with variable parameters of their stochastic characteristics are realized. In the process of computer research, random processes are generated that differed in frequency spectrum and amplitude characteristics, and which correspond to the processes of perturbations acting at the technological stages of melting wells in the charge, collapse of the charge and oxidation of the melt in the arc furnace ДСП-200.

Computer studies of the dynamics of arc length control are performed when implementing in the Simulink model of EM SAC of the differential law (1) of the mismatch signal formation used in the regulator АРДМ-Т-12 arc furnace ДСП-200, and using the proposed fuzzy law $U_r(U_a, I_a)$ (4). In order to correctly compare the dynamics of both laws, the studies are performed under the action of the same realizations of deterministic and random perturbations that correspond to the studied stage of melting.

Based on the results of comparative analysis of the dynamics indices of regulation of EM coordinates using both laws of regulation of arc lengths, conclusions are drawn about the effectiveness of the proposed fuzzy model (4) in comparison with the differential one (1).

Figure 5 shows the time dependencies of the voltages and currents of the arcs of the furnace ДСП-200

obtained on Simulink models during the implementation of the sequence of deterministic perturbations, namely, the symmetric three-phase operational short circuit $t \in$ 0.5-1.75 s; single-phase short circuit in phase C $t \in$ 1.75-2.8 s and close to the arc break in phases A and B $t \in$ 2.8-4 s, by differential (1) and fuzzy (4) control models.

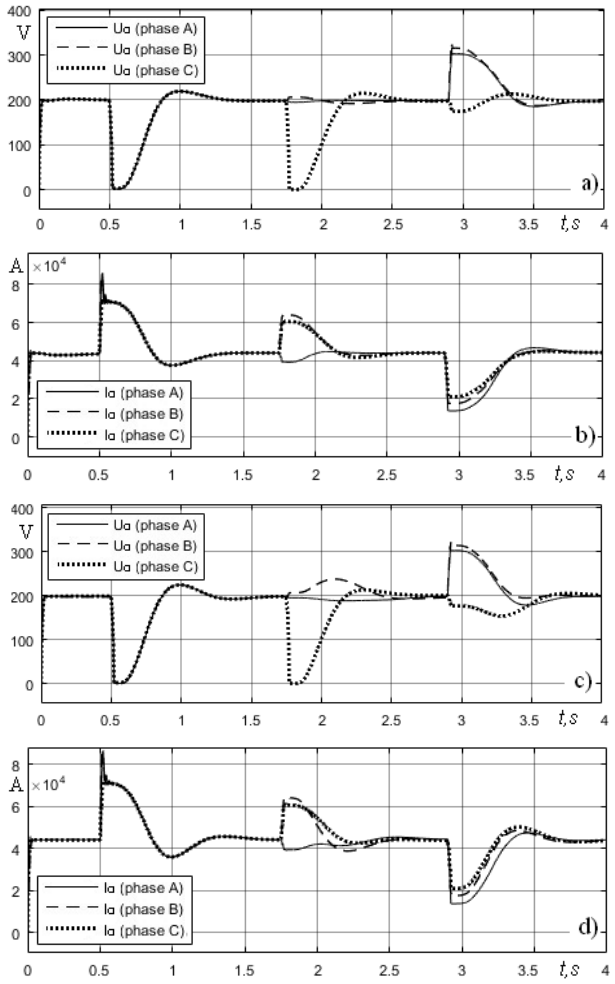

Fig. 5. Time dependencies of voltages and currents of arcs of furnace ДСП-200 in the regulation of deterministic perturbations: *a*, *b* – fuzzy model (4), *c*, *d* – differential model (1)

Three-phase symmetrical operational SC is implemented by both models $U_r(U_a, I_a)$ equally, because in this mode there are no interactions of phase loads. Analysis of the obtained processes $U_{aj}(t)$ ($j = A,B,C$) at implementation of asymmetric deterministic perturbations shows that in fuzzy model (4) the arc length is regulated only in those phases where arc length deviations have occurred. The movements of the electrodes in the phases where there is no perturbation are minimal. They occur only in the first moments of extreme perturbations, when the differential law (1) is used to ignite the arcs. In the differential model (1) of regulation (АРДМ-Т-12 regulator) the movements of the electrodes in certain states of the EM are wrong, they do not always correspond to the phase states of the EM.

These conclusions are also confirmed by the analysis of time dependencies of phase signals of mismatch $U_{rj}(t)$ and speeds $\omega_j(t)$ of motors of movement of electrodes at implementation of the same determined perturbations which are shown in Fig. 6.

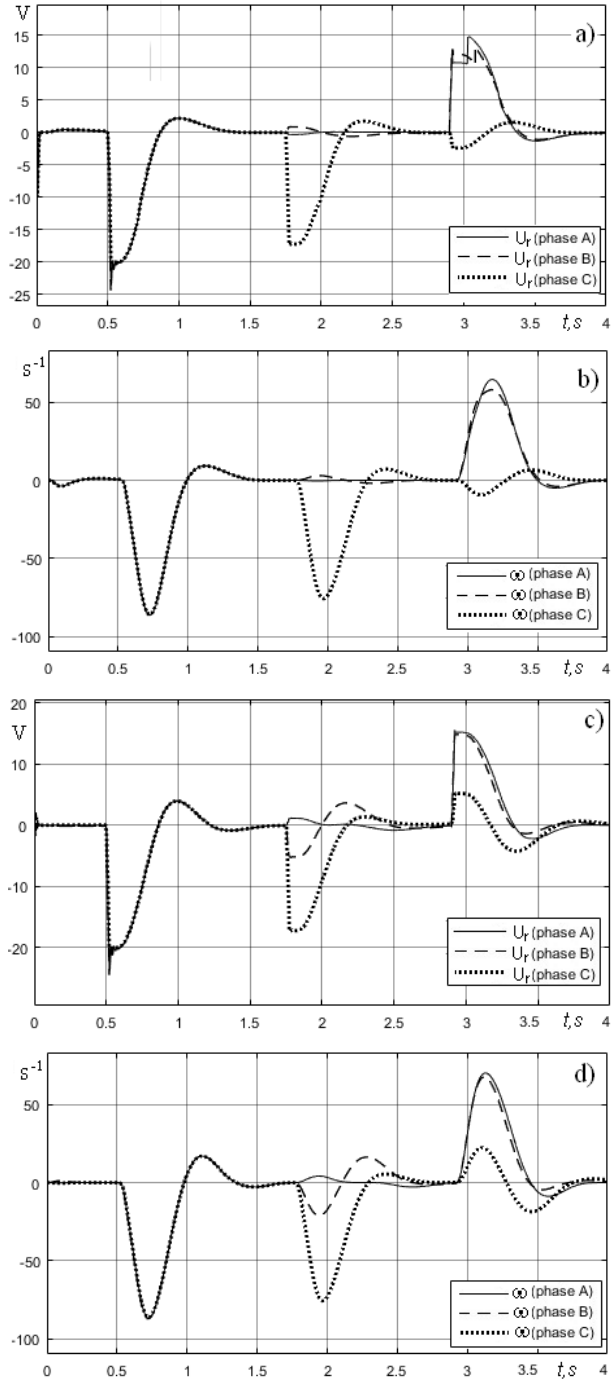

Fig. 6. Time dependencies of mismatch signals $U_{rj}(t)$ and speeds $\omega_j(t)$ of MME motors of electrodes with fuzzy (4) (*a*, *b*) and differential (1) (*c*, *d*) models of arc length control

Shown in Fig. 5, 6 dynamic processes of regulation of deterministic perturbations in such a «pure» form in the melting interval are rare. Therefore, their research and analysis are conducted only as testing to confirm the correct operation of the designed system of fuzzy derivation of FIS in the structure of the EM SAC. For completeness of their analysis, we note that the regulation time of the investigated deterministic perturbations when using the fuzzy model (4) of the BC comparison block is

10-20 % less than using the differential one (1). The phase-average integral quadratic estimation of the quality $I_{sq} = \int_0^4 (\bar{I}_a - I_a(t))^2 dt$ of regulation of these perturbations in the interval $t \in [0, 4]$ s improved by 8.6 %. The value of this estimate is proportional to the reduction of power losses in a short network of the ASF.

The obtained values show the increase of the control speed, the improvement of the dynamic accuracy of the stabilization of the EM coordinates and the improvement of the energy efficiency of the ASF in the regulation of deterministic perturbations by the fuzzy model (4) of the BP.

However, it is possible to obtain an integrated estimation of the efficiency of the proposed fuzzy model of arc length regulation only on the examples of phase-asymmetric random perturbations regulation by arc lengths, which are the main perturbations in the melting process in the ASF.

For this purpose, computer simulations of the modes of control of random perturbations at stationary intervals T_c = 180-240 s and their changes for different technological stages of melting using both control models are performed. Figure 7 shows obtained on Simulink models the fragments $t \in$ 0-30 s of these processes of regulation of EM coordinates using the developed fuzzy model (4) (Fig. 7,*b*, Fig. 7,*c*) and according to the differential law (1) (АРДМ-Т-12 regulator) (Fig. 7,*d*, Fig. 7,*e*) of the ДСП-200 furnace. The perturbation processes $f_{aj}(t)$ (Fig. 7,*a*) corresponded to the stage of charge collapse.

This figure shows the processes of change of voltages $U_{aA}(t)$ and currents $I_{aA}(t)$ of phase A arcs. Analysis of the processes $I_{a,j}(t)$ obtained in these computer experiments shows that the dispersion of arc currents using a fuzzy (4) control model amounted to: D_{I_A} = 168.3 kA^2; D_{I_B} = 159.3 kA^2, D_{I_C} = 181.2 KA^2, and by the differential model D_{I_A} = 236.3 kA^2; D_{I_B} = 235.1 kA^2, D_{I_C} = 219.9 kA^2. The average phase dispersion of arc currents for these control models is: $D_{I.fuz}$ = 169.6 kA^2, $D_{I..dif}$ = 203.3 kA^2, respectively, and the average phase reduction of the dispersion of arc currents ΔD_I = 33.7 kA^2 or 4.5 % of the maximum possible dispersion of arc currents.

Studies of the dynamics of arc current regulation at other technological stages of melting, i.e. under the action of random perturbations with other amplitude and frequency characteristics, show that the dispersion of arc currents using the proposed fuzzy control model decreased by 3-7.5 %.

According to the known results of researches, at the obtained estimation of decrease in dispersion of currents of arcs by 3-7.5 %, arc furnace productivity increases by 4-5 %, and specific electricity consumption decreases by 3-4 %. For the superpowerful ДСП-200 furnace it gives essential improvement of indicators of electrotechnological efficiency.

In the future it is planned to investigate the influence on the dynamics indices of other algorithmic and parametric degrees of freedom of the FIS fuzzy derivation system model on the dynamics of EM coordinate control and on the energy efficiency indices of the arc furnace.

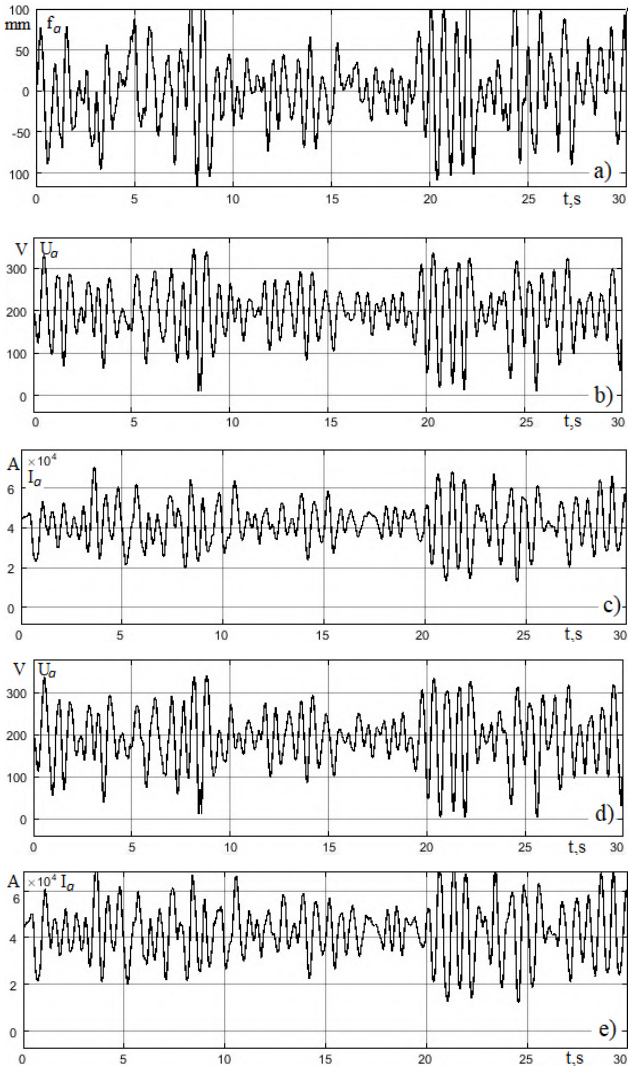

Fig. 7. Time dependencies of perturbations $f_{a,A}(t)$ (*a*), voltages $U_{a,A}(t)$, $I_{a,A}(t)$ of arcs when using fuzzy (4) (*b*, *c*) and differential (1) (*d*, *e*) models of arc length adjustment

Conclusions.

1. The proposed fuzzy model of EM mismatch signal generation with operative adaptation to its current state in each phase in comparison with known control models allows to implement phase-by-phase autonomous regulation of arc lengths and increase control efficiency of the ASF operation modes.

2. The possibility of realization of phase-by-phase autonomous implementation of deterministic and random EM perturbations in the range of average arc lengths using the proposed fuzzy model is confirmed, which allows to reduce in average by phases at different melting stages to decrease the dispersion of the ASF arc currents by 3-7.5 % and on this basis to increase the productivity of the ASF by 4-5 %, as well as to reduce the specific consumption of electricity by 3-4 %.

REFERENCES

1. Kazakov S.V., Garten, V. The 8th international Conference on Electrometallurgy of Steel (part I). *Electrometallurgy*, 2005, no. 12, pp. 36-43. (Rus).

2. Kudrin B.I. Retrospective and perspective views on electrical consumption in electrometallurgy. *Electrometallurgy*, 2003, no. 10, pp. 2-13. (Rus).
3. Lopukhov G.A. The state and tendencies of development of electro-smelting production (based on materials 33 of the IISI Conference). *Electrometallurgy*, 2000, no. 7, pp. 35-37. (Rus).
4. Maslov D.V. *Razrabotka algoritmov i sistem upravleniia dugovymi staleplavil'nymi pechami, snizhaiushchikh polomki elektrodov. Avtoref. diss. kand. tehn. nauk* [Development of algorithms and control systems for arc steelmaking furnaces that reduce electrode breakage. Abstracts of cand. techn. sci. diss.]. Moscow, 2014. (Rus).
5. Lyuta A.V. *Udoskonalena systema upravlinnia pryvodom peremishchennia elektrodiv duhovykh staleplavylnykh pechei Avtoref. diss. kand. tehn. nauk* [Improved control system for moving water of electrodes of arc steelmaking furnaces. Abstracts of cand. techn. sci. diss.]. Donetsk, 2013. (Ukr).
6. Lozynskyi O., Paranchuk Y., Stakhiv P. The study of dynamics of the two-loop arc furnace electric mode ACS on a Simulink-model. *Przeglad Elektrotechniczny*, 2018, no. 12, pp. 24-27. **doi: 10.15199/48.2018.12.06.**
7. Lozinskii, O.Y., Paranchuk, Y.S. System for the optimum control of the electrical conditions of an arc furnace powered through a controlled reactor. *Russian Metallurgy (Metally)*, 2007, no. 8, pp. 737-743. **doi: 10.1134/S0036029507080204**.
8. Nikolaev A.A., Kornilov G.P., Anufriev A.V., Pekhterev S.V., Povelitsa E.V. Electrical optimization of superpowerful arc furnaces. *Steel in Translation*, 2014, vol. 44, no. 4, pp. 289-297. **doi: 10.3103/S0967091214040135.**
9. Mees H., Hohl J., Krüger K. Dynamic Condition-Based Scrap Melt Control: Results of the Application at Thyssenkrupp Nirosta in Bochum. *10th European Electric Steelmaking Conference*, Graz, 25-28 September, 2012.
10. Nikolaev A.A., Tulupov P.G. Development of the improved control algorithms for ultra-high power electric arc furnace EAF-250 electrode motion system. *Electrotechnical Systems and Complexes*, 2015, no. 3 (28), pp. 20-27. (Rus).
11. Nikolaev A.A., Kornilov G.P., Povelitsa E.V., Tulupov P.G. Study of different methods to design automated electrode position control systems for electric arc furnaces and ladle furnaces. *Vestnik of Nosov Magnitogorsk State Technical University*, 2015, no. 2, pp. 90-100. (Rus).
12. Nikolaev A.A., Tulupov P.G. Method of setting optimum asymmetric mode of operation of electric arc furnace. *2016 11th France-Japan & 9th Europe-Asia Congress on Mechatronics (MECATRONICS) /17th International Conference on Research and Education in Mechatronics (REM)*, Jun. 2016. **doi: 10.1109/mecatronics.2016.7547111.**.
13. Nikolaev A.A., Tulupov P.G., Savinov D.A. Mathematical model of electrode positioning hydraulic drive of electric arc steel-making furnace taking into account stochastic disturbances of arcs. *2017 International Conference on Industrial Engineering, Applications and Manufacturing (ICIEAM)*, May 2017. **doi: 10.1109/ICIEAM.2017.8076205.**
14. Nikolaev A., Povelitsa E., Kornilov G., Anufriev A. Research and development of automatic control system for electric arc furnace electrode positioning. *Applied Mechanics and Materials*, 2015, vol. 785, pp. 707-713. **doi: 10.4028/www.scientific.net/amm.785.707**.
15. Lozynskyy O., Paranchuk Y., Paranchuk R. Fuzzy control law of electrode travel in arc steelmaking furnace. *16th International Conference on Computational Problems of Electrical Engineering (CPEE)*, Sep. 2015. **doi: 10.1109/cpee.2015.7333349.**
16. Paranchuk Ya.S., Paranchuk R.Ya. Neural network system for continuous voltage monitoring in electric arc furnace. *Naukovyi Visnyk Natsionalnoho Hirnychoho Universytetu*, 2016, no. 2 (152), pp. 74-80.
17. Lozynskyy O., Paranchuk Y., Kobylianskyi O. Simulink model of electric modes in electric arc furnace. *2017 IEEE International Young Scientists Forum on Applied Physics and Engineering (YSF)*, Oct. 2017. pp. 54-57. **doi: 10.1109/YSF.2017.8126591.**

Received 25.02.2020

Y.S. Paranchuk[1], *Doctor of Technical Science, Professor,*
R.Y. Paranchuk[1], *Candidate of Technical Science,*
[1] Lviv Polytechnic National University,
12, S. Bandera Str., Lviv, 79013, Ukraine,
e-mail: yparanchuk@yahoo.com

How to cite this article:
Paranchuk Y.S., Paranchuk R.Y. Research of arc furnace electrical mode with a fuzzy control model. *Electrical engineering & electromechanics*, 2020, no. 4, pp. 30-36. **doi: 10.20998/2074-272X.2020.4.05.**

UDC 621.3.022: 621.319.53: 621.373: 629.7 **doi: 10.20998/2074-272X.2020.4.06**

M.I. Baranov, S.G. Buriakovskyi, V.V. Kniaziev, S.S. Rudenko

ANALYSIS OF CHARACTERISTICS AND POSSIBILITIES OF HIGH-VOLTAGE ELECTRICAL ENGINEERING COMPLEX SCIENTIFIC-&-RESEARCH PLANNING-&-DESIGN INSTITUTE «MOLNIYA» OF NTU «KHPI» FOR THE TESTS OF OBJECTS OF ENERGY, ARMAMENT, AVIATION AND SPACE-ROCKET TECHNIQUE ON ELECTRIC SAFETY AND ELECTROMAGNETIC COMPATIBILITY

Purpose. *Implementation of analysis of basic technical descriptions and new possibilities of separate electric options of unique high-voltage electrical engineering complex Scientific-&-Research Planning-&-Design Institute «Molniya» of NTU «KhPI», intended for testing objects of industrial energy (IE) on electric safety, action on them of standard storm and interconnect pulses of voltage (current), and also objects of armament and military technique (OAMT), aviation (AT) and space-rocket (SRT) technique on electromagnetic compatibility (EMC) and resistibility at direct action on them of the rationed pulses of current of artificial lightning and row of no-spread temporal functions of pulses of current (high-voltage).* ***Methodology.*** *Basis of the applied electrical engineering, electroenergy and electromechanics, electrophysics bases of technique of high-voltage and large pulse currents, bases of the applied instrument-making, high-voltage measuring technique and standardization.* ***Results.*** *Description of basic technical descriptions and new possibilities of component parts of unique high-voltage electrical engineering complex Scientific-&-Research Planning-&-Design Institute «Molniya» of NTU «KhPI», intended for testing different objects of IE on electric safety, their resistibility to direct (indirect) action of standard aperiodic storm and interconnect pulses of voltage (current), and also OAMT, AT and SRT on EMC and resistibility to lightning at a direct action on them of the rationed pulses of current of artificial lightning. It is shown that these tests can be conducted in accordance with the requirements of normative documents of the USA of SAE ARP 5412: 2013, SAE ARP 5414: 2013, SAE ARP 5416: 2013, RTCA DO-160G: 2011, military Standards of the USA of MIL-STD-464C: 2010, MIL-STD-461G: 2015, Standards of NATO AECTP-500: 2016, AECTP-250: 2014, International Standards of IEC 62305-1: 2010, IEC 61024-1: 1990 and intergovernmental Standard GOST 1516.2-97 on the domestic high-voltage options of type of UITOM-1, GTM-10/350, GKIN-2, TI-CS115 (NCS08), TI-CS116 (NCS09), G-NCS10, MV 1000 and IK-1U with the rationed descriptions. Examples and results of tests of row of technical objects are resulted on indicated high-voltage little- and heavy-current electric options.* ***Originality.*** *First in a complex kind basic technical descriptions and proof-of-concept possibilities of unique high-voltage electrical equipment of Scientific-&-Research Planning-&-Design Institute «Molniya» of NTU «KhPI» are presented, being in Ukraine head organization in area of development, creation and practical application of the indicated high-voltage technique in behalf of domestic industries of IE, airplane and rocket production, and also defense industries of industry.* ***Practical value.*** *Application of the described domestic high-voltage proof-of-concept electrical equipment at tests on electric safety, EMC and resistibility to lightning of different objects of IE, OAMT, AT and SRT will be instrumental in the increase of reliability of their functioning in the conditions of striking (destabilizing) action on them of powerful electromagnetic hindrances of natural and artificial origin.* References 39, tables 9, figures 30.

Key words: **high-voltage generators of voltage and current pulses, objects of industrial energy, armament, aviation and space-rocket technique, standards of tests, results of tests of technical objects on electric safety, electromagnetic compatibility and resistibility to lightning.**

Виконаний аналіз основних технічних характеристик і нових можливостей складових частин унікального високовольтного електротехнічного комплексу НДПКІ «Молнія» НТУ «ХПІ», призначеного для проведення випробувань об'єктів промислової енергетики на електробезпеку, їх стійкість до дії стандартних аперіодичних грозових і комутаційних імпульсів напруги (струму), а також об'єктів озброєння і військової техніки, авіаційної і ракетно-космічної техніки на електромагнітну сумісність і блискавкостійкість при прямій дії на них нормованих імпульсів струму штучної блискавки. Показано, що дані випробування можуть проводитися відповідно до вимог нормативних документів США SAE ARP 5412: 2013, SAE ARP 5414: 2013, SAE ARP 5416: 2013, RTCA DO-160G: 2011, військових стандартів США MIL-STD-464C: 2010, MIL-STD-461G: 2015, стандартів НАТО AECTP-500: 2016, AECTP-250: 2014, міжнародних стандартів IEC 62305-1: 2010, IEC 61024-1: 1990 і міждержавного стандарту ГОСТ 1516.2-97 на оригінальних вітчизняних високовольтних установках УИТОМ-1, ГТМ-10/350, ГКИН-2, TI-CS115 (NCS08), TI-CS116 (NCS09), G-NCS10, МВ 1000 і ИК-1У з нормованими характеристиками. Приведені приклади і результати випробувань ряду технічних об'єктів на вказаних високовольтних слабко- і сильнострумних електроустановках. Бібл. 39, табл. 9, рис. 30.

Ключові слова: **високовольтні генератори імпульсів напруги і струму, об'єкти промислової енергетики, озброєння, авіаційної і ракетно-космічної техніки, стандарти випробувань, результати випробувань технічних об'єктів на електробезпеку, електромагнітну сумісність і блискавкостійкість.**

Выполнен анализ основных технических характеристик и новых возможностей составных частей уникального высоковольтного электротехнического комплекса НИПКИ «Молния» НТУ «ХПИ», предназначенного для проведения испытаний объектов промышленной энергетики на электробезопасность, их стойкость к воздействию стандартных апериодических грозовых и коммутационных импульсов напряжения (тока), а также объектов вооружения и военной техники, авиационной и ракетно-космической техники на электромагнитную совместимость и молниестойкость при прямом действии на них нормированных импульсов тока искусственной молнии. Показано, что данные испытания могут проводиться в соответствии с требованиями нормативных документов США SAE

© M.I. Baranov, S.G. Buriakovskyi, V.V. Kniaziev, S.S. Rudenko

ARP 5412: 2013, SAE ARP 5414: 2013, SAE ARP 5416: 2013, RTCA DO-160G: 2011, военных стандартов США MIL-STD-464C: 2010, MIL-STD-461G: 2015, стандартов НАТО AECTP-500: 2016, AECTP-250: 2014, международных стандартов IEC 62305-1: 2010, IEC 61024-1: 1990 и межгосударственного стандарта ГОСТ 1516.2-97 на оригинальных отечественных высоковольтных установках УИТОМ-1, ГТМ-10/350, ГКИН-2, TI-CS115 (NCS08), TI-CS116 (NCS09), G-NCS10, МВ 1000 и ИК-1У с нормированными характеристиками. Приведены примеры и результаты испытаний ряда технических объектов на указанных высоковольтных слабо- и сильноточных электроустановках. Библ. 39, табл. 9, рис. 30.
Ключевые слова: **высоковольтные генераторы импульсов напряжения и тока, объекты промышленной энергетики, вооружения, авиационной и ракетно-космической техники, стандарты испытаний, результаты испытаний технических объектов на электробезопасность, электромагнитную совместимость и молниестойкость.**

Problem definition. Powerful electromagnetic interference (PEMI) of natural and artificial origin is a serious threat to the reliable functioning of modern technology, based on the use of various radio, electrical and electronic equipment [1]. The world experience in the operation of such equipment (for example, military and civilian aircraft, launch vehicles, thermal (TPP), nuclear (NPP) and hydraulic (HPP) power plants) indicates that low-current electronics, which is part of its information technology systems and computer control networks, is extremely sensitive to the action of PEMIs on it [2]. One of the sources of PEMIs is long spark discharges in the Earth's air atmosphere (lightning) arising from a thundercloud to the earth, neighboring clouds, aircraft and various objects located on the Earth's surface [3]. Therefore, the issues of electromagnetic compatibility (EMC) in the field of modern technology have gained increased importance in the world. General requirements for EMC of equipment are regulated by the relevant Technical Regulations of Ukraine, similar to EU Directive 2014/30/EU [4]. Types of tests and methods for their implementation are described in Ukrainian Standards, identical to EU Standards of the 61000 and 55000 series. In 2004, the KT-160D Standard [5], similar to the corresponding US Standard RTCA DO-160D, was introduced in Ukraine to test the onboard equipment of civilian aircraft. In 2011, the next edition of this RTCA DO-160G Standard [6] was released in the USA, which has a number of significant differences from the previous RTCA DO-160D Standard. Obviously, the capabilities of testing laboratories in Ukraine should be adapted to the requirements of the new edition of this Standard. Section 22 of this Standard focuses on onboard equipment (OBE) tests on transient susceptibility caused by lightning. In all versions of the Standards from RTCA DO-160D to RTCA DO-160G, the basic requirements for OBE tests for lightning resistance have not practically changed, with the exception of some refinements and adjustments. These basic requirements include [5, 6]:

- temporary shapes and amplitude values of lightning test currents and voltages;
- types of test lightning discharges;
- methods for introducing interference from lightning into the OBE;
- OBE test regulations.

Of fundamental importance for the implementation of the Concept of the State Target Program for the Reform and Development of the Military-Industrial Complex of Ukraine, which was approved by Order of the Cabinet of Ministers of Ukraine No. 19-r of 01.20.2016, is the implementation of NATO Standards in Ukraine (in particular, according to EMC). These standards regulate the requirements for EMC parameters for objects of armament and military technique (OAMT) and their components, taking into account the combat arms and destination. Ensuring the necessary level of immunity of the OAMT samples to the action of various PEMIs will increase the defense capability of Ukraine and will promote the promotion of products of national manufacturers on international markets. By order of the National Standardization Body of Ukraine dated December 26, 2017 No. 471, from February 1, 2018, the following two basic NATO Standards came into force in our country by confirmation method: DSTU-P STANAG 4370 AESTP-500 Ed. E: 2017 [7] and DSTU-P STANAG 4370 AESTP-250 Ed. C: 2017 [8]. It should be noted that the stringent requirements of these NATO Standards are largely consistent with the requirements of similar US military Standards [9, 10]. Therefore, the implementation in Ukraine of tests of OAMT in accordance with NATO Standards will actually provide an opportunity to assess the compliance of our OAMT with the requirements of US military Standards, which are the most common in the world. Taking into account the novelty of the requirements of NATO Standards, in the paper it is advisable to analyze the technical characteristics of a number of new generators recently developed and created at Scientific-&-Research Planning-&-Design Institute «Molniya» of NTU «KhPI» for testing the stability of OAMT equipment to external (internal) PEMIs.

No less dangerous for the operation of power electric power equipment is such a source of PEMIs as switching overvoltages arising in electric power systems and networks of various voltage classes during regular switching on and emergency switching off of electric power consumers in them [11, 12]. In this regard, the development and use for practical purposes in the field of modern electrical technologies in assessing the real resistance and electric strength of the external (internal) insulation of electric power facilities of generators that reproduce switching voltage pulses with an amplitude of hundreds and thousands of kilovolts at industrial power (IP) facilities is relevant in world applied task. Emergency modes in their electrical circuits, accompanied by the flow of short-circuit currents (SC) with an amplitude of up to several tens of kiloamperes, are also dangerous for the reliable operation of power electrical equipment and electronic devices of power facilities of PE, aviation (AT) and space-rocket (SRT) technique [1, 11]. An electric charge of up to ±(50-200) C accumulated in thunderclouds due to electrophysical processes in the Earth's atmosphere during spark discharges from these clouds (for example, to ground objects or to objects

caught in flight in the Earth's atmosphere) causes flow in their plasma channels of a powerful pulse current of a complex temporal shape with amplitude of up to ±(30-200) kA [3]. In this regard, US guiding technical documents SAE ARP 5412: 2013 [13] and SAE ARP 5416: 2013 [14] define stringent requirements for the normalized amplitude-temporal parameters (ATPs) of artificial lightning current pulses generated by powerful high-voltage lightning current generators (LCG) and used in tests of AT and SRT objects for lightning resistance. The International Standard IEC 62305-1: 2010 [15] and the National Standard of the Russian Federation GOST R IEC 62305-1-2010 [16] regulate the current requirements for the standardized ATPs of the aperiodic pulsed current pulse of an artificial lightning of a temporary shape of 10 μs/350 μs generated by a powerful high-voltage LCG, typical for a short thunderstorm into ground-based power facilities and used in testing of various objects of IP for lightning resistance. The indicated high-voltage LCG allow determining the real EMC indicators and the resistance of IP, AT, and SRT objects to the direct effect of lightning strikes on them. Therefore, the development, creation and practical application of powerful high-voltage LCG are currently relevant applied scientific and technical tasks for the diverse infrastructure of industrialized countries of the world.

According to the analysis of observations of thunderstorm activity at 178 weather stations of the country, National Energy Company Ukrenergo established that the duration of thunderstorm activity in Ukraine is increasing by 100 hours annually. Over the past 5 years, about 350 emergency switches off have occurred on power lines of classes 220-750 kV as a result of a direct lightning strike, 50 of which were accompanied by SC. Therefore, lightning voltage (current) pulses are a serious threat to energy objects for their operation. The critical state in the reliability and safety of operation of energy facilities in Ukraine is confirmed by a number of major accidents due to malfunctions of their grounding devices (GDs). Among them: ignition of the power transformer of the Rivne NPP in 2019 due to SC with the subsequent operation of the protection and the erroneous disconnection of its power unit No. 3 from the Ukrainian power system; disconnection of a substation of voltage class of 330 kV in the south of the country due to a false actuation of its protection system; erroneous disconnection of power unit No. 1 of Zmievskaya TPP in 2019. In this regard, the diagnostics and modernization of the GDs of power facilities will ensure both the electrical safety of their maintenance personnel and other persons who may suffer from the removal of electrical potential outside the power facilities, as well as the normal operation of the equipment of TPPs, NPPs HPPs.

In contrast to the high-voltage test installations created in foreign countries in the field of electrical safety, EMC, and the resistance of technical facilities to the action of artificial lightning and PEMIs according to [4-10, 12-16], the high-current high-voltage test electric equipment available in Ukraine is characterized by the originality of constructing its discharge electric circuits with a global priority and made of domestic components, structural and insulating materials [17-24]. For well-known reasons, the acquisition of expensive foreign electrical installations is an unrealistic task for us. In this regard, it is necessary to rely on our own original developments and electrical installations that implement the requirements of [4-10, 12-16]. Electrical installations of Ukraine for the implementation of the requirements of a number of US and NATO Standards [4-10] have not been described in literature.

The goal of the paper is analysis of the main technical characteristics and new capabilities of individual electrical installations of the high-voltage electrical complex Scientific-&-Research Planning-&-Design Institute «Molniya» of NTU «KhPI» designed to test IP objects for electrical safety, the effect of standard lightning and switching voltage (current) pulses on them, as well as OAMT, AT and SRT on EMC and resistance to action on them of normalized current pulses of artificial lightning and a number of special temporary shapes of current pulses (voltage).

1. A generator of full current artificial lightning with amplitude of up to ±200 kA. In 2007, the staff of the Scientific-&-Research Planning-&-Design Institute «Molniya» of NTU «KhPI» at its scientific and experimental training ground (Andreevka, Kharkiv region) created a powerful high-voltage high-current LCG of the UITOM-1 type [17], capable of testing elements of AT and SRT objects on lightning resistance in accordance with international requirements [13, 14]. According to US technical requirements [13, 14], in laboratory tests of devices and elements of aviation and rocket and space technology for resistance to the direct effect of full current of artificial lightning on them, its following components generated in high-voltage high-current LCG circuits can be used: pulsed *A*-, repeated pulsed *D*-, intermediate *B*-, long-term C- and shortened long-term *C**- current components of artificial lightning. We point out that most often in the practice of lightning tests of various devices and systems of civil and military aircraft, the following combinations of the indicated lightning current components are used [13, 17]: *A*-, *B*- and *C*-components; *A*-, *B*- and *C**- components; *D*-, *B*- and *C**-components. The main ATPs normalized according to [13, 14], typical for such components of the artificial lightning current in the electrical circuits of the LCG, can be summarized in Table 1.

Table 1

Normalized ATPs of the main components of the total current of artificial lightning [13, 14]

Lightning current component	I_m, kA	I_C, kA	q_C, C	J_a, 10^6 J/Ω	τ_f, μs	τ_p, ms
A	200±20	–	–	2±0.4	≤50	≤0.5
B	–	2±0.4	10±1	–	–	5±0.5
C	0.2-0.8	–	200±40	–	–	(0.25–1) ×10^3
*C**	–	0.4	6-18	–	–	15-45
D	100±10	–	–	0.25±0.05	≤25	≤0.5

Note. I_m is the amplitude of the current pulse; I_C is the average current value; q_C is the amount of the flowing charge; J_a is the integral of the action of the current pulse; τ_f, τ_p are, respectively, the duration of the pulse front between the levels (0.1-0.9)I_m and the current pulse at the level ≤0.1I_m.

Figure 1 shows a general view of a powerful LCG of the UITOM-1 type, and Fig. 2 is a schematic electrical diagram of the construction of this artificial lightning full-current generator. In accordance with the data in Fig. 2, the UITOM-1 type generator includes five separate and synchronously operating high-voltage pulse current generators (GIT) of capacitive design, each of which (GIT-*A*, GIT-*D*, GIT-*B*, GIT-*S* and GIT-*C**) on common electric load – the test object (TO) forms the corresponding components of the total current of artificial lightning [17]. The required combination of lightning current components (and, accordingly, the necessary combination of GIT) on a common TO is implemented using electrical jumpers X1-X4 (see Fig. 2).

Fig. 1. General view of the high-voltage high-current LCG of the UITOM-1 type, which simulates the direct influence of the main components of the artificial lightning current on the TO (in the foreground there is a working table with a three-electrode controlled air switch F_1 for voltage of ±50 kV and an air exhaust system, and in the background there are powerful high-voltage generators GIT-*A*, GIT-*D*, GIT-*B*, GIT-*C* and GIT-*C**) [17, 18]

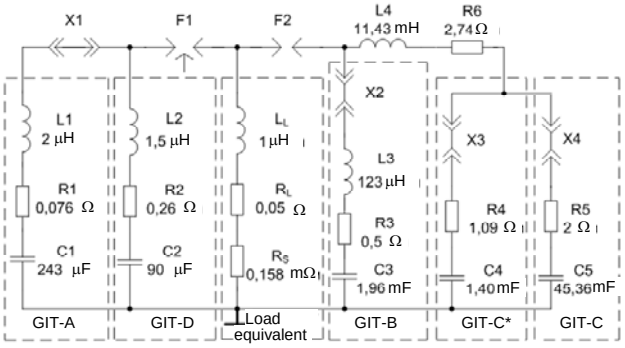

Fig. 2. Electrical circuits for the construction of discharge circuits of five high-voltage GITs (GIT-*A*, GIT-*D*, GIT-*B*, GIT-*C* and GIT-*C**) and UITOM-1 type LCG in general with one common electric R_LL_L load (F_1, F_2 – three- and two-electrode high-current air switches for voltage ±50 kV and ±5 kV; *X*1-*X*4 – electrical jumpers; R_S=0.158 mΩ – active resistance of the measuring coaxial shunt ShK-300M1; *R*1-*R*5, *L*1-*L*3 – own electrical parameters of the circuits of GIT-*A*, GIT-*D*, GIT-*B*, GIT-*C** and GIT-*C*; *R*6, *L*4 – electrical parameters of the forming elements for the circuits of GIT-*C* and GIT-*C**) [18]

Powerful GIT-*A* and GIT-*D* generators are equipped with parallel-connected high-voltage low-inductance capacitors of the type IK-50-3 (they are charged to constant voltage $\pm U_{CA}$ of not more than ±50 kV), and GIT-*B*, GIT-*C* and GIT-*C** generators with high-voltage low-inductance capacitors of the IM-5-140 type (the latter are charged, respectively, to constant voltage $\pm U_{CB}$ and $\pm U_{CC}$ not more than ±5 kV). As a result, the total nominal energy stored in the UITOM-1 type LCG capacitors is 1.21 MJ [18].

To measure the ATPs generated by these LCGs at the TO (according to Fig. 2 on the total lumped R_LL_L load R_L≈50 mΩ и L_L≈1 μH) of all components of the pulsed lightning current, one measuring high-voltage coaxial shunt of the ShK-300M1 type, with active resistance of R_S=0.158 mΩ and passed the state metrological verification is used [18].

Table 2 shows the main technical characteristics of a measuring high-current coaxial shunt of the ShK-300M1 type, the high-resistance disk element of which 1 mm thick and outer diameter of 80 mm was made of 12X18H10T stainless steel [19]. The design of this measuring shunt is capable of withstanding repeated full currents of artificial lightning flowing through it, characterized by the action integral up to J_a≈10·10^6 J/Ω.

Table 2

Main technical characteristics of the measuring shunt type ShK-300M1 [18, 19]

Shunt name	Characteristic value		
	R_S, mΩ	K_S, A/V	Mass, kg
ShK-300M1	0.158±1 %	K_{SA}=12625	3.1
		K_{SC}=6312	

Note. K_S=2/R_S is the shunt conversion coefficient, A/V; K_{SA} is the shunt conversion coefficient when measuring in the LCG discharge circuit of the ATPs of *A*- and *D*- components of the artificial lightning current, A/V (from the 1:1 coaxial connector of the matching voltage divider (MVD) type SDN-300); K_{SC} is the shunt conversion coefficient when measuring in the LCG discharge circuit of the ATPs of *B*-, *C*- and *C**- components of the artificial lightning current, A/V (from the 1:2 coaxial connector of the SDN-300 voltage divider matched).

Figures 3-5 show typical oscillograms of pulsed *A*-, intermediate *B*- and long-term *C*- components of the artificial lightning current normalized according to [13, 14] ATPs previously recorded in high-current discharge circuits of high-voltage generators GIT-*A*, GIT-*B* and GIT-*C* of the powerful LCG *of* UITOM-1 type using the ShK-300 measuring shunt (K_{SA}=11261 A/V; K_{SC}=5642 A/V [17]) and Tektronix TDS 1012 digital storage oscilloscopes. Designs of the used ShK-300 and ShK-300M1 shunts, as well as the original schemes for constructing measuring channels in the UITOM-1 LCG allow simultaneously registering the required combinations of lightning current components [18].

In Fig. 4 interesting metrological features are almost ideal zones (time zones located on the horizontal time axis in the regions of 300 μs and 5 ms) of «joining» or «stitching» of the measured current curves corresponding to the *A*-, *B*- and *C*- components of the full current of artificial lightning generated by a powerful LCG of the UITOM-1 type [17, 18]. The practical implementation of this approach while simultaneously recording the indicated components of the artificial lightning current was carried out by using a single voltage divider type SDN-300 in the measuring path.

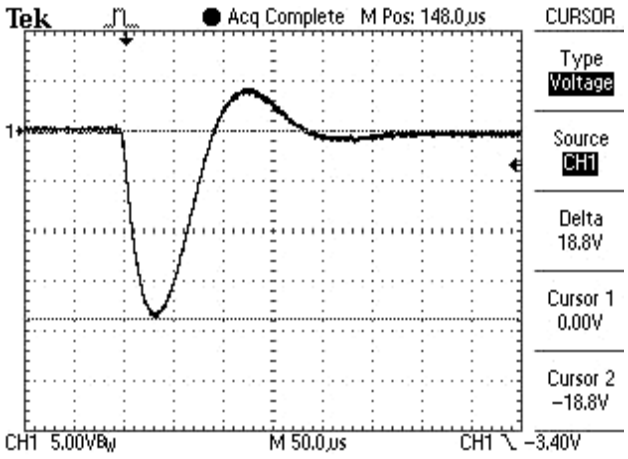

Fig. 3. Oscillogram of the pulsed *A*- component of the artificial lightning current with normalized ATPs in the high-current discharge circuit of the GIT-*A* generator of a powerful LCG of the UITOM-1 type (U_{3A}≈−29.7 kV; I_{mA}≈–212 kA; J_{aA}≈2.09·10^6 J/Ω; τ_f≈32 µs; τ_p≈500 µs; vertical scale – 56.3 kA/cell; horizontal scale – 50 µs/cell) [17]

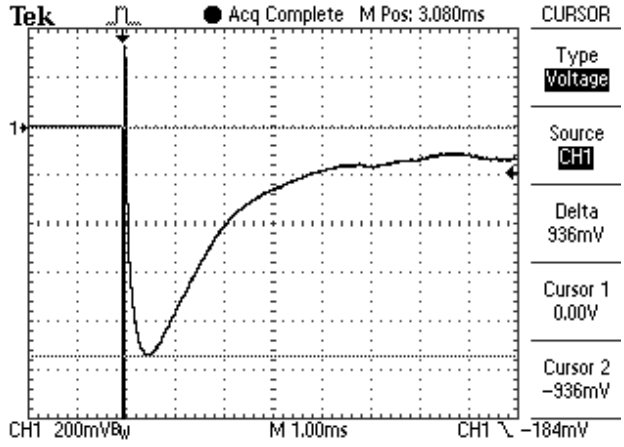

Fig. 4. Oscillogram of the intermediate *B*- component of the artificial lightning current with normalized ATPs in the high-current discharge circuit of the GIT-*B* generator of a powerful LCG of the UITOM-1 type (U_{3B}≈−4 kV; I_{mB}≈–5.28 kA; I_C≈2.08 kA; q_{CB}≈–10.4 C; τ_p≈5 ms; vertical scale – 1128.4 A/cell; horizontal scale − 1 ms/cell) [17]

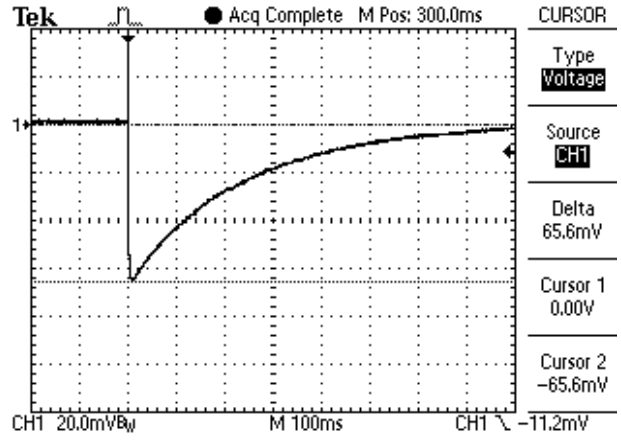

Fig. 5. Oscillogram of the long-term *C*- component of the artificial lightning current with normalized ATPs in the high-current discharge circuit of the GIT-*C* generator of a powerful LCG of the UITOM-1 type (U_{3C}≈−4 kV; I_{mC}≈–0.74 kA; q_{CC}≈–182 C; τ_f≈9 ms; τ_p≈1000 ms; vertical scale – 225.6 A/cell; horizontal scale − 100 ms/cell) [17]

Figure 6 shows the results of direct exposure to a pilot model of a domestic-produced aircraft receiving-transmitting antenna of only one pulsed *A*- component of the artificial lightning current, normalized according to [13, 14] the ATPs of which corresponded to the technical data indicated on the current oscillogram of Fig. 3 (I_{mA}≈–212 kA; J_{aA}≈2.09·10^6 J/Ω; τ_f≈32 µs; τ_p≈500 µs) [20].

The data in Fig. 6 clearly shows that the experimental model of the receiving-transmitting antenna of a domestic aircraft, designed and manufactured without fully taking into account the international requirements for lightning resistance given in the US regulatory documents [13, 14], underwent its complete destruction after direct exposure to its radio elements of pulsed *A*- artificial lightning current components with normalized ATPs.

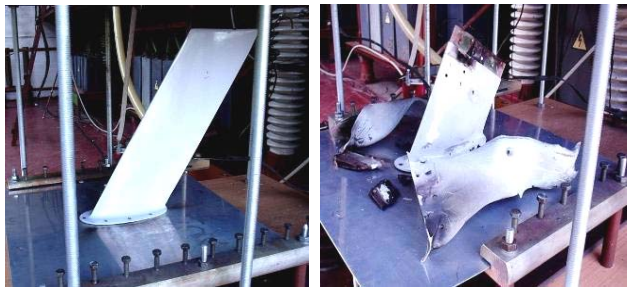

a *b*

Fig. 6. External view of the experimental model of the receiving-transmitting antenna of a domestic aircraft before (*a*) and after (*b*) the direct impact on it in a high-current discharge circuit of a high-voltage generator GIT-*A* of a powerful LCG type UITOM-1 of only one pulsed *A*- component of the artificial lightning current with normalized ATPs (I_{mA}≈–212 kA; J_{aA}≈2.09·10^6 J/Ω; τ_f≈32 µs; τ_p≈0.5 ms) [20]

The UITOM-1 powerful high-voltage lightning current generator based on schemes for constructing and synchronizing the parallel operation of the discharge circuits of its five separate GITs, stored in capacitor banks electric energy, generated on the tested R_LL_L load normalized ATPs of the components of the artificial lightning current and its comparatively low cost does not have foreign analogues [17].

2. A current pulse generator of a temporary shape 10/350 µs of artificial lightning with amplitude of up to ±200 kA. In 2014, at the indicated scientific and experimental training ground of the Scientific-&-Research Planning-&-Design Institute «Molniya» of NTU «KhPI», we created a unique powerful high-voltage high-current generator of current of short-term lightning strike of the GTM-10/350 type [21], on which tests of various ground-based IP objects can be carried out on lightning resistance to the direct action on them of an aperiodic current pulse of artificial lightning of a temporary shape τ_f/τ_p=(10±2) µs/(350 ± 35) µs of both polarities in accordance with the technical requirements set forth in international regulatory documents [15, 16]. The main normalized ATPs of this powerful test pulse of artificial lightning current, corresponding to a short shock of a thunderstorm high-current discharge into a protected electric power object (TO), are given in Table 3. From the data of Table 1, 3 it follows that the powerful test current

pulse of a short thunderstorm high-current discharge of a temporary shape of 10/350 μs in terms of its energy indicators (first of all, by the value of the corresponding integral of the current action J_a) significantly exceeds the corresponding numerical indicators for pulsed *A*- and repeated pulsed *D*-component of the artificial lightning current (see section 1) used in testing of various objects of AT and SRT for lightning resistance in accordance with the regulatory documents in force [13, 14].

Table 3

Normalized ATPs of an aperiodic current pulse of a temporary shape 10 μs/350 μs [15, 16]

Name of the current pulse parameter	Lightning protection level according to the Standard IEC 62305-1: 2010		
	I	II	III-IV
Front duration τ_f, μs	10±2	10±2	10±2
Pulse duration τ_p at the level $0.5I_m$, μs	350±35	350±35	350±35
Current amplitude I_m, kA	200±20	150±15	100±10
Current action integral J_a, 10^6 J/Ω	10±3.5	5.6±1.96	2.5±0.875
Charge q_C, C	100±20	75±15	50±10

Figure 7 shows a general view of the generator type GTM-10/350, and Fig. 8 shows the electrical circuits for constructing (replacing) of its four separate high-voltage GITs (GIT-1 – GIT-4, synchronously working on one common electric R_LL_L load) and this generator as a whole.

Fig. 7. General view of a powerful high-voltage high-current generator of artificial lightning type GTM-10/350 (in the foreground there is its desktop with a controllable high-voltage three-electrode air switch placed on top of it with graphite electrodes for voltage ±50 kV and pulsed aperiodic lightning current with amplitude up to ±220 kA and a test sample of cable and wire products, and in the background there are the electrical elements of the charge-discharge circuits of its individual high-voltage pulse current generators GIT-1, GIT-2, GIT-3 and GIT-4) [21]

Note that the GIT-1 – GIT-3 generators are equipped with high-voltage low-inductance pulse capacitors type IK-50-3 (rated voltage ±50 kV; rated capacitance 3 μF), and the GIT-4 generator is equipped with high-voltage pulse capacitors of the IM2-5-140 type (rated voltage ±5 kV; rated capacitance 140 μF) [21]. In the GIT-1 – GIT-3 generators, their capacitors (respectively, in the amount of 16, 44 and 111 pcs.) are connected in parallel to the rated voltage of ±50 kV, and in the GIT-4 generator its capacitors (in the amount of 288 pcs.) – in series in parallel (two series-connected capacitors in each of the 144 parallel-connected sections) for rated voltage of ±10 kV. As a result, the total nominal energy stored in a high-voltage high-current generator of artificial lightning type GTM-10/350 is approximately equal to 1.15 MJ [21].

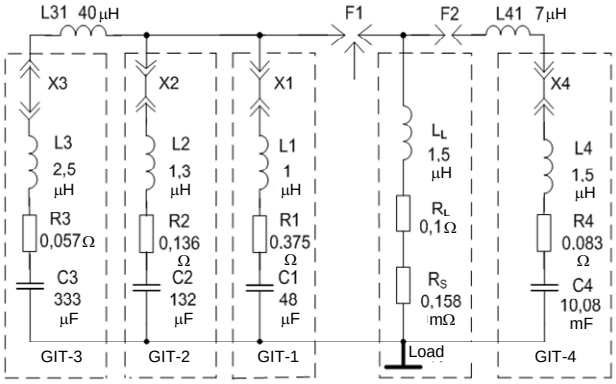

Fig. 8. Electrical equivalent circuits of high-current discharge circuits of four separate high-voltage generators GIT-1 – GIT-4 as parts of a high-power current pulse generator 10/350 μs of artificial lightning type GTM-10/350, working on one common electric R_LL_L load ($X1 - X4$ – conductive jumpers of discharge circuits of GIT-1 – GIT-4; $R1$-$R4$, $L1$-$L4$ – own electrical parameters of circuits of GIT-1 – GIT-4; $L31$, $L41$ – electrical parameters of forming reactive elements for discharge circuits of generators GIT-3 and GIT-4) [21, 22]

Figure 9 shows an oscillogram of a powerful aperiodic current pulse of a temporary shape of 10/350 μs with normalized ATPs obtained in a high-current discharge circuit of a high-voltage generator of the GTM-10/350 type with a low-resistance active-inductive load (R_L≈0.1Ω; L_L≈1.5 μH).

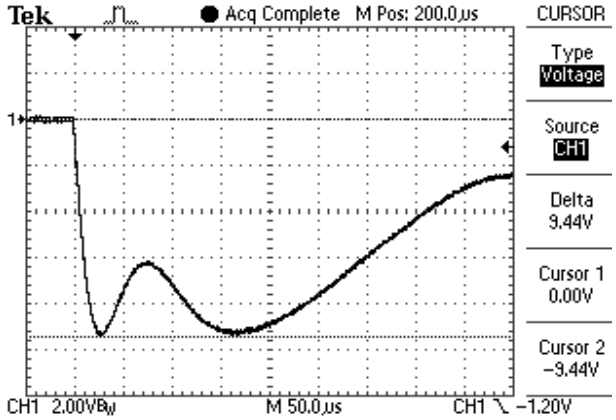

Fig. 9. Oscillogram of an aperiodic current pulse of negative polarity in a high-current discharge circuit of a high-voltage generator GTM-10/350 with an active-inductive load (R_L≈0.1 Ω; L_L≈1.5μH; $U_{31\text{-}3}$=−15 kV; U_{34}=−2.25 kV; I_m≈–106 kA; J_a≈3.03·10^6 J/Ω; q_C≈–52.2 C; τ_f≈15 μs; τ_p≈340 μs; vertical scale – 22.52 κA/cell; horizontal scale − 50 μs /cell) [22]

The ATPs of the aperiodic current pulse of artificial lightning (see Fig. 9), formed in the discharge circuit of

the GTM-10/350 generator, was measured using a ShK-300 type coaxial shunt (K_S = 11261 A/V [17]) and digital storage oscilloscope series Tektronix TDS 1012. The charging voltage $U_{C1\text{-}3}$=$U_{31\text{-}3}$ of negative polarity of the capacitors for the generators GIT-1 – GIT-3 in this case was about 15 kV, and the charging voltage U_{C4}=U_{34} of the same polarity of the individual capacitors for the generator GIT-4 was 2.25 kV.

Figure 10 shows the results of the impact on a solid aluminum core with cross section of 6 mm^2 of АППВнг2×6 network cable with polyvinylchloride (PVC) insulation of an aperiodic current pulse of a short shock of a lightning discharge of a temporary shape of 17/265 μs with amplitude I_m≈ –83.8 kA obtained in a discharge circuit of GTM-10/350 [23].

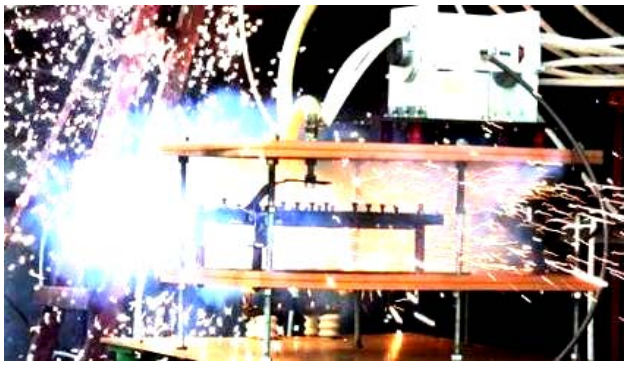

Fig. 10. Results of the electrothermal action in the discharge circuit of the GTM-10/350 type artificial lightning current generator of a normalized aperiodic current pulse of a short thunderstorm discharge of a temporary shape of 17/265 μs with amplitude of I_m≈ –83.8 kA on the test sample of the АППВнг2×6 network cable with PVC insulation and solid aluminum core of cross section of 6 mm^2 [23]

From the data in Fig. 10 it is shown that the test sample of АППВнг2×6 network cable with PVC insulation (TO) could not stand the indicated electrothermal effect of normalized to [15, 16] aperiodic current pulse of artificial lightning. Its continuous round aluminum core with cross section of 6 mm^2 together with its PVC insulation due to the onset of an electric explosion (EE) in it (the core) underwent sublimation and complete destruction. Note that the EE of the tested in the discharge circuit of the GTM-10/350 for thermal resistance to the indicated powerful current pulse of artificial lightning of a test sample of the network cable with a current-carrying aluminum part causes a noticeable deformation of the current pulse acting on it. In this case, the values of τ_f increase and the values of τ_p decrease. A powerful high-voltage lightning current generator of the type GTM-10/350 has no foreign analogues according to the schemes for constructing and synchronizing the parallel operation of the discharge circuits of four separate GITs, stored in capacitor banks of electric energy, generated at the R_LL_L load the normalized ATPs of a lightning current pulse of a short shock and its relatively low cost [21].

3. A generator of standard switching aperiodic voltage pulses with amplitude of up to ±2 MV. To test the electrical strength of the insulation of objects at the scientific and experimental training ground of the Scientific-&-Research Planning-&-Design Institute «Molniya» of NTU «KhPI», in 2012 a powerful generator of switching voltage pulses (GSVP) was created, which allows generating on the electrical load with a capacitive characteristic (for example, on insulators, high voltage bushings , disconnectors, capacitors, transformers, etc.) standard aperiodic voltage pulses of positive (negative) polarity of the temporal shape T_g/τ_p≈205 μs/1900 μs, where T_g, τ_p are, respectively, the rise time and duration at the level of 0.5 U_m of the voltage pulse, at their amplitude U_m up to ±2 MV [12, 24]. Figure 11 is a general view of this ultra-high-voltage generator.

Fig. 11. General view of GSVP of GKIN-2 type, which forms a standard aperiodic switching pulse of voltage of a temporary shape T_g/τ_p ≈205/1900 μs with amplitude U_m up to 2 MV on the tested electric power facility (the modernized generator GIN-4 is placed on the right, and an insulating support 11 m high with load capacitance C_l≈13.3 nF for 3 MV, to the upper potential electrode of which from the GIN-4 generator forming R_f≈4.28 kΩ and from the load capacitance – current-limiting R_l ≈4.59 kΩ resistors are connected) [24]

Figure 12 shows a circuit diagram of an ultra-high-voltage generator GKIN-2, assembled on the basis of using a modernized by us in 2012 for generating on test objects (TO) at electric power facilities in accordance with the requirements of [12] of a standard switching aperiodic voltage pulse of a temporary shape (250±50) μs/(2500±750) μs of a pulse voltage generator (PVG) for rated voltage of 4 MV and stored electric energy up to 1 MJ [25], built on the indicated training ground (field stand) of the Institute in the 1970s according to the classical Arkadyev-Marx scheme [26]. Note that GIN-4 (see Fig. 12) has a bookcase structure and contains 16 cascades, each of which (with the exception of the first cascade from the ground) includes one uncontrolled air two-electrode ball spark gap F with diameter of 125 mm and eight high-voltage capacitors C in the metal case KBMG-125/1 (rated voltage ±125 kV; capacitance 1 μF) of our own design [25, 27].

The first cascade of the GIN-4 generator from the ground is equipped with a high-voltage controlled air three-electrode spark gap (trigatron) F_1 of diameter of 125 mm, started from a special start-up pulse generator (SPG) of own design of the Scientific-&-Research Planning-&-Design Institute «Molniya» of NTU «KhPI», which supplies damped pulses microsecond duration to the trigatron F_1 electrodes, characterized by voltage amplitude of up to ±10 kV [28].

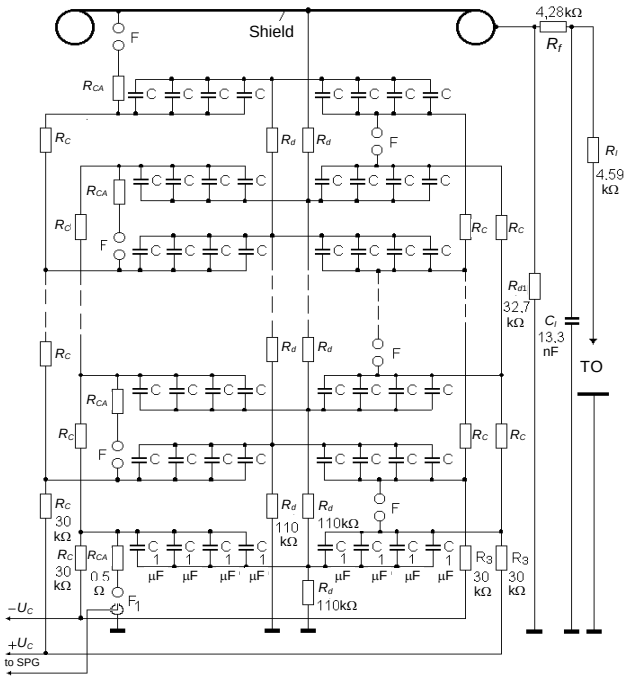

Fig. 12. Schematic diagram of the ultra-high-voltage GKIN-2 generator, assembled on the basis of the modernized powerful bipolar generator GIN-4 for rated voltage of 4 MV, connected to the proposed circuit for the formation of standard switching aperiodic voltage pulses on the TO (two-electrode needle-plane system with a long air discharge gap) containing an additional discharge resistor R_{d1}=32.7 kΩ, forming resistor R_f =4.28 kΩ, load capacitance C_l= 13.3 nF and current-limiting resistor R_l=4.59 kΩ [24]

The GIN-4 modernized by us in each of the charge branches of positive and negative polarities to constant voltage $\pm U_C$ of capacitors C with porcelain insulators (see Fig. 12) contains instead of low-resistance charging resistors with nominal value of 500 Ω the high-resistance charging resistors R_C=30 kΩ with a total of 32 pcs.

Each of the 16 GIN-4 cascades for a rated voltage of 250 kV is equipped with one soothing resistor R_{CA}=0.5 Ω. The parallel charge of capacitors C in GIN-4 to the corresponding constant voltage $\pm U_C$=$\pm U_3$ is carried out from two powerful high-voltage chargers of the GKIN-2 through four chains of series-connected charging R_C=30 kΩ (16 pcs. for each of two bipolar branches of charge) and two chains of series-connected discharging R_d=110 kΩ (8 pcs. each with a total discharge resistance of GIN-4 equal to 440 kΩ) resistors, each of which was calculated for rated voltage of 500 kV. The GIN-4 construction at the top contains a rectangular steel shield with round edges connected to its discharge circuit, to which shown in Fig. 12 forming elements and the required TOs are galvanically connected.

Figure 13 shows an oscillogram of a full standard switching aperiodic voltage pulse of positive polarity of a temporary shape T_g/τ_p≈205/1900 μs with amplitude U_m≈783.2 kV, obtained using the discharge of the described ultra-high-voltage generator GKIN-2 for an electrical load (TO), made in the form a long air gap (about 3 m long) in a two-electrode needle-plane system (Fig. 14, a steel rod was used for the «needle», and 5×5 m galvanized sheets were used for the «plane»).

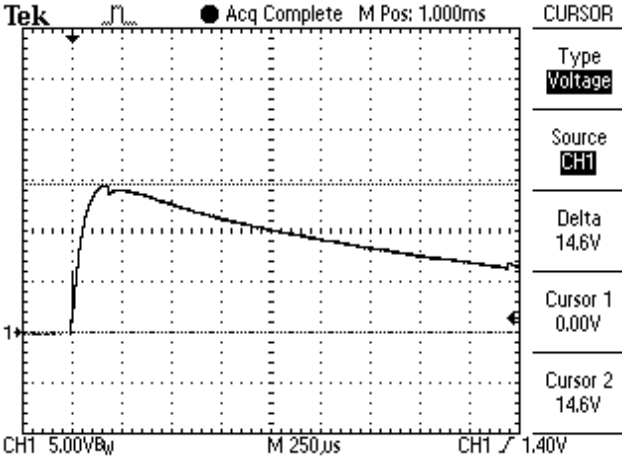

Fig. 13. Oscillogram of a full switching aperiodic voltage pulse of positive polarity on a needle-plane two-electrode system with an air gap of 3 m (U_3≈±40 kV; U_m≈783.2 kV; T_g≈205 μs; τ_p≈1900 μs; vertical scale – 268.2 kV/cell; horizontal scale – 250 μs/cell) [29]

Fig. 14. General view of the TO – a two-electrode needle-plane system with an air gap of 3 m, to the upper electrode of which GKIN-2 and the measuring ohmic divider of the pulse voltage ODN-2 to rated voltage of ±2.5 MV are galvanically connected [29]

Note that when measuring the ATPs of switching pulses of voltage of a temporary shape T_g/τ_p≈205/1900 μs, formed in the discharge circuit of the GKIN-2 in the TO shown in Fig. 14, an ODN-2 type ultra-high-voltage ohmic pulse voltage divider [29] matched in the measuring circuit having a division ratio K_d ≈ 53650 and a shielded cable transmission line from the TO of a useful electrical signal up to 60 m in length, and a Tektronix digital storage oscilloscope TDS 1012, located away from the considered GKIN-2 in a buried shielded measuring hopper, were used.

Figure 15 shows an oscillogram of a positive-polarity aperiodic switching voltage pulse of amplitude

U_m≈1030 kV cut off at the front obtained with GKIN-2 during electrical breakdown of air insulation of 3 m in length in the needle-plane two-electrode discharge system shown in Fig. 14. It can be seen that in this case, the cutoff time is T_C≈90 μ.

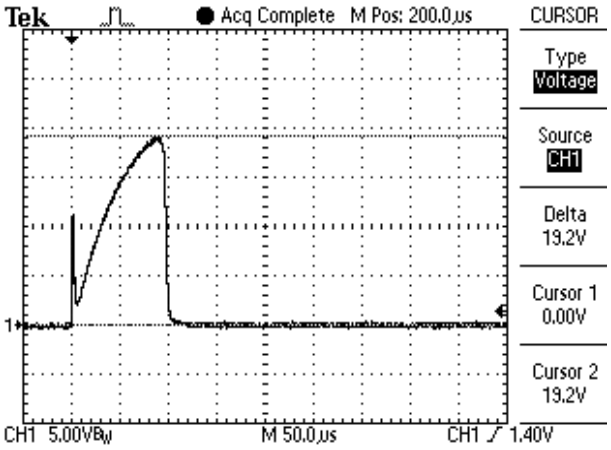

Fig. 15. Oscillogram of a cut off ultra-high-voltage switching aperiodic voltage pulse of positive polarity on a two-electrode needle-plane system with an air gap of 3 m (U_3≈±60 kV; U_m≈1030 kV; T_C≈90 μs; vertical scale – 268.2 kV/cell; horizontal scale − 50 μs /cell) [29]

We indicate that from the data in Fig. 13, 15 it follows that at the front of the switching aperiodic voltage pulse of the temporary shape T_g/τ_p≈205/1900 μs generated by the GKIN-2, a peak-like burst of up to 7 μs duration is observed [24], due to the operation peculiarity of the GKIN-4 ultra-high-voltage generator used in the test circuit, associated with the presence in it of a steel roof-top screen with area of up to 60 m^2 and a fast charge-discharge of its parasitic electric capacitance in the process of a powerful discharge to forming electrical elements and TO according to the diagram in Fig. 12 of power capacitors C = 1 μF of all GIN-4 cascades (with the capacitance «in the discharge» of this PVG equal to approximately 0.125 μF) when its high-voltage spark gaps F_1 and F are triggered. The GKIN-2 powerful ultra-high-voltage generator of aperiodic switching voltage pulses does not have foreign analogues today [24] according to the schemes for constructing its charge-discharge circuits (cascades) and normalized ATPs of the standard aperiodic switching pulse of 250/2500 μs voltage generated at the test object.

4. A generator TI-CS115 (NCS08). This generator is designed to test the components of the OAMT for conductive susceptibility to pulsed currents of the form CS115 [9] and NCS08 [7]. Test currents are supplied into the TO by feeding them into cable bundles through injectors. A general view of this generator is shown in Fig. 16.

The test current pulse generated by the TI-CS115 (NCS08) type generator on an electric load has a trapezoidal shape with a rise time of the front T_F≈2 ns, a fall time T_D≈2 ns and a horizontal section duration T≈30 ns. Figures 17-19 show typical oscillogram of a test current pulse of the shape required by [9].

Fig. 16. Generator of type TI-CS115 (NCS08), which reproduces pulse currents of the form CS115 [9] and NCS08 [7] on the TO

The output characteristics of the generator TI-CS115 (NCS08) are given in Table 4. The generator of pulsed currents of the type CS115 [9] and NCS08 [7] does not have known foreign analogues according to ATPs of special shaped test current pulses (see Fig. 17-19).

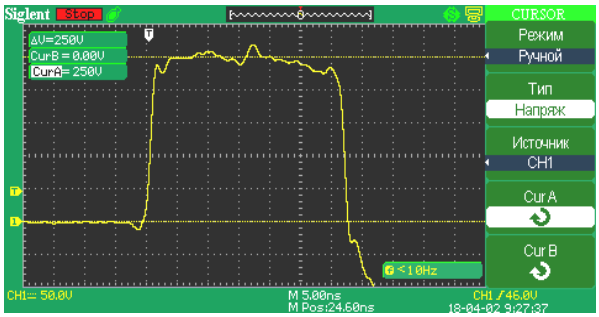

Fig. 17. Typical oscillogram of a test current pulse of the form CS115 with amplitude of 5 A of positive polarity generated by a generator of the type TI-CS115 (NCS08)

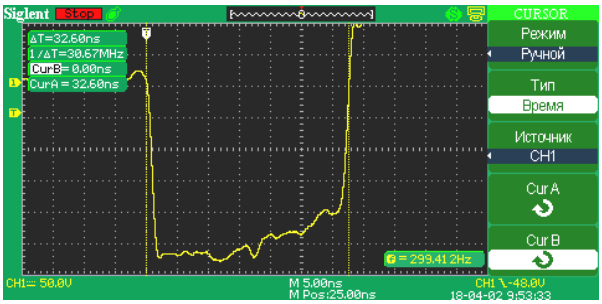

Fig. 18. Typical oscillogram of a test current pulse of the form CS115 with amplitude of 5 A of negative polarity generated by a generator of the type TI-CS115 (NCS08)

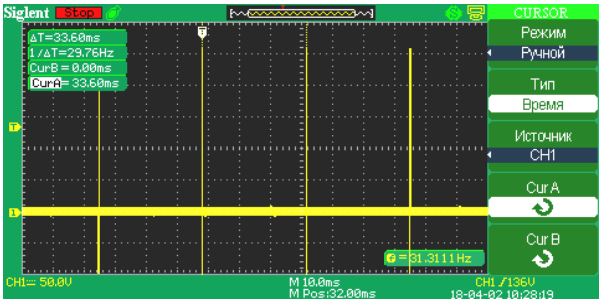

Fig. 19. Typical oscillogram of the repetition rate f_F =30 Hz of a test current pulse of the form CS115 generated by a generator of the type TI-CS115 (NCS08)

Table 4

Results of determining the characteristics of the generator TI-CS115 (NCS08) in the mode of measuring its current pulses

Technical characteristics of the output current pulse	Current I_p, A	T, ns	T_F, ns	T_D, ns	f_F, Hz	Pulse shape
Requirements of regulatory documents [7, 9]	5+1	not less than 30 ns	no more than 2 ns	no more than 2 ns	30 Hz ± 3 Hz	Trapezoid
Actual values for positive pulse	5±0.06	32.8	1.92	1.92	29.94±0.27	Trapezoid
Actual values for negative pulse	5±0.07	32.6	1.96	1.84	29.94±0.36	Trapezoid
Conclusion of compliance	meet	meet	meet	meet	meet	meet

Note: T is the duration of the horizontal part of the current pulse; T_F is the rise time of the front of the current pulse; T_D is the decay time of the current pulse; f_F is the repetition rate of current pulses.

5. A generator TI-CS116 (NCS09). This high-frequency generator is designed to test the components of the OAMT for conductive susceptibility to pulsed currents of the type CS116 [9] and NCS09 [7] also by the method of feeding test current pulses formed by it into the bundles of their cables through injectors. In this case, the current pulses have the shape of a damped sine wave, the frequency f_0 of which varies in the range from 10 kHz to 80 MHz. The current values are set depending on the frequency f_0 of the sinusoidal oscillations of the pulse current. The decrement of current oscillations is also regulated by the requirements of [7, 9]. The external view of the TI-CS116 (NCS09) type generator is shown in Fig. 20.

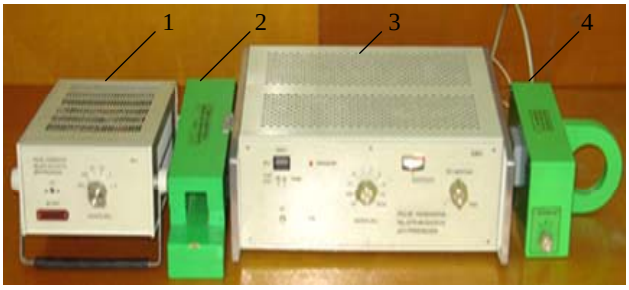

Fig. 20. General view of a high-frequency generator of the type TI-CS116 (NCS09) (1 – block F1; 2 – injector IG-3; 3 – power supply unit DP; 4 – block F2 with an inserted module M10)

The block diagram of the construction of this generator is shown in Fig. 21, and the main technical data on the parameters of the pulse current generated by it are given in Table 5, 6.

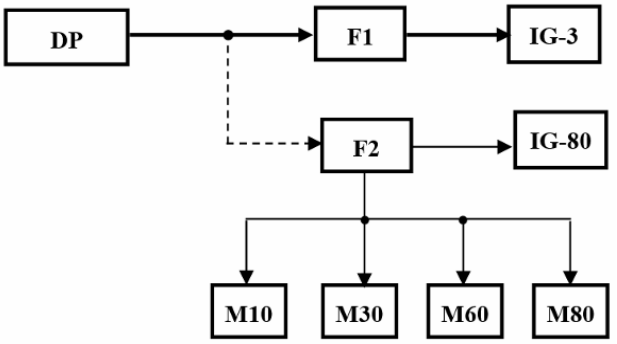

Fig. 21. Block diagram of the construction of a high-frequency generator of the TI-CS116 (NCS09) type (DP – power supply and switch control unit; F1 – frequency generation unit from 10 kHz to 3 MHz; F2 – frequency generation unit from 10 MHz to 80 MHz; M10 – replaceable module with frequency of 10 MHz; M30 – replaceable module with frequency of 30 MHz; M60 – replaceable module with frequency of 60 MHz; M80 – replaceable module with frequency of 80 MHz; IG-3 – injector for frequencies from 10 kHz to 3 MHz; IG-80 – injector for frequencies from 10 MHz to 80 MHz)

Table 5

Dependence of the peak value of the pulse current I_P on its frequency f_0

Frequency f_0, MHz	0.01	0.03	0.1	0.3	1	3	10	30	60	80
Current I_P in accordance with RD [7, 9], A	0.1+0.02	0.3+0.06	1+0.2	3+0.6	10+2	10+2	10+2	10+2	5+1	3.8+0.8
Current I_P according to the results of verification, A	positive polarity of pulse current									
	0.101±0.002	0.3±0.001	1.01±0.013	3±0.08	10.08±0.05	10.08±0.009	10.08±0.05	10.08±0.11	5.04±0.04	3.84±0.02
	negative polarity of pulse current									
	0.101±0.002	0.3±0.003	1.01±0.007	3±0.08	10.08±0.04	10.08±0.009	10.08±0.05	10.08±0.008	5.04±0.04	3.84±0.03

Table 6

Dependence of the pulse current I_P by cycles on frequency f_0

N (cycle number)	I_N/I_P in accordance with RD [7, 9]	Frequency f_0, MHz									
		0.01	0.03	0.1	0,3	1	3	10	30	60	80
		I_N/I_P according to the results of verification (I_N – current of the N-th cycle; I_P − rated current)									
1	from 0.73 to 0.85	positive polarity of pulse current									
		0.85	0.80	0.81	0.83	0.73	0.73	0.73	0.73	0.75	0.74
		negative polarity of pulse current									
		0.85	0.80	0.81	0.83	0.73	0.73	0.73	0.73	0.75	0.74
2	from 0.53 to 0.73	positive polarity of pulse current									
		0.59	0.60	0.58	0.65	0.59	0.54	0.59	0.55	0.54	0.54
		negative polarity of pulse current									
		0.59	0.60	0.58	0.65	0.59	0.54	0.59	0.55	0.54	0.54
3	from 0.39 to 0.62	positive polarity of pulse current									
		0.40	0.43	0.43	0.49	0.48	0.44	0.44	0.39	0.39	0.40
		negative polarity of pulse current									
		0.40	0.43	0.43	0.49	0.48	0.44	0.44	0.39	0.39	0.40
4	from 0.28 to 0.53	positive polarity of pulse current									
		0.30	0.28	0.29	0.37	0.37	0.37	0.35	0.29	0.29	0.28
		negative polarity of pulse current									
		0.30	0.28	0.29	0.37	0.37	0.37	0.35	0.29	0.29	0.28

Oscillograms of the current I_P for several frequencies f_0 from their above range are presented in Fig. 22-24.

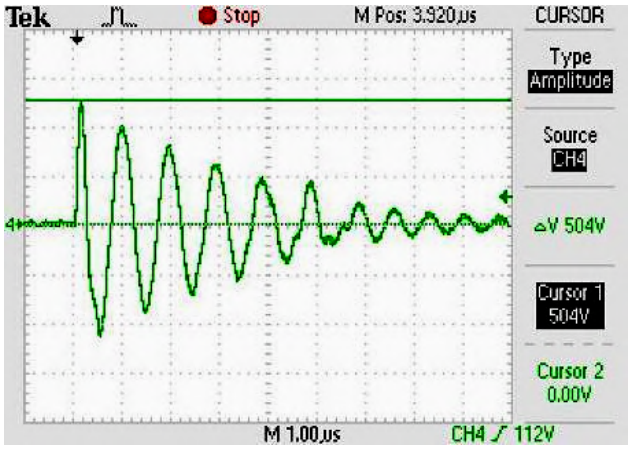

a

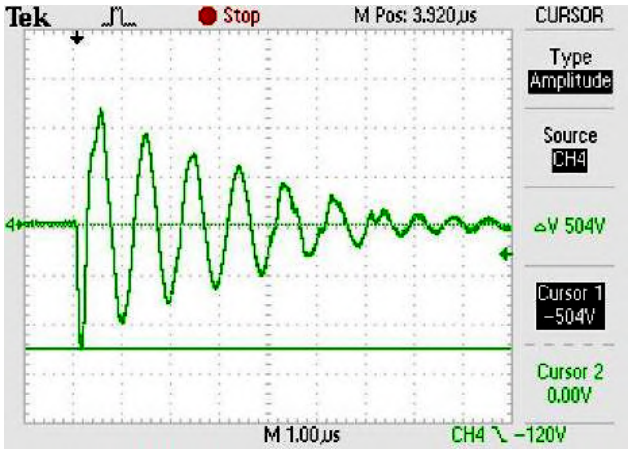

b

Fig. 22. Typical oscillograms of a test pulse current of the form CS116 with frequency f_0=1 MHz and amplitude of 10 A (*a* – positive, *b* – negative polarity)

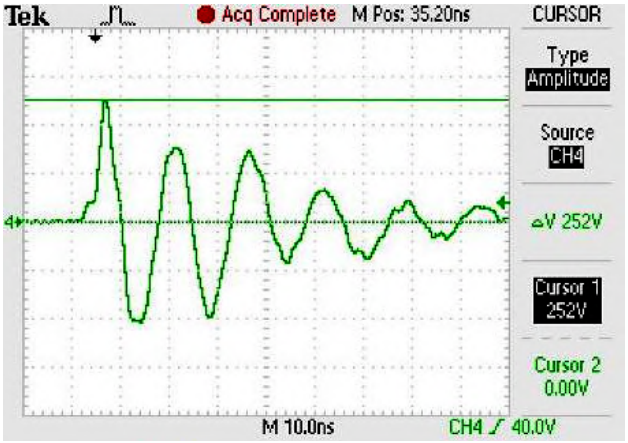

a

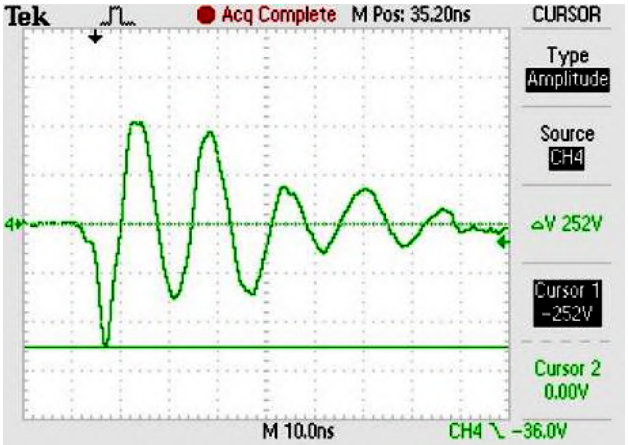

b

Fig. 23. Typical oscillograms of a test pulse current of the form CS116 with frequency f_0=60 MHz and amplitude of 5 A (*a* – positive, *b* – negative polarity)

A comparison of the technical requirements of regulatory documents (RD) according to [7, 9] for the generated current pulses, with the ATPs generated by this electrical installation of current pulses, obtained by us in

the process of verification of test electrical equipment, clearly indicates their full compliance. We point out that today the TI-CS116 (NCS09) high-frequency generator according to ATPs of generated test current pulses also has no foreign analogues.

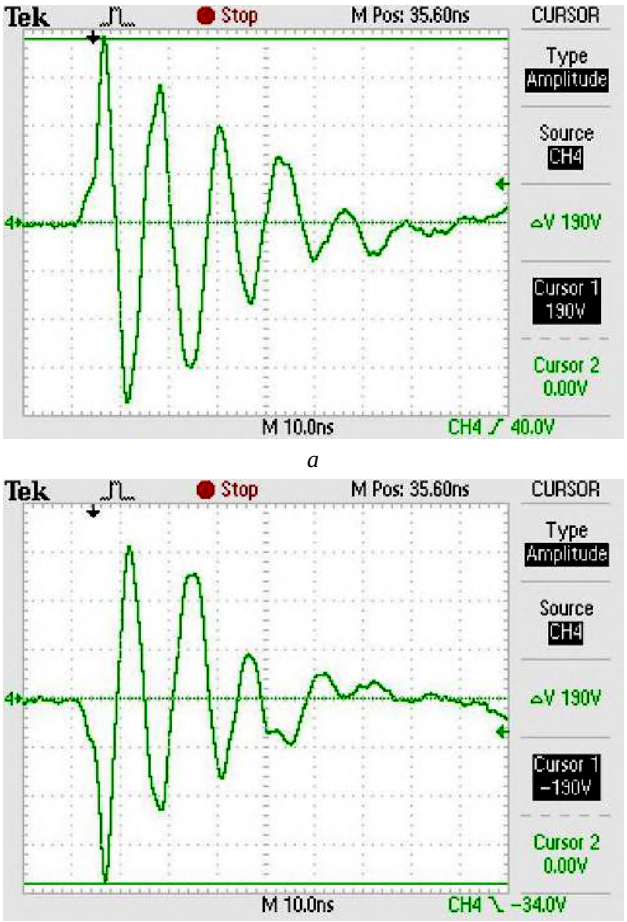

Fig. 24. Typical oscillograms of a test pulse current of the form CS116 with frequency f_0=80 MHz and amplitude of 3.8 A (*a* – positive, *b* – negative polarity)

6. A generator G-NCS10. This current pulse generator is designed to test the components of the OAMT for lightning resistance in the form of NCS10 according to section 3.25 of the NATO Standard AESTR-500: 2016 [7]. A general view of the high-voltage generator G-NCS10 is shown in Fig. 25. This generator allows to generate a powerful aperiodic current pulse of a temporary shape of 50 μs/500 μs at current of up to 10 kA with charge voltage of its capacitor bank up to 2 kV. The G-NCS10 generator differs from the schemes of foreign electrical appliances of a similar class [7] by the original design of its charge-discharge circuits and high specific technical characteristics at the output. Today, this generator has no analogues in foreign countries according to the schemes for constructing its forming electric circuits and has a relatively low cost.

At the Institute, a mathematical model was developed to assess the distribution of the probability of lightning striking the surface of an aircraft. An experimental testing of a computer code for this scientific

Fig. 25. General view of a high-voltage current pulse generator of the G-NCS10 type, which implements the requirements of the NATO AESTR-500: 2016 Standard when testing OAMT in the form of NCS10 (Scientific-&-Research Planning-&-Design Institute «Molniya» of NTU «KhPI», Kharkiv, 2018)

direction was carried out on the model of an A320 airplane. The frames of the process of such high-voltage tests of aircraft using the G-NCS10 generator and other generators are presented in Fig. 26.

Fig. 26. Frames from the process of experimental determination of the likely places of a lightning strike in an airplane model

In the course of these tests, it was found that the recommendations of US documents SAE ARP 5414 [30] and SAE ARP 5416 [14] require clarification due to the difference between streamer-leader processes on real and large-scale TOs. The solution to this problem is important not only for aircrafts, but also for other samples of OAMT.

Table 7 presents a list of the main types of tests that are regulated by the NATO Standard according to [7], and the possibility of their implementation at our Institute, taking into account promising developments, the completion of which is scheduled for the end of 2020.

Table 7

Nomenclature of tests and measurements (sample from Table 501-6, 501-7 of AECTP-500: 2016 Standard [7])

Type of test	Name	Platform type	Degree of implementation
1	2	3	4
NCE01	Conducted Emissions, Power Leads, 30 Hz to 10 kHz	Submarine and Air Force only	Full
NCE02	Conducted Emissions, Power Leads, 10 kHz to 10 MHz	All types	Full
NCE04	Conducted Emissions, Exported Transients on Power Leads	Excluding space	Full
NCE05	Conducted Emissions, Power, Control & Signal Leads, 30 Hz to 150 MHz	Excluding space	Full
NCS01	Conducted Susceptibility, Power Leads, 30 Hz to 150 kHz	All types	Full
NCS02	Conducted Susceptibility, Control & Signal Leads, 20 Hz to 50 kHz	Excluding space	Full
NCS07	Conducted Susceptibility, Bulk Cable Injection, 10 kHz to 200 MHz	All types	Full
NCS08	Conducted Susceptibility, Bulk Cable Injection, Impulse Excitation	Excluding ships and submarines	Full
NCS09	Conducted Susceptibility, Damped Sinusoidal Transients, Cables and Power Leads, 10 kHz to 100 MHz	All types	Full
NCS10	Conducted Susceptibility, Imported Lighting Transients	Air Force only	Full
NCS12	Conducted Susceptibility, Electrostatic Discharge	Ground and Air Force only	Full
NRE01	Radiated Emissions, Magnetic Field, 30 Hz to 100 kHz	Excluding space	Full
NRE02	Radiated Emissions, Electric Field, 10 kHz to 18 GHz	All types	Up to 6 GHz
NRS01	Radiated Susceptibility, Magnetic Field, 30 Hz to 100 kHz	Excluding space	Full
NRS02	Radiated Susceptibility, Electric Field, 50 kHz to 40 GHz	All types	Up to 6 GHz; up to 50 V/m

Note: All types – including surface ships, submarines; ground forces, air force; space systems and launch complexes.

7. An installation for monitoring the state of electrical safety and grounding systems of electric power facilities. When performing this control, the electrical and technological parameters of the GDs of the required energy objects are determined. These parameters include: GD resistance; voltage on the GD; touch voltage and GD design. The analysis by the Institute staff on the results of diagnostics of the GDs of more than 1200 power facilities in Ukraine (including four NPPs, 15 TPPs, 4 HPPs, 100 substations with voltage class of 220-750 kV, 900 substations with voltage class of 35-150 kV, etc.) showed that during SC in the power system, exceeding the permissible value of touch voltage at power facilities is fixed at more than 75 % of substations with voltage class of 110-750 kV. The most widespread in the world practice of monitoring the safe operation of electrical installations and during experimental measurement of touch voltage at power facilities is a method based on the use of the «low current method» followed by reduction of the measured touch voltage in direct proportion to the ratio of the actual SC current to the measuring current at the facility [31, 32]. A method based on the application of direct SC current for these purposes is extremely dangerous both for electrical equipment and for technical personnel serving it.

Today, at the Scientific-&-Research Planning-&-Design Institute «Molniya» of NTU «KhPI», electrical engineering works are successfully carried out aimed at improving the reliability of operation of industrial enterprises, energy facilities and transport infrastructure by developing optimal recommendations for the modernization of their GDs based on electromagnetic diagnostics at power facilities operating in Ukraine. For this purpose, at our Institute in the 1990s, a measuring complex was developed and created for diagnosing the state of GDs of power facilities of the KDZ-1 type, the main technical characteristics of which are given in [33]. In 2019, we created a new MV 1000 device, the characteristics of which (Table 8) correspond to the world level in terms of completeness of covering the requirements of IEC standards in terms of ensuring the safe operation of electrical installations [34]. It allows to determine the resistance of contact joints and GDs; voltage on the GD; step voltage; touch voltage and topology of the location of the GDs in the ground.

Table 8

Instrument specifications of the device type MV 1000

Parameter name	Value
Frequency of generated alternating voltage and current, Hz	57 ± 1; 263 ± 2; 523 ± 3; 993 ± 3
Measuring range of generated alternating voltage, V	from 0.5 to 45
Measuring range of generated alternating current, A	from 0.05 to 8.0
Relative error of voltage (current) measurement, %, no more	± 4

Figure 27 shows a scheme for measuring touch voltage using this installation. According to this scheme, the potential electrode *P* must simulate two human feet.

To do this, they use a special electrode-plate with contact surface of size (25 × 25) cm^2. To create reliable contact of this electrode with the ground, a load weighing at least 25 kg is installed on it. The voltmeter is shunted by a resistor with resistance R_B, which should be equal to the resistance of the human body (as a rule, it is taken equal to about 1000 Ω). The horizontal distance from the place of contact of the human feet to the plate to the metal structure of the object is assumed to be from 0.8 m to 1 m [32].

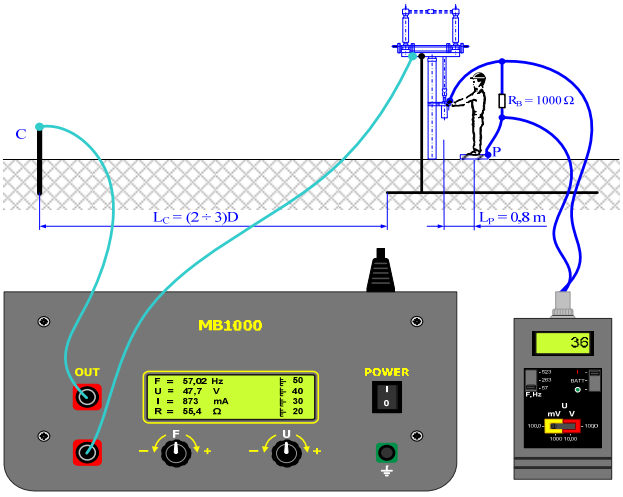

Fig. 27. Touch voltage measurement scheme

The current electrode *C* (see Fig. 27) is located from the place of measuring the touch voltage at a distance equal to (2-3)*D*, where *D* is the diagonal of the GD. Such a distance was accepted for equivalent homogeneous soil according to [31]. The generator is connected to the equipment and electrode *C*, and a voltmeter is connected between the potential electrode and the equipment. To simulate the most adverse seasonal conditions, the installation site of potential electrode *P* is wetted. They lead the measured values of the touch voltage to a real SC current and compare the result with a known acceptable normalized voltage value.

It should be noted that the specified MV 1000 type electrical appliance allows to determine the topology of the GD location without revealing the soil at the place of work on its (this GD) diagnosis (Fig. 28).

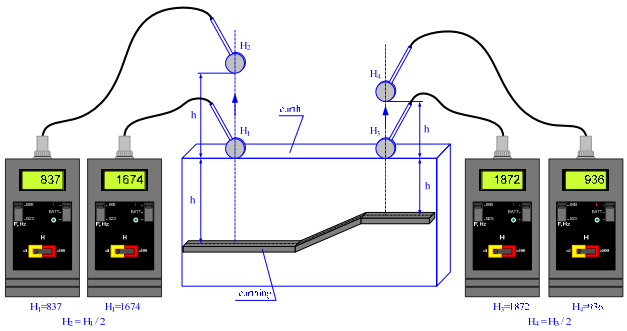

Fig. 28. Scheme for determining the topology of the location of the object's GD using an electrical installation of type MV 1000

Using a new electric device of type MV 1000 for diagnosing the state of the GDs allows:

- increase the accuracy of determining the parameters of the GDs (error – up to 4 %, for analogues – up to 10 %);
- finally move in Ukraine to the European model for determining the normalized parameters of the GDs of power facilities, where the main parameters are touch voltage and step voltage;
- increase the reliability and operation safety of existing domestic power plants (TPPs, NPPs, HPPs) and substations;
- increase the competitiveness of the Scientific-&-Research Planning-&-Design Institute «Molniya» of NTU «KhPI» in Ukraine and enter the European electrical engineering market regarding diagnostics of GDs (the first step to achieve such a commercial goal was the presentation of the MV 1000 device at the International technical exhibition ENERGETAB, Bielsko-Biala, Poland, September 17-19, 2019).

8. An installation for determining the pulse resistance of lightning rods and supports of power lines. In the domestic document [35] there is no concept of pulse resistance of a GD. However, in international requirements, in particular, according to [15, 36], the resistance of the GDs of lightning rods and the supports of overhead power transmission lines (PTLs) is determined at the action on them of a current pulse with specified ATPs as the ratio of the peak voltage value on the GD to the peak value of the current flowing through GD. In the world there are a number of devices that allow to determine the pulse resistance of the GD. A detailed analysis of existing portable devices for this purpose is presented in [37], among which there are Polish WG-407, WG-507 and MRU-200, Japanese PET-7, ZED-meter manufactured in the USA, Ukrainian IK-1U and Russian impedance meter. It should be noted that only three of these devices allow measurements to be made when simulating the impact on power objects of lightning voltage (current) pulses, namely: WG-507 with a voltage (current) pulse of 4/10 μs, MRU-200 with voltage pulses (current) 4/10 μs and 10/350 μs, and IK-1U with voltage pulses (current) of a temporary shape of 1.2/50 μs and 8/20 μs.

In this regard, the staff of the Scientific-&-Research Planning-&-Design Institute «Molniya» of NTU «KhPI» improved the existing measuring complex of the type IK-1U due to «stretching» the duration of the required current pulse 10/350 μs in the mode of generating a current pulse 8/20 μs with a decrease in its amplitude [37]. This was achieved by developing a new forming unit and expanding the measuring range of a pulse voltmeter. In addition, this made it possible to minimize costs by preserving the basic circuitry solutions of the IK-1U generator. The choice of elements for a new set-top box for the device was determined using the *MicroCap* computer code in the *Transient Analysis* mode taking into account the existing values of active and reactive elements. The simulation results of the operation of the IK-1U complex with the forming unit in the 10/350 μs mode (Fig. 29,*a*,*b*) show the compliance of the temporal parameters of the current pulse formed in it with a normative document [15].

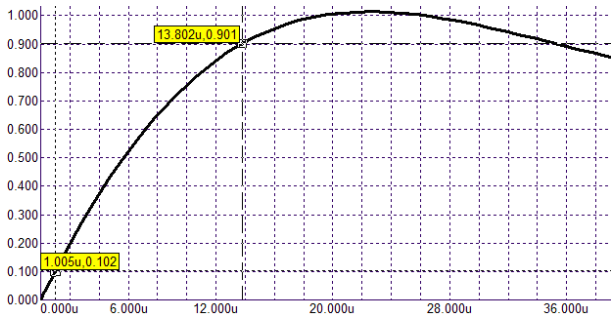

a

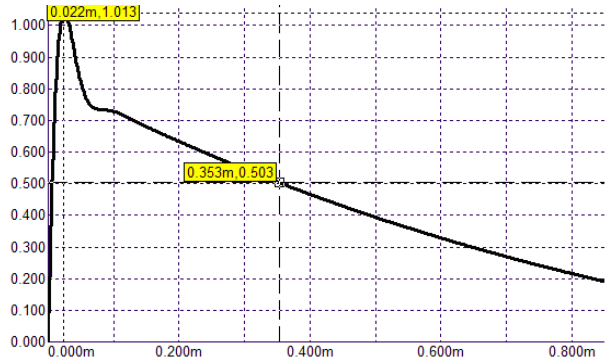

b

Fig. 29. Simulation results for the IK-1U generator of the front of an aperiodic current pulse (*a*) and its duration (*b*) in *MicroCap* code [37]

Based on the results of the simulation, a mock-up of the forming unit for the new device was created in the form of a set-top box to the existing IK-1U complex. Figure 30 shows oscillograms of the front and duration of a thundering aperiodic current pulse of 10/350 μs obtained in IK-1U [37].

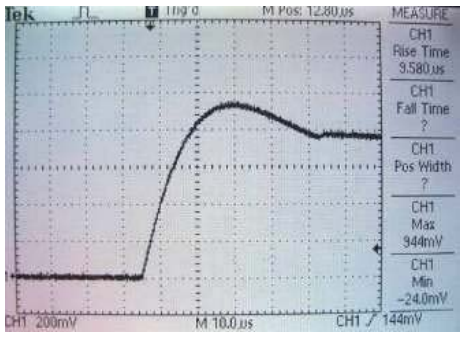

a

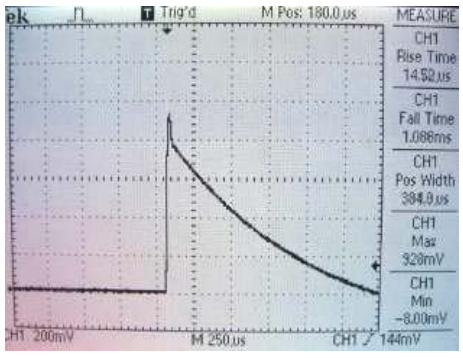

b

Fig. 30. Oscillograms of the front of the current pulse (*a*) and its duration (*b*) in the mode of formation of the temporary shape 10/350 μs by the modernized IK-1U complex [37]

Table 9 shows the main technical characteristics of the advanced measuring complex IK-1U with a new forming unit. After modernization, the IK-1U electrical installation allows the electrical diagnostics of the GD and PTL supports to be performed using three temporary shapes of voltage (current) pulses (1.2/50 μs, 8/20 μs and 10/350 μs), which significantly distinguishes it from foreign analogues [37] .

Table 9

Technical characteristics of the complex IK-1U [37]

Parameter name	Value
Fronts of voltage and current pulses (at levels of 0.1–0.9 from its amplitude), μs	1.2 ± 0.1; 8 ± 0.8; 10 ± 2.0
Duration of voltage and current pulses (at the level of 0.5 of their amplitude), μs	50 ± 5; 20 ± 4; 350 ± 35
Maximum amplitude of voltage pulses generated for the shapes 1.2/50 μs and 8/20 μs (in the 10/350 μs mode), V	1000 (600)
Range of measurements of the amplitude of voltage pulses, V	from 0.5 to 200
Maximum amplitude of current pulses generated for the shapes 1.2/50 μs and 8/20 μs (in the 10/350 μs mode), A	25 ± 5 (1 ± 0.05)
Range of measurements of the amplitude of current pulses, A	from 0.1 to 25
Relative error of voltage (current) measurement %, no more	10

The modernized complex IK-1U successfully passed testing when performing electromagnetic diagnostics of the state of the GDs at more than 100 operating electrical substations in Ukraine.

9. Electric drive and field characteristics to solve the problems of ensuring its EMC. A new scientific and technical direction was developed at the Institute related to the development and research of electric drives based on linear motors (LMs) of electromagnetic and inductor types, as well as switched reluctance machines (SRMs) [38, 39]. In the practical application of such LDs and SRMs as part of electric drives of various devices and systems, one of the most important tasks is to ensure their EMC. In this regard, work on the study of transient electromagnetic processes and calculation of magnetic fields in LDs and SRMs has come to the fore. For mathematical modelling of these electromechanical systems, we have applied:

- modelling based on the solution of differential equations of electrical phase circuits;
- modelling based on the well-known circuit-field mathematical models of LDs and SRMs;
- modelling based on the approach of a generalized electromechanical energy converter.

When determining the field characteristics of LDs of electromagnetic and inductor types, the staff of the Institute used the well-known Finite Element Method – the basis of the FEMM computer code. The results of these field calculations became a guideline in assessing their EMC as part of a turnout drive for railway transport [39]. The practical application of the results of these studies will allow to develop measures to reduce the level of emission of radio interference generated by the LDs

and bring them into line with the requirements of UN Regulation No. 10.

An inductor-type LD magnetic field was also calculated [39]. The developed mathematical models using the FEMM code became the basis for the calculated assessment of the EMC of this type of LD.

From the above review of domestic powerful high-voltage test electrical equipment designed to solve problems in the field of electrical safety, EMC and the resistance of power facilities, OAMT, AT and SRT to the damaging effects of standard aperiodic lightning current pulses, switching voltage pulses and other special shapes of current pulses (voltage), it follows that the considered individual electrical installations of the Scientific-&-Research Planning-&-Design Institute «Molniya» of NTU «KhPI», which implement the requirements of International and national regulatory documents [4-10, 13-16, 36], are characterized by a relatively low cost in general, a high unification of components and applied materials, the originality of the construction of high-current discharge circuits of their high-voltage current (voltage) generators and their synchronous parallel electrical start circuits.

Conclusions. Designed and created as part of a single electrical complex of the Scientific-&-Research Planning-&-Design Institute «Molniya» of NTU «KhPI» high-voltage test installations of the type UITOM-1, GTM-10/350, GKIN-2, TI-CS115 (NCS08), TI-CS116 (NCS09), G- NCS10, MV 1000 and IK-1U are capable in accordance with the requirements of US regulatory documents SAE ARP 5412: 2013, SAE ARP 5414: 2013, SAE ARP 5416: 2013, RTCA DO-160G: 2011, US military Standards MIL-STD-464C: 2010, MIL-STD-461G: 2015, NATO Standards AECTP-500: 2016, AECTP-250: 2014, International Standards IEC 62305-1: 2010, IEC 61024-1: 1990 and Interstate Standard GOST 1516.2-97 to conduct field tests of objects of industrial energy on electrical safety and resistance to standard aperiodic lightning and switching voltage (current) pulses in order to really determine the stability of their electrical components and the electrical strength of their insulation, as well as weapons and military equipment, aircraft and rocket and space technology to electromagnetic compatibility and resistance when exposed to them in accordance with current international requirements of normalized high-voltage current pulses of artificial lightning, as well as other special temporary shapes of current pulses (voltage).

Acknowledgment. Work on the development and creation of high-voltage test electrical equipment at the Scientific-&-Research Planning-&-Design Institute «Molniya» of NTU «KhPI» was carried out as part of a number of applied scientific and technical projects funded by the Ministry of Education and Science of Ukraine: «Development and research of prototypes of advanced technical means of lightning protection of aerospace equipment» (state registration number 0104U000447); «Development and research of the possibility of creating a powerful electrophysical installation for generating full lightning current and testing of electric power facilities for lightning resistance» (state registration number 0106U012302); «Ensuring energy security of Ukraine by increasing the operation reliability of strategic energy facilities in normal and emergency modes» (state registration number 0117U000534); «Ensuring compliance of armaments and military equipment of Ukraine with modern requirements of NATO Standards on electromagnetic compatibility» (state registration number 0117U000533); «Development of test systems for standard weapons and military equipment of Ukraine according to NATO Standards on electromagnetic compatibility» (state registration number 0119U002571).

REFERENCES

1. Baranov M.I. *Izbrannye voprosy elektrofiziki. Monografiya v 3kh tomakh. Tom 2, Kn. 2: Teoriia elektrofizicheskikh effektov i zadach* [Selected topics of Electrophysics. Monograph in 3 Vols. Vol.2, Book 2. A theory of electrophysical effects and tasks]. Kharkiv, Tochka Publ., 2010. 407 p. (Rus).

2. Baranov M.I. An anthology of the distinguished achievements in science and technique. Part 42: Electronics: retrospective view, successes and prospects of its development. *Electrical engineering & electromechanics*, 2018, no. 1, pp. 3-16. **doi: 10.20998/2074-272X.2018.1.01.**

3. Uman M.A. Natural and artificially-initiated lightning and lightning test standards. *Proceedings of the IEEE*, 1988, vol. 76, no. 12, pp. 1548-1565. **doi: 10.1109/5.16349.**

4. Directive 2014/30/EU of the European parliament and of the Council of 26 February 2014 on the harmonisation of the laws of the Member States relating to electromagnetic compatibility. *Official Journal of the European Union*, 29.03.2014, L96, pp. 79-106.

5. *QR-160D. Qualifying requirements. External and environment environments for a side aviation equipment (Environmental factors – EF). Requirements, norms and methods of tests.* Moscow, ARIAC Publ., 2004. 324 p. (Rus).

6. *DO-160G: 2011. Environmental conditions and test procedures for airborne equipment.* USA, 2011. 438 p.

7. *AECTP-500: 2016. NATO Standard Electromagnetic Environmental Effects Tests and Verification. Edition E Version 1*, December 2016, NSO Publ., 1125 p.

8. *AECTP-250: 2014. NATO Standard Electrical and Electromagnetic Environmental Conditions. Edition C Version 1*, December 2014, NSO Publ., 253 p.

9. *MIL-STD-461G: 2015. Requirements for the control of electromagnetic interference characteristics of subsystems and equipment*. USA, 2015, 280 p.

10. *MIL-STD-464C: 2010. Electromagnetic environmental effects. Requirements for systems.* USA, 2010, 165 p.

11. Bortnik I.M., Beloglovskiy A.A., Vereshchagin I.P., Vershinin Yu.N., Kalinin A.V., Kuchinskiy G.S., Larionov V.P., Monastyrskiy A.E., Orlov A.V., Temnikov A.G., Pintal' Yu.S., Sergeev Yu.G., Sokolova M.V. *Elekrophizicheskie osnovy techniki vysokih naprjazhenij* [Electrophysics bases of technique of high voltage]. Moscow, Publishing house of MEI, 2010. 704 p. (Rus).

12. *GOST 1516.2-97. Elektrooborudovanie i elektroustanovki peremennogo toka na napriazhenie 3 kV i vyshe. Obshchie metody ispytanii elektricheskoi prochnosti izoliatsii* [GOST 1516.2-97. Electrical equipment and installations for AC voltages 3 kV and higher. General methods of dielectric tests]. Minsk, Publishing house of standards, 1998. 31 p. (Rus).

13. SAE ARP 5412: 2013. Aircraft Lightning Environment and Ralated Test Waveforms. SAE Aerospace. USA, 2013, pp. 1-56.

14. SAE ARP 5416: 2013. Aircraft Lightning Test Methods. SAE Aerospace. USA, 2013, pp. 1-145.

15. IEC 62305-1: 2010 «Protection against lightning. Part 1: General principles». Geneva, IEC Publ., 2010.

16. *GOST R MEK 62305-1-2010. Menedzhment riska. Zashhita ot molnii. Chast' 1: Obshhie principy* [GOST R IEC

62305-1-2010. Risk management. Protection from lightning. Part 1: General principles]. Moscow, Standartinform Publ., 2011, 46 p. (Rus).
17. Baranov M.I., Koliushko G.M., Kravchenko V.I., Nedzel'skii O.S., Dnyshchenko V.N. A Current Generator of the Artificial Lightning for Full-Scale Tests of Engineering Objects. *Instruments and Experimental Technique*, 2008, no. 3, pp. 401-405. **doi: 10.1134/s0020441208030123.**
18. Baranov M.I., Buriakovskyi S.G., Hrytsenko A.S., Kostiuk V.A. Results of investigations of thermal resistibility of prototypes of aluminum alloy panels of fuel tank of airplane to direct action of normalized components of artificial lightning current. *Electrical engineering & electromechanics*, 2019, no. 6, pp. 29-38. **doi: 10.20998/2074-272X.2019.6.04.**
19. Baranov M.I., Kniaziev V.V., Rudakov S.V. The coaxial shunt for measurement of current pulses of artificial lightning with the amplitude up to ±220 kA. *Instruments and Experimental Technique*, 2018, vol. 61, no. 4, pp. 501-505. **doi: 10.1134/S0020441218030156**
20. Baranov M.I., Buriakovskyi S.G., Rudakov S.V. The tooling in Ukraine of model tests of objects of energy, aviation and space-rocket engineering on resistibility to action of pulsed current of artificial lightning. *Electrical engineering & electromechanics*, 2018, no. 4, pp. 45-53. **doi: 10.20998/2074-272X.2018.4.08**.
21. Baranov M.I., Koliushko G.M., Kravchenko V.I., Rudakov S.V. A generator aperiodic current pulses of artificial lightning with a rationed temporal form of 10/350 μs with an amplitude of ±(100-200) kA. *Instruments and Experimental Techniques*, 2015, vol. 58, no. 6, pp. 745-750. **doi: 10.1134/S0020441215060032.**
22. Baranov M.I., Koliushko G.M., Kravchenko V.I., Rudakov S.V. A powerful high-voltage generator of aperiodic impulses of current of artificial lightning with the peak-temporal parameters rated on an international standard IEC 62305-1-2010. *Electrical Engineering & Electromechanics*, 2015, no. 1, pp. 51-56. **doi: 10.20998/2074-272X.2015.1.10.**
23. Baranov M.I., Rudakov S.V. Electrothermal action of the pulse of the current of a short artificial-lightning stroke on test specimens of wires and cables of electric power objects. *Journal of Engineering Physics and Thermophysics*, 2018, vol. 91, no. 2, pp. 544-555. **doi: 10.1007/s10891-018-1775-2.**
24. Baranov M.I., Koliushko G.M., Kravchenko V.I. A switching aperiodic superhigh-voltage pulse generator for testing the electric strength of insulation of technical objects. *Instruments and Experimental Technique*, 2013, vol. 56, no. 6, pp. 653-658. **doi: 10.1134/s0020441213050126.**
25. Pekar' I.R., Fertik S.M. The powerful high-voltage electric-discharge setting on 4 MV and 1 MJ. *Lecture collection of interinstitute conference «Electrophysics apparatus and electric isolation»*. Moscow, Energiya Publ., 1970, pp. 22-26. (Rus).
26. Beier M., Bek V., Meller K., Tsaengl V. *Tekhnika vysokikh napriazhenii: teoreticheskie i prakticheskie osnovy primeneniia* [Technics of high voltages. Theoretical and practical application bases]. Moscow, Energoatomizdat Publ., 1989. 555 p. (Rus).
27. Baranov M.I. *Izbrannye voprosy elektrofiziki: Monografija v 4-h tomah. Tom 1: Elektrofizika i vydajushhiesja fiziki mira* [Selected topics electrophysics: Monographs in 4 vols. Vol.1: Electrophysics and outstanding physics of the world]. Kharkov, NTU «KhPI» Publ., 2008. 252 p. (Rus).
28. Baranov M.I., Bocharov V.A., Zyabko Yu.P. Complex high-voltage electrophysical equipment for testing lightning protection of technical objects via storm and switching micro and millisecond voltage impulses with up to 1 MV amplitude. *Electrical engineering & electromechanics*, 2006, no. 4, pp. 60-65. (Rus).
29. Baranov M.I., Koliushko G.M., Kravchenko V.I. Generation of standard switching aperiodic impulses of high and superhigh voltage for full-scale tests of electrical power objects. *Electrical engineering & electromechanics*, 2013, no. 2, pp. 52-56. (Rus).
30. SAE ARP 5414: 2013. Aircraft Lightning Zoning. SAE Aerospace. USA, 2013, pp. 1-33.
31. *IEEE Std 80-2000 Guide for Safety in AC Substation Grounding*. New York, IEEE, 2000. 200 p. **doi: 10.1109/ieeestd.2000.91902**.
32. Koliushko D.G., Rudenko S.S. Analysis of methods for monitoring of existing energy objects grounding devices state at the present stage. *Electrical engineering & electromechanics*, 2019, no. 1, pp. 67-72. **doi: 10.20998/2074-272X.2019.1.11.**
33. Djura D.A., Selivanov V.N. Instruments to measure impulse response of grounding. *Trudy Kolskogo nauchnogo tsentra RAN*, 2013, no. 4, pp. 56-66. (Rus).
34. Glebov O.Yu., Koliushko G.M, Koliushko D.G., Plichko A.V., Ponudzhayeva O.G. *Prystrii dlia diahnostyky stanu zazemliuvalnoho prystroiu enerhoobiektiv* [Device for diagnostics of grounding system of energy objects]. Patent UA, no. 136575, 2019. (Ukr).
35. *Pravila ulashtuvannya electroustanovok* [Electrical installation regulations]. Kharkiv, Fort Publ., 2017. 760 p. (Ukr).
36. *IEC 61024-1: 1990. Protection of structures against lightning. Part 1: General principles*. Geneva, IEC Publ., 1990, 47 p.
37. Koliushko D.G., Rudenko S.S., Plichko A.V., Shcherbinin V.I. Modernization of the complex type IK-1U for measuring the impedance of the grounding device of a lightning arrester and supports of transmission lines. *Electrical engineering & electromechanics*, 2019, no. 3, pp. 55-58. **doi: 10.20998/2074-272X.2019.3.09.**
38. Buryakovskiy S.G., Lyubarskiy B.G., Masliy Ar.S., Masliy An.S. Calculation of hauling description of linear engine for a pointer translation. *Information and control systems at railway transport*, 2015, no. 1(110), pp. 83-87. (Rus).
39. Buriakovskyi S., Maslii A., Maslii A. Determining parameters of electric drive of a sleeper-type turnout based on electromagnet and linear inductor electric motor. *Eastern-European Journal of Enterprise Technologies*, 2016, vol. 4, no. 1(82), pp. 32-41. (Rus). **doi: 10.15587/1729-4061.2016.75860**.

Received 12.02.2020

M.I. Baranov[1], *Doctor of Technical Science, Professor,*
S.G. Buriakovskyi[1], *Doctor of Technical Science, Professor,*
V.V. Kniaziev[1], *Candidate of Technical Science, Leader Research Scientist,*
S.S. Rudenko[1], *Candidate of Technical Science, Senior Research Scientist,*
[1] Scientific-&-Research Planning-&-Design Institute «Molniya», National Technical University «Kharkiv Polytechnic Institute», 47, Shevchenko Str., Kharkiv, 61013, Ukraine,
phone +380 57 7076841,
e-mail: baranovmi@kpi.kharkov.ua, sergbyr@i.ua, knyaz2@i.ua, nio5_molniya@ukr.net

How to cite this article:
Baranov M.I., Buriakovskyi S.G., Kniaziev V.V., Rudenko S.S. Analysis of characteristics and possibilities of high-voltage electrical engineering complex Scientific-&-Research Planning-&-Design Institute «Molniya» of NTU «KhPI» for the tests of objects of energy, armament, aviation and space-rocket technique on electric safety and electromagnetic compatibility. *Electrical engineering & electromechanics*, 2020, no. 4, pp. 37-53. **doi: 10.20998/2074-272X.2020.4.06.**

UDC 621.319 **doi: 10.20998/2074-272X.2020.4.07**

G.V. Bezprozvannych, O.A. Pushkar

INCREASING NOISE IMMUNITY OF CABLES FOR FIRE PROTECTION SYSTEMS

Introduction. Technical means of fire protection systems are capable of operating at data rates from tens to hundreds of Kbit/s with components of a digital signal in the frequency spectrum up to several tens of MHz. Appropriate cable infrastructure with a high level of noise immunity is required to transmit broadband digital signals. Purpose. Substantiation of ways to increase noise immunity of cables based on twisted pairs for modern fire protection systems with the ability to transmit digital signals in the frequency spectrum up to 100 MHz. Methodology. A comparison is made of the influence of the twisting step of pairs in unshielded 4-pair and multi-pair shielded balanced cables on the parameters of electromagnetic effects. It has been experimentally shown that twisting each pair with different steps provides a higher level of noise immunity of cables based on twisted pairs. Practical value. The frequency dependencies of the near end crosstalk in 10-, 30- and 4-pair balanced cables are shown. The influence of the common shield on the attenuation coefficient of the shielded 4-pair cable is established. References 12, figures 8.

Key words: **fire protection systems, electromagnetic influence, near end crosstalk, twisted pairs, unshielded and shielded cables, attenuation coefficient.**

Наведено частотні залежності перехідного загасання на ближньому кінці в 10, 30 та 4-х парних симетричних кабелях. Експериментально доведено, що скручування кожної пари з різними кроками забезпечує більш високий рівень завадостійкості кабелів на основі витих пар. Застосування загального екрану призводить до зменшення електромагнітних впливів між витими парами кабелю. Діапазон значень перехідного затухання на ближньому кінці на верхній робочій частоті 100 МГц становить 44-54 дБ та 46-58 дБ для неекранованого та екранованого кабелів з витими парами відповідно. Ефект зростання коефіцієнту загасання та більший розкид параметрів впливу обумовлює більш жорсткі вимоги до щільності конструкції та налаштувань технологічного процесу виготовлення екранованих кабелів. Бібл. 12, рис. 8.

Ключові слова: **системи протипожежного захисту, електромагнітний вплив, перехідне загасання на ближньому кінці, кручені пари, неекранований і екранований кабелі, коефіцієнт загасання.**

Приведены частотные зависимости переходного затухания на ближнем конце в 10, 30 и 4-х парных симметричных кабелях. Экспериментально показано, что скрутка каждой пары с разными шагами обеспечивает более высокий уровень помехоустойчивости кабелей на основе витых пар. Применение общего экрана приводит к уменьшению электромагнитных влияний между витыми парами кабеля. Диапазон значений переходного затухания на ближнем конце на верхней рабочей частоте 100 МГц составляет 44-54 дБ и 46-58 дБ для неэкранированного и экранированного кабелей с витыми парами соответственно. Эффект роста коэффициента затухания и больший разброс параметров влияния обусловливают более жесткие требования к плотности конструкции и настройкам технологического процесса изготовления экранированных кабелей. Библ. 12, рис. 8.

Ключевые слова: **системы противопожарной защиты, электромагнитное влияние, переходное затухание на ближнем конце, витые пары, неэкранированный и экранированный кабели, коэффициент затухания.**

Introduction. Fire protection and fire alarm systems have expanded from fairly simple electromechanical devices to modern microprocessor technologies that are highly sensitive to electromagnetic interference. Regardless of the devices used, fire protection systems use different interfaces of communication devices. Modern technical means of such systems are able to operate at data rates from tens to hundreds of kBit/s with components of the digital signal in the frequency spectrum up to several tens of MHz. For the transmission of broadband digital signals an appropriate cable infrastructure which should provide high requirements for noise immunity when transmitting signals over cables is required [1, 2]. The basis of such infrastructure is modern symmetrical cables based on twisted pairs [1, 2]. Twisting of conductors in pairs is carried out in order to increase the degree of communication between the conductors of one pair and further reduce electromagnetic interference from external sources, as well as mutual inducing in the transmission of differential signals [3, 4].

Category 5e cables with copper conductors are widely used in fire protection systems, structured cable systems [3, 4] and provide digital signals transmission in the frequency spectrum up to 100 MHz [5].

As the transmission speed increases, along with the need to provide digital signals, the interference increases, both inside and outside the cable [5, 6]. Reducing the level of electromagnetic interference is achieved due to the principle of balanced signal transmission over a pair of twisted wires [5, 6].

For a symmetric (balanced) pair, the property of symmetry is fundamentally important, i.e. the same physical and electrical properties of forward and reverse conductors. Otherwise, the currents and voltages of the interference that occur in the pair increase significantly. The essence of symmetry is that the induced currents and voltages have almost the same amplitude and opposite phases, i.e. compensate each other. A number of important cable parameters are related to the mechanism of interaction between pairs. Transient interference is the main source of noise which reduces the quality of signal transmission over the cable. The urgency of this problem is constantly growing, because the transient interference increases with increasing signal transmission rate, and hence the frequency [5, 6].

Problem definition. To characterize the noise immunity of cables, the parameters of mutual influence

© G.V. Bezprozvannych, O.A. Pushkar

are used, in particular, transient attenuation at the near end (NEXT – Near End CrossTalk) [5, 6]. The influence parameters characterize the part of the electromagnetic energy of the signal which is converted into electromagnetic radiation. The transition of electromagnetic energy from one pair to another one is associated with the electromagnetic interaction between cable pairs [5-8].

The NEXT parameter depends on the cable design: the number of pairs (Fig. 1), twisting steps, fluctuations in the geometric dimensions of the conductive cores and the insulation thickness relative to the normalized values within the tolerances [8-11].

Figure 1 shows the transient attenuation at the near end in the form of level lines in 30-pair (Fig. 1,*a*) and 10-pair (Fig. 1,*b*) shielded symmetrical cables of the same length at frequency of 256 kHz: *Nv* is the pair that affects (source of interference); *Np* is the pair that is affected (interference receiver).

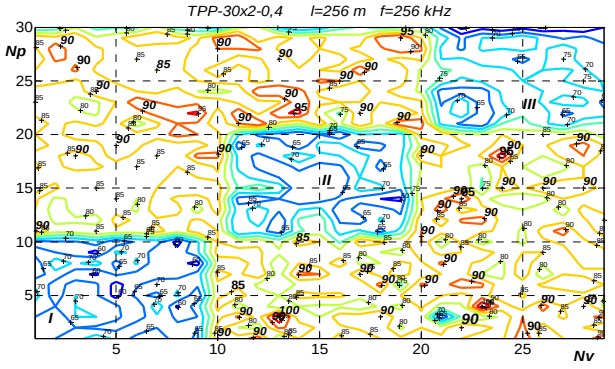

a

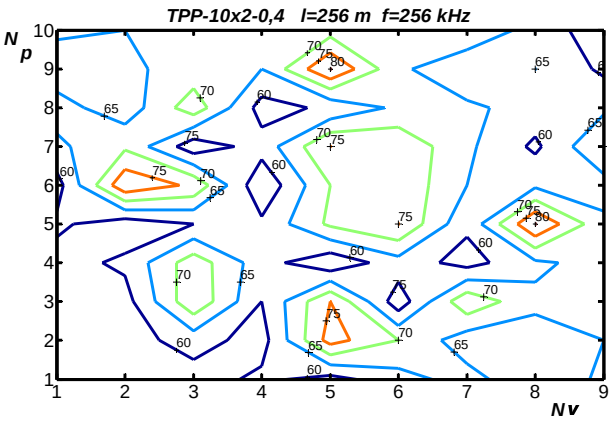

b

Fig. 1. Influence of design of symmetrical cables on transient attenuation at the near end

For the 30-pair cable, the impact parameters are clearly divided into three groups (denoted by the numbers ***I***, ***II***, ***III***) (Fig. 1,*a*), within which the transient attenuation at the near end for pairs located nearby is the smallest and is 65 dB, i.e. mutual influences are the greatest. For pairs from different groups (the most distant) the transient attenuation is quite high: up to 90 and even 100 dB.

For 10-pairs cable (Fig. 1,*b*) the impact parameters are higher. The lowest value of the transient attenuation is 60 dB (for example, between pairs 5–1 and 8–7); the highest one is 80 dB (between pairs 5–9).

The reason for this is that in such a cable the pairs are located close to each other. The twisting step in 5 pairs is one, the same for these pairs, in the other 5 pairs is the other (coordinated), but also the same for these 5 pairs.

As the frequency increases, the transient attenuation at the near end decreases (Fig. 2), i.e. the level of interference increases.

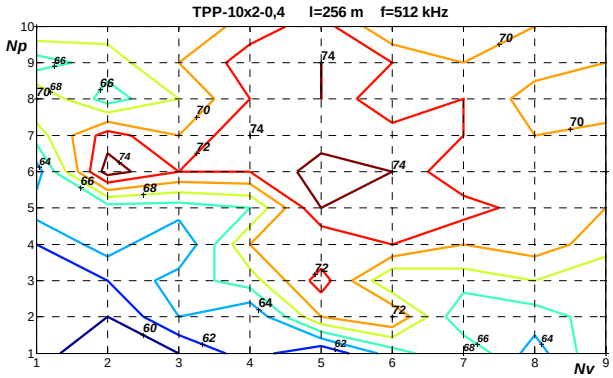

a – frequency 512 kHz

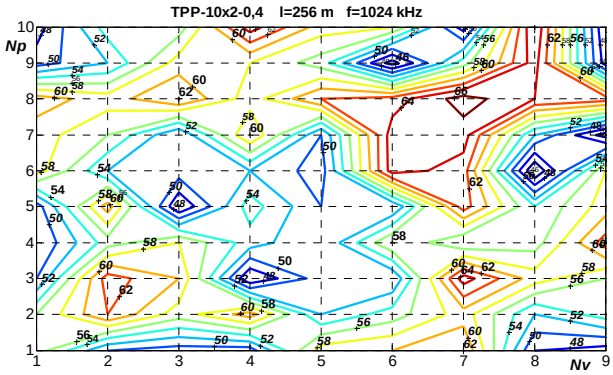

b – frequency 1024 kHz

Fig. 2. Dynamics of change of transient attenuation at the near end on frequency in a multipaired symmetric cable

The goal of the paper is to substantiate ways to increase the noise immunity of twisted pair cables for modern fire protection systems with the ability to transmit digital signals in the frequency spectrum up to 100 MHz.

Influence of cable twisting step on transient attenuation at the near end. To reduce the electromagnetic influence in the high-frequency range between pairs in the cable, it is necessary to twist pairs of conductors with different coordinated steps [8]

$$\frac{h_i}{h_j} = \frac{2v \pm 1}{2w}, \qquad (1)$$

where h_i, h_j are the steps of twisting pairs, v and w are the positive integers.

When twisting pairs in a cable of ideal design while ensuring the stability of the twisting step along the entire length, the electrical and magnetic components of the impact change their sign to the opposite with their constant value modulo.

The transient attenuation at the near end in this case noticeably increases (curve 3, Fig. 3) and consists of transient attenuation between non-twisted pairs (curve 1)

and additional transient attenuation due to twisting of pair's conductors (curve 2, Fig. 3).

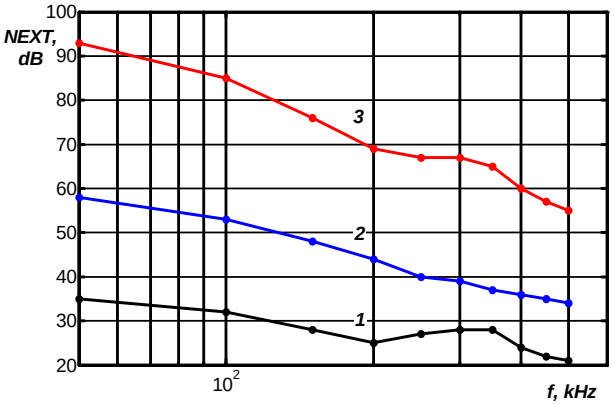

Fig. 3. Influence of twisting of conductors on transient attenuation at the near end in a symmetrical pair

The transient attenuation for twisted pairs is greater the smaller the twist step

$$NEXT = 20\lg\left|\pi(h_i/h_j+1)/\gamma_i h_i\,[1+\kappa(h_i/hj+1)/(h_i/h_j-1)]\right|,$$

where γ_j is the coefficient of propagation of the electromagnetic wave (signal) in the pair with the smallest step, in which the transient attenuation is determined, k = 0.2-0.8 is the coefficient depending on the design of the cable and the location of the pairs.

In a cable consisting of N twisted pairs, the total number of combinations of circuits N_v influencing on each other is [8]

$$N_v = 2\sum_{n=1}^{N-1}(N-n)\,. \qquad (2)$$

Thus, in an unshielded cable with 4 unshielded pairs, the total number of influencing circuits is 12, and 6 of them are inverse: their influence is identical to the direct influence. The number of influencing circuits will be 6 (Fig. 4). In this case, the cable has 6 values of transient attenuation at the near end (Fig. 5). In the 30-pair cable (Fig. 1,*a*) – 435, in the 10-pair one (Fig. 1,*b*) – 45.

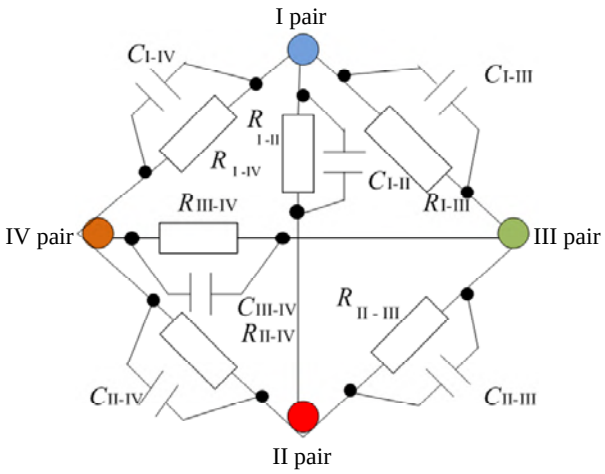

Fig. 4. Capacitive ($C_{I\text{-}II}$, $C_{I\text{-}III}$, $C_{I\text{-}IV}$, $C_{II\text{-}III}$, $C_{II\text{-}IV}$, $C_{II\text{-}IV}$) and active ($R_{I\text{-}II}$, $R_{I\text{-}III}$, $R_{I\text{-}IV}$, $R_{II\text{-}III}$, $R_{II\text{-}IV}$, $R_{II\text{-}IV}$) components of electromagnetic influences in a 4-pair unshielded cable

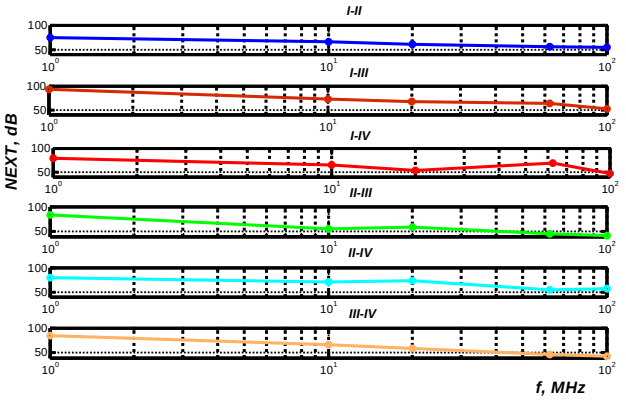

Fig. 5. Experimental frequency dependencies of transient attenuation at the near end in a 4-pair unshielded cable with length of 100 m

Twisting each pair with different coordinated steps provides a higher level of transient attenuation at the near end between pairs in a 4-pair unshielded cable compared to a shielded symmetrical 10-pair cable (compare NEXT values for 1 MHz in Fig. 6 and Fig. 2,*b*). The twist step in twisted-pair cables is in the range of 10 to 25 mm, which is at least 10 times less than in multi-pair symmetrical cables [8].

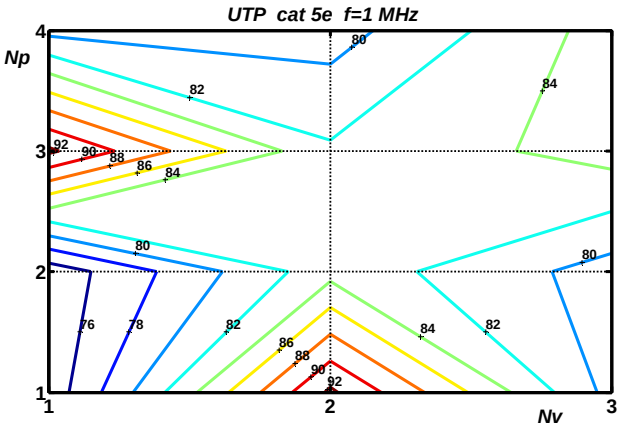

Fig. 6. Transient attenuation level lines at the near end in an unshielded 4-pair cable at 1 MHz

Comparing the values of transient attenuation at the same frequency of two cables of different lengths is quite correct. For a long line in the high frequency range

$$\alpha \cdot l > 6{,}5\ dB\,,$$

(where α is the attenuation coefficient of the signal when propagated in the cable (dB/m) of length l (m)), the transient attenuation at the near end does not practically depend on the length of the line (cable), but depends only on the frequency [8]. This is due to the fact that the interference currents from individual sections come to the near end of the interference receiver so weak that they do not increase the mutual interaction between the pairs.

Shielding efficiency and the effect of the shield on the cable attenuation factor. To increase the transient attenuation, reduce the level of intrinsic electromagnetic radiation of each twisted pair and increase the noise immunity of the cable, depending on the operating conditions, the shielding is used [5, 10, 12]:

- general shielding of 4 twisted pairs;
- individual shielding of each pair without general shielding of all 4 pairs;
- individual shielding of each pair with general shielding of all 4 pairs.

The most common cable design is one with a common shield for 4 twisted pairs [5, 10] for the operating frequency range of 100 MHz. External shields, superimposed on the core of 4 pairs longitudinally, are made of thin polymer film metallized with aluminum (aluminum-polyethylene). A tinned copper or galvanized drainage conductor with diameter of 0.5 mm is introduced into the film shield, which ensures electrical continuity of the shield in case of accidental rupture of the metal film shield during laying, installation and operation of the cable. This shield provides reliable shielding from the magnetic component of the electromagnetic interference. This interference is manifested in the high frequency range. It is possible to use an additional shield in the form of a braid, which protects the cable pairs from electrical interference, which is manifested in the lower frequency range. The use of two-layer shields provides reliable shielding over the entire operating frequency range of the cable [5].

Shielding leads to an increase in cable noise immunity, which is confirmed by the results of measurements of transient attenuation at the near end of unshielded (Fig. 7,*a*) and shielded (Fig. 7,*b*) cables of the same length of 100 m for 100 MHz.

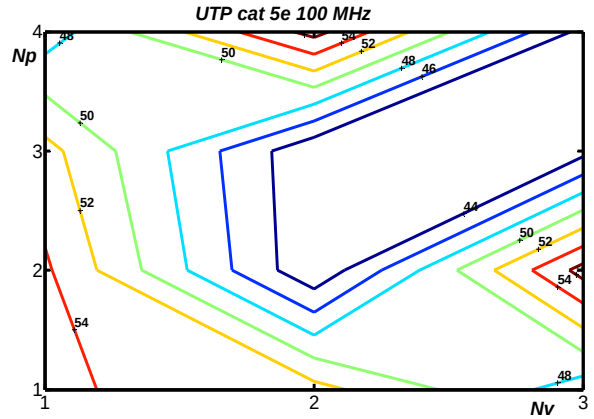

a

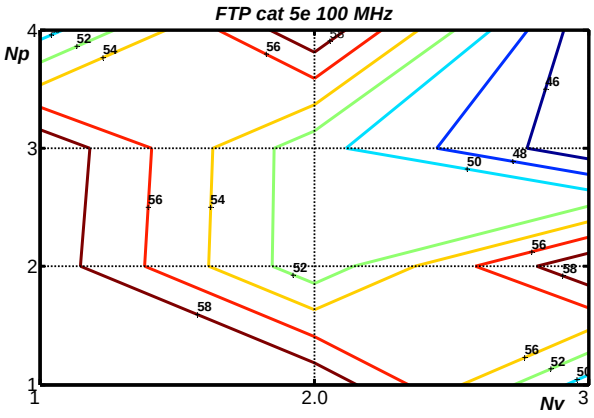

b

Fig. 7. Efficiency of shielding of cables on the basis of twisted pairs in the high-frequency range

Besides, the presence of a shield in the cable design affects the primary transmission parameters: active resistance R of pair's conductors, operating capacitance C, inductance L, active insulation conductivity G and, as a consequence, the secondary transmission parameters: impedance Z and attenuation coefficient α (see formula (3), Fig. 8) with the same conductor diameters, insulation thickness and tolerances as in unshielded cable [10, 11].

$$\alpha = 8{,}69 \cdot \left(\frac{R}{2} \cdot \sqrt{\frac{C}{L}} + \frac{G}{2} \cdot \sqrt{\frac{L}{C}} \right), \text{ dB/m.} \qquad (3)$$

Increase of the attenuation coefficient of 4 twisted pairs of shielded cable (Fig. 8, curve 3) in comparison with unshielded one (Fig. 8, curve 2) in the whole range of operating frequencies, due to higher values of resistance of pair's conductors and operation capacitance due to the proximity effect of the shield, reduces the tolerance relative to the upper limit of the values of the attenuation factor (Fig. 8, curve 1) in the operation of cables.

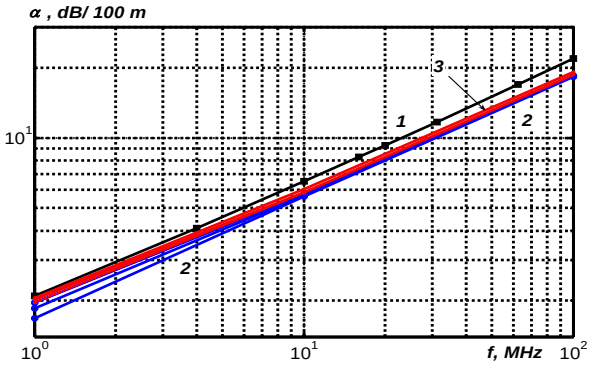

a

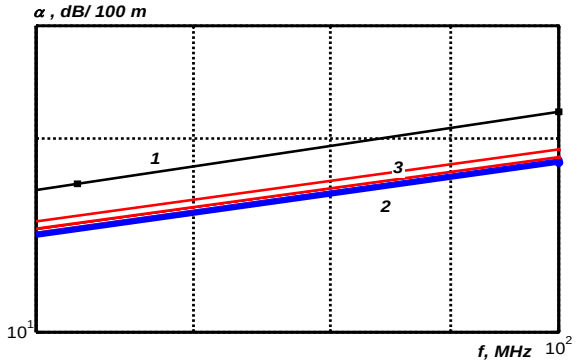

b

Fig. 8. On the effect of shielding on the attenuation factor in the operating frequency range of cables based on twisted pairs

The use of cables with shields requires mandatory and high-quality grounding. In case of unreliable grounding, the interference currents will repeatedly flow through the shield partially reflecting at its ends and emitting electromagnetic waves into space. In this case, the shield becomes a secondary source of radiation – a kind of antenna [5, 6, 12]. In this case, not only will the protection of twisted pair from external sources will be ineffective, but the electromagnetic effect of the cable on other adjacent cables and various electronic devices located in the same room of the fire protection system will be significantly increased.

Conclusions.

It is experimentally proven that the twisting of each pair with different coordinated steps provides a higher level of noise immunity in a 4-pair unshielded cable compared to a shielded symmetrical multi-pair cable at the same frequency.

The use of a general shield reduces the electromagnetic effects between the twisted pairs of cable. The range of transient attenuation values at the near end at the upper operating frequency of 100 MHz is 44-54 dB and 46-58 dB for unshielded and shielded twisted pair cables with the same twisting steps.

The effect of increasing the attenuation coefficient and the greater scatter of the impact parameters cause more stringent requirements for the density of the structure and settings of the technological process of manufacturing shielded cables with twisted pairs.

REFERENCES

1. Pigan R., Metter M. *Automating with PROFINET: Industrial Communication Based on Industrial Ethernet*. John Wiley & Sons Publ., 2015. 462 p.

2. Belous A., Saladukha V. *High-Speed Digital System Design: Art, Science and Experience*. Springer Nature Publ., 2019. 933 p.

3. *Catalog Nexans. Cables for alarm and safety systems*. 2018. 16 p.

4. *International Standard ISO/IEC 11801. Information Technology – Generic cabling for customer premises. Part 2: Office premises*. 2017. 24 p**.**

5. Penttinen Jyrki T.J. *The Telecommunications Handbook: Engineering Guidelines for Fixed, Mobile and Satellite Systems*. John Wiley & Sons Publ., 2015. 1008 p.

6. Weston David A. *Electromagnetic Compatibility: Methods, Analysis, Circuits, and Measurement*. CRC Press, 3rd Edition, 2016. 1160 p.

7. Solak V., Efendioglu H.S., Colak B., Garip M. Analysis and simulation of cable crosstalk. *IEEE IV International Electromagnetic Compatibility Conference (EMC Turkey)*, 24-27 Sept. 2017, Ankara, Turkey, pp 1-4. **doi: 10.1109/EMCT.2017.8090354.**

8. Bezprozvannych G.V., Ignatenko A.G. The influence of core twisting on the transmission parameters of network cables. *Bulletin of NTU «KhPI»*, 2004, no.7, pp. 82-87. (Rus).

9. Bezprozvannych G.V., Ignatenko A.G. Optimization of the design of network cables by the attenuation coefficient in the tolerance zone of the geometric dimensions of the transmission parameters. *Electrical engineering & electromechanics*, 2004, no. 2. pp. 8-10. (Rus).

10. Boyko AM, Bezprozvannych G.V. Justification of insulation thickness of twisted shielded pairs of structured cable systems. *Bulletin of NTU «KhPI»*, 2011, no. 3, pp. 21-35. (Ukr).

11. Bezprozvannych G.V., Ignatenko A.G. Indirect estimates of tolerances on the diameters of conductive conductors of twisted pair conductors of network cables. *Bulletin of NTU «KhPI»*, 2005, no. 42, pp. 47-52. (Rus).

12. Baltag O., Rosu G., Rau M.C. Magnetic field of parallel and twisted wire pairs. *2017 10th International Symposium on Advanced Topics in Electrical Engineering (ATEE)*, 2017, pp. 324-329. **doi: 10.1109/atee.2017.7905020.**

Received 22.05.2020

G.V. Bezprozvannych[1], *Doctor of Technical Science, Professor,*
O.A. Pushkar[2], *General Director,*
[1] National Technical University «Kharkiv Polytechnic Institute»,
2, Kyrpychova Str., Kharkiv, 61002, Ukraine,
phone +380 57 707 60 10,
e-mail: bezprozvannych@kpi.kharkov.ua
[2] Company «Alay»,
95 A2, office 202, Otradny Ave., Kyiv, 03061, Ukraine.

How to cite this article:
Bezprozvannych G.V., Pushkar O.A. Increasing noise immunity of cables for fire protection systems. *Electrical engineering & electromechanics*, 2020, no. 4, pp. 54-58. **doi: 10.20998/2074-272X.2020.4.07.**

UDC 621.3 **doi: 10.20998/2074-272X.2020.4.08**

C. Djabali, T. Bouktir

SIMULTANEOUS ALLOCATION OF MULTIPLE DISTRIBUTED GENERATION AND CAPACITORS IN RADIAL NETWORK USING GENETIC-SALP SWARM ALGORITHM

Purpose. In recent years, the problem of allocation of distributed generation and capacitors banks has received special attention from many utilities and researchers. The present paper deals with single and simultaneous placement of dispersed generation and capacitors banks in radial distribution network with different load levels: light, medium and peak using genetic-salp swarm algorithm. The developed genetic-salp swarm algorithm (GA-SSA) hybrid optimization takes the system input variables of radial distribution network to find the optimal solutions to maximize the benefits of their installation with minimum cost to minimize the active and reactive power losses and improve the voltage profile. The validation of the proposed hybrid genetic-salp swarm algorithm was carried out on IEEE 34-bus test systems and real Algerian distributed network of Djanet (far south of Algeria) with 112-bus. The numerical results endorse the ability of the proposed algorithm to achieve a better results with higher accuracy compared to the result obtained by salp swarm algorithm, genetic algorithm, particle swarm optimization and the hybrid particle swarm optimization algorithms. References 27, tables 10, figures 12.

Key words: **genetic algorithm, salp swarm algorithm, real power losses, distributed generation, capacitors**.

Цель. В последние годы задача размещения распределенной генерации и батарей конденсаторов привлекает особое внимание многих организаций и исследователей. В данной работе рассмотрены отдельное и совместное размещение распределенной генерации и батарей конденсаторов в радиальной распределительной сети при различных уровнях нагрузки: слабом, среднем и пиковом с использованием алгоритма генетического роя сальпов (genetic-salp swarm algorithm). Разработанный алгоритм гибридной оптимизации генетического роя сальпов (GA-SSA) использует системные входные переменные радиальной распределительной сети для поиска оптимальных решений с целью максимизации преимуществ их установки с минимальными затратами для минимизации потерь активной и реактивной мощности и улучшения профиля напряжения. Тестирование предложенного алгоритма гибридной оптимизации генетического роя сальпов было проведено на экспериментальных 34-шинных системах IEEE и реальной 112-шиной алжирской распределенной сети Джанета (крайний юг Алжира). Численные результаты подтверждают способность предложенного алгоритма достигать лучших результатов с большей точностью по сравнению с результатом, полученным методом роя сальпов, генетическим алгоритмом, оптимизацией роя частиц и алгоритмами гибридной оптимизации роя частиц. Библ. 27, табл. 10, рис. 12.

Ключевые слова: **генетический алгоритм, алгоритм роя сальпов, реальные потери мощности, распределенная генерация, конденсаторы.**

Introduction. Radial distribution network provides a link between high voltage transmission network and consumer services. The operation and planning studies of a distribution network require a steady state condition of the system for various load demands [1]. Hence, the need for flexibility of power systems is present. Energy savings and environmental impact ave given impetus to the development of distributed generation (DG), expected to play an increasing role in the power system of the future. Because of the penetration of DGs, the use of these sources in distribution networks is increasing throughout the world [2].

In power systems, loss and reliability are two significant points among several factors that can be considered, especially in distribution systems. Actually two of the most important DG profits are loss reduction and reliability improvement [3]. Installation and operation of DG units is one of the regulators politics in recent years to reduce system losses and improve system efficiency [4].

Capacitors have been widely used in distribution systems to achieve different objectives. The most important are: improving the voltage profile and reducing the power loss in the radial distribution system, determining the optimal locations and sizes of capacitors. [5]. DGs and capacitors used alone or simultaneously with optimum installation and proper sizing have an affecting on reducing network loss and improving voltage profile, because the non-optimal location and size of dispersed generation and capacitors can result in an increase in system losses and costs.

The problem of optimal dispersed generation location and sizing is divided into two sub problems, where the optimal location for DG placement is the one and how to select the most suitable size is the second. Many researches were provided in recent years about optimal placement and sizing of the capacitor and DGs using different methaheuristic methods. Researchers have developed many interesting methods and solutions. The differences are about the problem, which is formulated, methodology and assumptions being made. Some of the methods mentioned in [6]. Simultaneous placement of distributed generation (DG) and capacitor is considered in radial distribution network with different load levels in objective to reduce the active and reactive power loss, to reduce the energy loss and improvement of voltage profile. Again, several optimization algorithms have been proposed such as Fuzzy-DE and Fuzzy-MAPSO methods is proposed in [7], firefly algorithm (FA) [8-10], particle swarm algorithm optimization (PSO) [11], discrete particle swarm optimization (DPSO) [12], Grey Wolf Optimizer (GWO) [13], genetic algorithm (GA) [14], cuckoo search algorithm (CSA) [15], gravitational search algorithm (GSA) [16], salp swarm algorithm (SSA) [17], genetic moth swarm algorithm (GMSA) [18] and biogeography-based optimization (BBO) [19].

A new combined algorithm is proposed to evaluate the DG site and size in distribution network. The location of DGs and capacitors banks is obtained by GA and its

© C. Djabali, T. Bouktir

size is optimized by SSA. First the initial population for equipment (DGs and capacitors) size an and location are produced by random, then the load flow was run. Using the given cost function and benefit's was implemented to optimize the size of DGs and capacitors which was calculated by SSA for the known location. In the next step, the new location of DG was calculated.

The results showed that the proposed combined GA-SSA method is better than the GA and SSA in terms of solution quality and number of iterations.

In this paper, DGs and fixed capacitors banks are installed for two scenarios: singly and simultaneously to minimize the required power transmission network, with different load levels (light, medium and peak). Cost of equipment and benefits are included in the objective function. This algorithm is applied to the network IEEE-34 bus test and the Algerian distributed network in Djanet (City in Southern Algeria) with 112-bus.

Problem statement and formulation. The aim of paper is to maximize the installation benefit of DGs and capacitors and minimize active and reactive power losses for operational powers of the installed equipment to have the efficiency of the GA-SSA algorithm. The objective function is given by the following function:

$$F = \max \sum_{i=1}^{N} Benefit(i) - \min \sum_{i=1}^{N} Cost(i), \quad (1)$$

where N is the number of equipment's (DGS and capacitors banks) installed in the radial distribution network,

$$\sum_{i=1}^{N_{DG}} Benefit(i) = BC + BE + BL + BR, \quad (2)$$

where BC – benefit of cost reduction of active power purchased; BE – benefit of energy loss reduction; BL – benefit of power loss reduction; BR – reactive power loss reduction benefit; N_{DG} – the number of distributed generation

$$\sum_{i=1}^{N} Cost(i) = \sum_{i=1}^{N_{DG}} (DG_c(i) + DG_m(i)) + \sum_{i=1}^{N_C} (cap_c(i)), \quad (3)$$

where DG_C – distributed generation installation cost; DG_m – maintenance cost of DGs; cap_c – capacitor installation cost; N_C – the number of capacitors banks.

Mathematical formulation of the total objective function involves more than one objective function to be optimized simultaneously.

It considers capacitor banks installation cost, active power losses of transmission lines and the cost of distributed generation sources.

The power demand is evaluated as

$$BC = \sum_{i=1}^{N_{DG}} BC_B(i), \quad (4)$$

where BC_B is the benefit of cost reduction of active power purchased after DG installation.

The benefit of energy loss reduction is

$$BE = \sum_{i=1}^{N_{DG}} BE_B(i) + \sum_{i=1}^{N_C} BE_A(i), \quad (5)$$

where BE_B and BE_A are the benefit of energy loss reduction after DG installation and capacitor installation, respectively.

The peak power loss reduction is one of the most important effect of capacitor placements in distribution network and can be computed as

$$BL = C_d \cdot (\sum_{i=1}^{N_C} BL_B(i) - \sum_{i=1}^{N_C} BL_A(i)), \quad (6)$$

where BL_B is the peak power loss in feeder before capacitor installation (kW); BL_A is the peak power loss in feeder after capacitor installation (kW); C_d is demand reduction benefit rate ($/MW).

The reduction of reactive power loss benefit can be calculated as

$$BR = C_R(Q_0 - Q_1), \quad (7)$$

where Q_0, Q_1, and C_R, are reactive power loss before installation of equipment (kVar), reactive power loss after installation of equipment (kVar), and worth of reactive power ($/kVar) respectively.

The cost of capacitor installation is given by:

$$cap_c = Cost_{Ci} \cdot n_{Ci}, \quad (8)$$

where $Cost_{Ci}$ is the cost of i-th capacitor, n_{Ci} is the number of i-th capacitor.

The DG installation cost of distributed generation can be formulated as following equation:

$$DG_c = \sum_{i=1}^{N_{DG}} DG_{c,i} \cdot K_{DG}, \quad (10)$$

where K_{DG} is the size of DGs; $DG_{c,i}$ is the installation cost of i-th DGs.

The maintenance cost of distributed generation is formulated as

$$DG_m = \sum_{i=1}^{N_{DG}} DG_{m,i} \cdot K_{DG}, \quad (11)$$

where $DG_{m,i}$ is the maintenance cost of i-th DGs.

Optimal location and sizing of DGs and capacitors. The optimal location and sizing problems of distributed generation and capacitors bank are bi-objective constrained optimization problems that can be formulated as a mono-objective constrained optimization problem. In this paper the algorithm genetic-salp swarm has been developed for solving the problems of optimal location and sizing of distributed generation and capacitors banks in radial distribution network by maximizing the benefits and minimizing the costs of installation for reduce the active and reactive power losses and improve the voltage profile.

Basic concepts of genetic algorithm. Genetic algorithms are based on chromosomes and their natural evolution. In this method, contrary to the analytical methods, try and error, instead of working on an optimal answer, they work on several answers that they call «populations». These methods is based on the selection mechanisms used by nature, according to which the most fit individuals of a population are those that survive, by adapting more easily to the changes that occur in their environment. This technique has high efficiency in the absence of specific information about the problem [21, 22].

The parameters of genetic algorithm are: population size, reproduction probability, crossover probability and mutation probability.

The pseudo code of the GA algorithm is given as follows:

Step 1: Initialize population in random fashion.

Step 2: Evaluate the population by calculating the fitness of the individuals in the population.

Step 3: Perform selection operation.

Step 4: Perform crossover and mutation operation.

Step 5: Perform optimal search.

Step 6: Repeat step 2 – 5 until the GA is run for the predetermined.

Step 7: Select the best chromosome.

Basic concepts of salp swarm algorithm. Salp swarm algorithm (SSA) is a recently created bio-inspired optimization algorithm presented in 2017, introduced by Mirjalili et al. [23]. SSA mimics the swarming behavior of salps in oceans especially the navigation and searching for food sources. The salps are creatures living in seas and oceans. They are similar to jellyfishes in their tissues and movement towards the food sources [24]. Salps are usually found in groups (swarms) called salp chains; each salp chain contains a leader .The algorithm starts with initializing a matrix with a dimension of $n \cdot dim$ representing salps' positions, where n is the number of agents and dim is the number of variables to be designed. After that, each salp position is updated according to instructions received from the leader for swallowing the best food (F). The following equation is used for updating the salps' positions [25]:

$$x_j^1 = \begin{cases} F_j + c_1 + ((u_{b\,j} - l_{b\,j})c_2 + l_{b\,j}), c_2 \geq 0; \\ F_j - c_1 + ((u_{b\,j} - l_{b\,j})c_2 + l_{b\,j}), c_2 \leq 0, \end{cases} \quad (12)$$

where x_j^1 represents the position of the leader's j-th dimension; F_j represents the best solution (i.e., food source) in the j-th, $u_{b\,j}$ and $l_{b\,j}$ are the upper and lower bounds in the j-th dimension respectively; variables c_1 and c_2 are random numbers (c_1 plays a vital role in the performance of SSA, since it is the only parameter that controls the balance between exploration and exploitation).

As can be seen in [12], c_1 is a time varying parameter (depends on the iteration number) that allows high exploration rates at the early stages of the optimization process, while high exploitation rates are allowed in the last stages. The coefficient is a very significant parameter in SSA for the reason that it maintains a balance between exploration and exploitation, and it can be given by:

$$c_1 = 2e^{-\left(\frac{4l}{L}\right)^2}, \quad (13)$$

where l and L are the current iteration and the maximum number of iterations respectively; c_2 is uniform random numbers generated in the period [0, 1].

These variables indicate whether the next position in the j-th dimension will be moved towards the $+\infty$ or $-\infty$ in addition to the step size. Newton's law of motion [14], was used to simulate updating the positions of the followers

$$x_j^1 = \frac{1}{2}\left(x_j^i + x_j^{i-1}\right), \quad (14)$$

where $i \geq 2$ and x_j^i depicts the position of the i-th follower at the j-th dimension.

In SSA, the leader salp moves towards the food source, whereas the followers move towards the leader. The food source position can be changed during the process and then the leader will continue moving towards the new food source position. The steps of this optimization algorithm and its pseudo code are shown in Algorithm 1 below.

Generate an initial population of salps randomly
x_i (i = 1, 2, ..., n) considering upper bound u_b and lower bound l_b
While (t < maximum number of iteration) **do**
Calculate the fitness function of each salp ($f(x_i)$)
Set the best salp to x_{best}
Update the value of c_1 according to Eq. [13]
For (each salp (x_i)) **do**
If x_i is the leader **then**
Update the position of leading salp using Eq. [12]
Else
Update the position of the follower salp using Eq. [14]
End if
Update the position of the salp
End for
Update the position of the salps based on the upper and lower bounds
End while
Return *the best salp* x_{best}

Improvement method GA-SSA. This is a searching technique developed for optimal location and sizing of DG and capacitors. The problem consists of 2 parts. The first is the optimal location of DG and capacitors and the second is the optimal location. Result for the first part is an integer, which is either a bus number where DGs and capacitors are suggested to be installed. This needs an integer-based optimization algorithm. GA has been chosen to play this role because of its attractive quality. The answer obtained from GA solution is used in SSA algorithm to optimize the sizing for DG. SSA has the fast convergence ability, which is a great attractive property for a large iterative and time consuming problem. Therefore the algorithm is recovered in 16 steps:

Step 1: Read data from network (R, X, PLoad, QLoad).

Step 2: Determine the number of chromosomes, generation, and mutation rate and crossover rate value.

Step 3: Initial set of random size of DG and capacitors.

Step 4: Initial set of random location of DG and capacitors.

Step 5: Calculate the objective values (Parts of objective function in different load levels).

Step 6: Calculate the loss of active and reactive power losses in different load levels .

Step 7: Using SSA to calculate fitness for optimal sizing of DG and capacitors.

Step 8: Evaluation of fitness value of chromosomes by calculating objective function.

Step 9: Using GA to calculate fitness for optimal sitting of DG (Selection – Crossover – Mutation).

Step 10: Calculate the objective values (Parts of objective function in different load levels).

Step 11: Calculate the loss of active and reactive power losses in different load levels.

Step 12: Using SSA to calculate fitness for optimal sizing of DG and capacitors.

Step 13: Searching for best solution.

Step 14: Check the stop Criterion.

Step 15: If the stopping criteria is satisfied then stop, else go to step 5.

Step 16: Best solution.

Simulations and results. The hybrid GA-SSA technique for optimal location and sizing of DGs and capacitors have been implemented in MATLAB 7.10 programming language and the simulation conducted on a computer Core (TM) i5 a 1.90 GHz with 8 Go RAM. This algorithm tested in IEEE 34-bus [20] radial distribution system and the real network 112-bus radial distribution system [26] shown in Fig. 1 and Fig. 2 respectively.

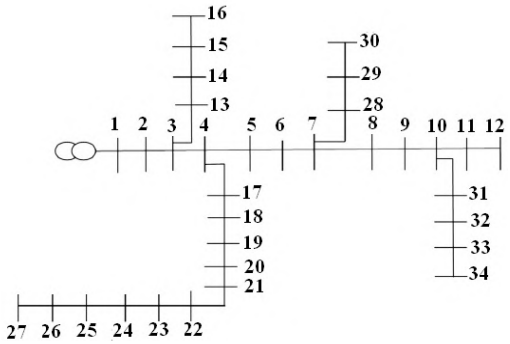

Fig. 1. IEEE 34-Bus test system

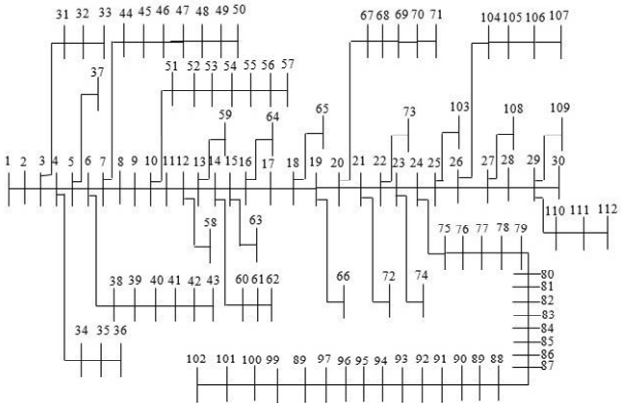

Fig. 2. Real network 112-bus

IEEE 34-Bus radial distribution network. The active and reactive power demand in peak load are 11303 KW and 7044.2 KVar respectively. The capacitors are installed in the system such that the reactive power generated by the maximum total capacity does not exceed 20% of the reactive power in peak load [27]. That corresponds to reactive power 1408.84 KVar. We therefore chose to install 7 capacitors with 200 KVar each one at optimal locations in order to maximize the objective function equation [1].

Three different load levels are considered in this paper: light, medium and peak load. The load growth rate is considered 1 % in each year. Tables 1 shows technical and commercial information of 3 load duration (h/year) and electricity market price ($/MWh) and Table 2 shows the parts of the objective function.

Now, in order to minimize active and reactive power losses and improve the voltage profile, 4 cases are considered. Figure 3 shows the locations and sizes of the capacitor banks as well as the distributed generators used for the 4 cases which are as follows:

- Case 1: without installing equipment's.
- Case 2: only 7 capacitors of 200 KVar are optimally placed at bus 3, 7, 10, 15, 24, 31 and 34.
- Case 3: only 5 DGs are installed. 4 DGs are optimally placed at bus 4, 8, 22 and 24 with capacity of 500 KW, and one DG at bus 33 with capacity of 250 KW.
- Case 4: 5 DGs and 7 capacitors are installed simultaneously with same optimal placement.

Table 1

Technical and commercial information of load and electricity market price

Network condition	Time duration (h/year)	Market price ($/MWh)
Light load	2190	35
Medium load	4745	49
Peak load	1825	70

Table 2

Parts of objective function in different load levels

Economical cost	Network condition	Costs ($)
Capacitor installation cost	Light load	14000
DG installation cost		397500
DG maintenance cost		15330
Total		426830
Capacitor installation cost	Medium load	14000
DG installation cost		397500
DG maintenance cost		33215
Total		444715
Capacitor installation cost	Peak load	14000
DG installation cost		397500
DG maintenance cost		12775
Total		424275

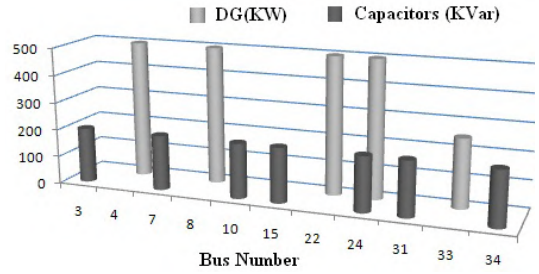

Fig. 3. Location and size of DGs and capacitors installed in IEEE 34-Bus

The optimum sizes of DGs placed respectively at optimal bus, obtained to minimize active and reactive power losses and improve the voltage profile are:

- in case 3 DGs values are determined as 412.19 KW, 86.53 KW, 431.82 KW, 463.02 and 88.14 KW but the optimal size of all DGs in case 4 are 405.06 KW, 151.21 KW, 252.43 KW, 355.50 and 76.27 KW in bus 4, 8, 22, 24 and 33 respectively.

These results are presented in Fig. 4.

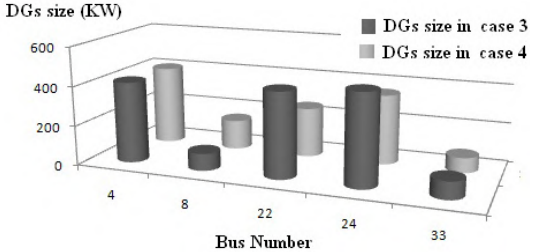

Fig. 4. Location and size of DGs in case 3 and 4

Table 3 represents the loss of active and reactive power in the 4 cases considered with the 3 load levels: light, medium and peak load.

Table 3

The loss of active and reactive power in the four cases considered with the three load levels

	Load level	Active power losses (kW)	Reactive power losses (KVar)
Without equipment's	Light load	512.6674	140.9201
	Medium load	642.3039	176.4590
	Peak load	1136.6012	311.7137
With only capacitors	Light load	498.2234	116.5629
	Medium load	567.5571	132.0432
	Peak load	1005.4012	282.4204
With DGs only	Light load	267.3280	59.5580
	Medium load	270.2497	61.4683
	Peak load	676.1747	189.2695
With DGs and capacitors	Light load	178.9525	42.7015
	Medium load	205.4583	50.9711
	Peak load	358.9739	96.3500

Note that for Case 2, the loss of active and reactive power are reduced by 2.81 %, 11.63 %, 11.54 % (Table 4) and 17.28 %, 25.17 %, 9.39 % (Table 5), respectively, and for 3 load levels respectively as compared with the case 1.

Case 3, the loss of active and reactive power are more reduced than the case 2 of 47.85 %, 57.92 %, 40.50 % (Table 4) and 57.73 %, 65.16 %, 39.28 % (Table 5) respectively, and three load levels respectively as compared to the case 1.

Case 4, the loss of active and reactive power are even more reduced than cases 2 and 3, 65.09 %, 68.01 %, 68.42 % (Table 4) and 69.70 %, 71.11 %, 69.09 % (Table 5), respectively and for 3 load levels respectively as compared to the case 1.

Table 4

Benefits of active power losses reduction

	Light load	Medium load	Peak load
Case 2	2.81 %	11.63 %	11.54 %
Case 3	47.85 %	57.92 %	40.50 %
Case 4	65.09 %	68.01 %	68.42 %

Table 5

Benefits of reactive power losses reduction

	Light load	Medium load	Peak load
Case 2	17.28 %	25.17 %	9.39 %
Case 3	57.73 %	65.16 %	39.28 %
Case 4	69.70 %	71.11 %	69.09 %

Table 6 represents a comparative study between the results obtained by the proposed algorithm GA-SSA and those obtained by SSA, GA, PSO (particle swarm optimization) and the HPSO (hybrid particle swarm optimization) algorithms [27].

Table 6

Comparative study in medium load

Size	GA-SSA	GA	SSA	PSO	HPSO
DG size in total (kW)	1240.47	1423.78	1283.14	1653.62	1493.56
Capacitor size in total (KVar)	1400	2126	1400	2542	2452
Power losses (KW)	527.55	608.84	612.55	620.64	614.55

We note that the loss of active power obtained by the GA-SSA algorithm is 8.55 % better than those values obtained by PSO algorithm and 7.65 % than those obtained by algorithm HPSO. Thus of viewpoint of production cost, reactive power obtained by GA-SSA (1400 kVA) is also better than that obtained by PSO (2542 kVA) and HPSO (2452 kVA).

This comparison clearly demonstrates the effectiveness of the proposed genetic salp swarm algorithm compared to genetic algorithm, salp swarm algorithm, particle swarm optimization and hybrid particle swarm optimization algorithm.

Fig. 5-8 represents the voltage profile at the distribution network for the 4 cases considered and for the 3 load levels. Table 6 shows the minimum voltage in the distribution network for the 4 cases considered and the 3 load levels. The values obtained for peak load: 0.8857 pu at bus 27 case 1, 0.9390 pu at bus 27 case 2, 0.9403 pu at bus 24 case 3 and 0.9647 pu at bus 27 case 4 show good improvement under voltage where the values of the voltage obtained are between 0.9647 in the different load levels: light, medium and peak.

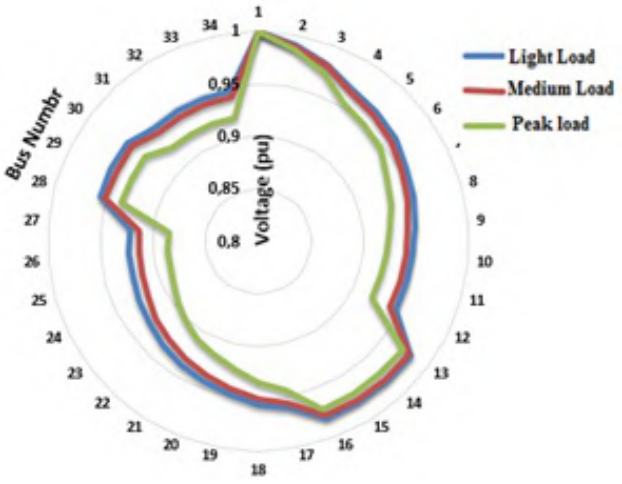

Fig. 5. Performance of voltage profile for 34 bus radial distribution in different load levels without installation of capacitors and DGs

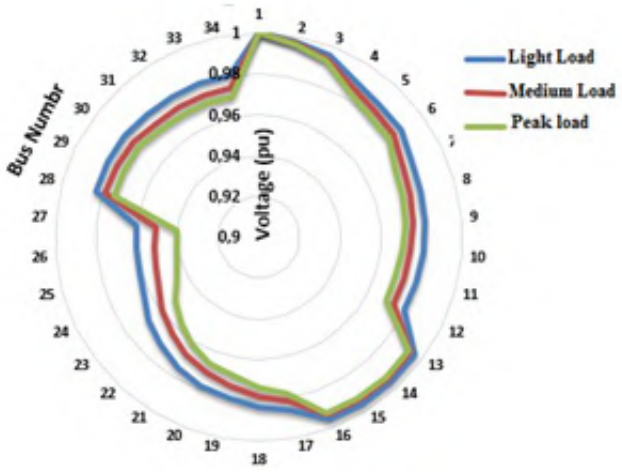

Fig. 6. Performance of voltage profile for 34 bus radial distribution in different load levels after installation of capacitors

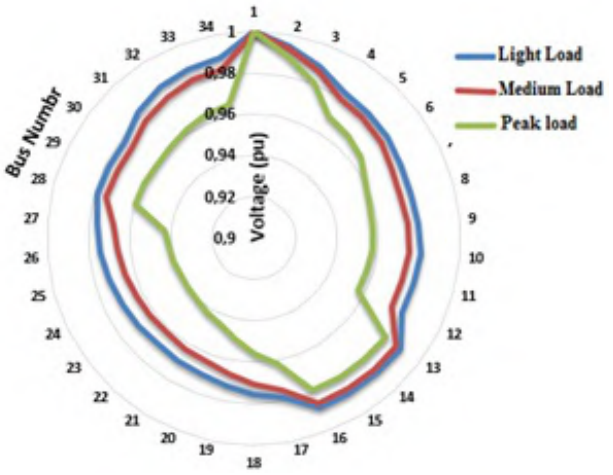

Fig. 7. Performance of voltage profile for 34 bus radial distribution in different load levels after installation of DGs

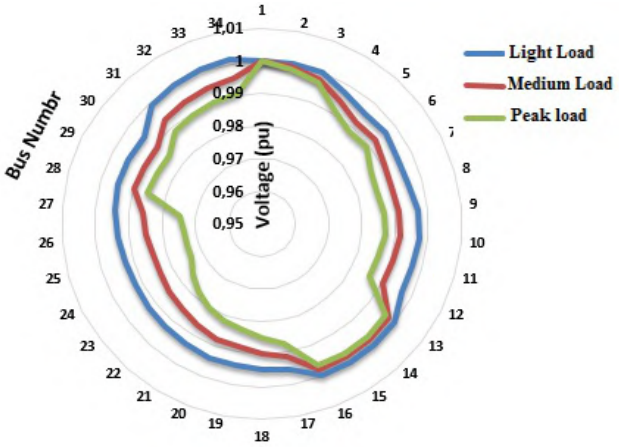

Fig. 8. Performance of voltage profile for 34 bus radial distribution in different load levels after installation of capacitors and DGs

Real distribution network of 112-Bus. The active and reactive power demand in peak load are 11303 KW and 7044.2 KVar respectively. Table 7 shows the parts of objective function in different load levels.

Table 7

Parts of objective function in different load levels of real network 112-bus

Economical cost	Network condition	Costs ($)
Capacitor installation cost	Light load	14400
DG installation cost		357120
DG maintenance cost		18396
Total		389916
Capacitor installation cost	Medium load	14400
DG installation cost		477000
DG maintenance cost		39858
Total		531258
Capacitor installation cost	Peak load	14400
DG installation cost		477000
DG maintenance cost		15330
Total		506730

The 4 cases studied to have the effectiveness of the method in the real 112-bus network (Fig. 2) are:

- Case 1: without installing equipment's.
- Case 2: in this case, we have installed 6 capacitors with 150 KVar. The optimal locations are obtained at the bus: 4, 25, 34, 38, 79 and 98.
- Case 3: we have installed 6 DGs: 2 DGs are optimally placed at bus 4 and 33 with capacity of 500 KW, and 4 DG at bus 33, 58, 88 and 92 with capacity of 250 KW.
- Case 4: 5 capacitors are installed with optimal placement at bus 6, 25, 34, 56 and 102 with 150 KVar and 4 DGs with optimal locations obtained at the bus: 12, 45, 76 and 92 with capacity of 250 KW.

The comparison between the results obtained by the GA-SSA algorithm and the SSA and GA algorithms are represented in Table 8.

Table 8

Comparison between the results obtained by the GA-SSA algorithm and other algorithms (real network 112-bus)

Case		V_{min} (p.u)	P_{loss} (KW)	Q_{loss} (KVar)	CPU time (s)
Base Case		0.9314	288.14	189.64	–
With only capacitors	GA-SSA	0.9394	224.16	174.22	36
	GA	0.9377	236.09	182.52	66
	SSA	0.9381	228.12	179.01	42
With only DGs	GA-SSA	0.9569	124.96	102.19	37
	GA	0.9481	141.08	142.71	74
	SSA	0.9498	136.56	137.24	48
With capacitors and DGs	GA-SSA	0.9802	56.32	42.93	39
	GA	0.9684	96.37	71.27	84
	SSA	0.9776	82.06	68.62	52

The benefits of active and reactive power losses reduction of cases 2 – 4 are compared with those of case 1 for 112-bus are presented in Table 9, 10, respectively.

Table 9

Benefits of active power losses reduction compared with the case 1 in real network 112-bus

	Benefits of active power losses reduction		
Load level	Light load	Medium load	Peak load
Case 2	38.81 %	22.20 %	30.64 %
Case 3	64.85 %	56.63 %	68.50 %
Case 4	96.09 %	80.45 %	74.42 %

Table 10

Benefits of reactive power losses reduction compared with the case 1 in real network 112-bus

	Benefits of reactive power losses reduction		
Load level	Light load	Medium load	Peak load
Case 2	17.28 %	8.13 %	9.39 %
Case 3	57.73 %	46.11 %	39.28 %
Case 4	79.70 %	77.36 %	69.09 %

Fig. 9 represents the voltage profile of the real network 112-bus without installation of the equipment where the minimum values of the voltage for the 3 load levels, peak, medium and light are respectively: 0.9114, 0.9316, 0.9303.

Fig. 10, corresponding to case 2, represents the real 112-bus network voltage profile after the installation of capacitors where the minimum voltage values for the 3 load levels, peak, medium and light are respectively 0.9343, 0.9394 and 0.9422.

The installation of the capacities also allowed a reduction of active power losses of 38.82 %, 22.20 %, 30.64 % and a reduction of reactive power losses of 17.28 %, 8.13 %, 9.39 % compared to case 1, respectively for the 3 load levels.

Fig. 11, corresponding to case 3, represents the real network 112-bus network voltage profile after installation of DGs where the minimum voltage values for the 3 load levels, peak, medium and light are respectively 0.9535, 0.9569 and 0.9578.

The installation of the DGs also allows a reduction of active power losses of 64.85 %, 56.36 %, 68.50 % and a reduction of reactive power losses of 57.73 %, 46.11 %, 39.28 % compared to case 1 respectively for the 3 load levels.

Fig. 12, corresponding to case 4, represents the real network 112-bus network voltage profile after simultaneous installation of DGs and capacitors where the minimum voltage values for the 3 load levels, peak, medium and light are 0.9792, 0.9802 and 0.9812 respectively.

The installation of the 2 equipment allowed a further reduction of active power losses of 96.09 %, 80.45 % and 74.42 % and a reduction of reactive power losses of 79.70 %, 77.36 % and 69.09 % compared to case 1 respectively for the 3 load levels.

The results obtained in this scenario are better than those obtained in case 2 and case 3 from the point of view of the voltage profile and the maximization of the benefit of the DGs installation and capabilities.

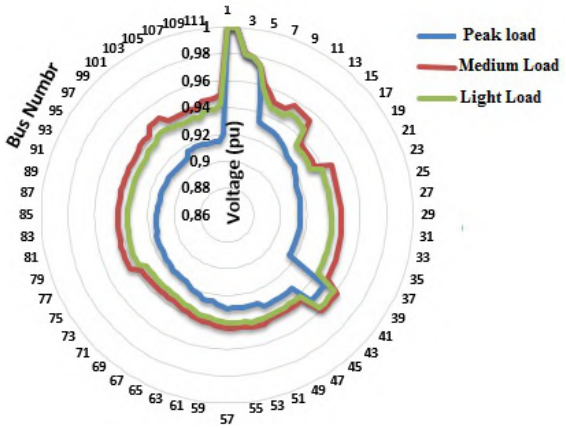

Fig. 9. Performance of voltage profile for real network 112-bus in different load levels without installation of capacitors and DGs

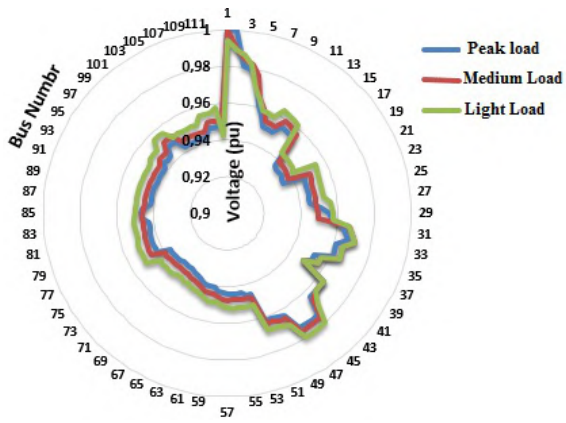

Fig. 10. Performance of voltage profile for real network 112-bus in different load levels after installation of capacitors

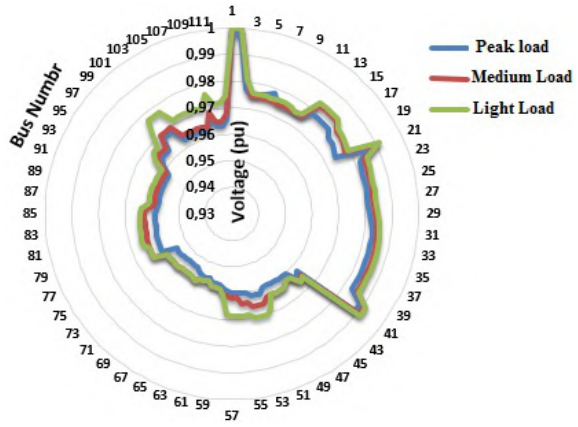

Fig. 11. Performance of voltage profile for real network 112-bus in different load levels after installation of DGs

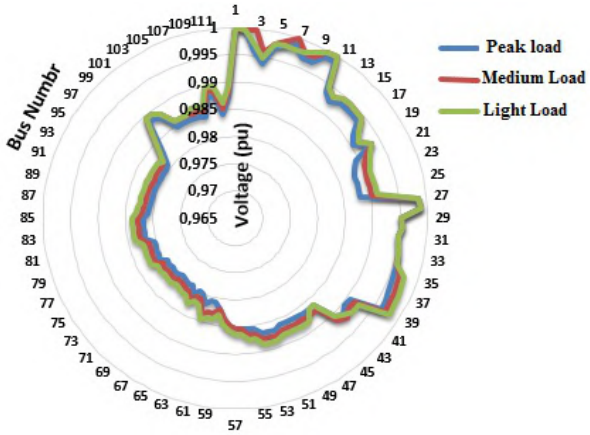

Fig. 12. Performance of voltage profile for real network 112-bus in different load levels after installation of capacitors and DGs

Conclusion. In this article, two algorithms genetic and salp swarm algorithm have been proposed for the simultaneously optimal placement of distributed generation and capacitors in a distribution system. These two algorithms are applied on four different cases. The purpose of this combination is to maximize the installation benefit of distributed generation and capacitor banks and minimize active and reactive power losses in radial distribution network, also to minimize the computation time, and to seek the optimal overall solution. This method is applied on radial distribution network IEEE 34-bus and real Algerian distributed network of Djanet 112-bus, the result shows that, cases with simultaneous placement of distributed generation and capacitor have much improvement of voltage profile and power loss reduction compared with others methods.

REFERENCES

1. Satyakar V.V.K., Viswanatha Rao J., Manikandan S. Analysis of radial distribution system by optimal placement of DG using DPSO. *International Journal of Engineering Research & Technology*, 2012, vol. 1, iss. 10, pp. 1-7.

2. Khanjanzadeh A., Arabi M., Sedighizadeh M., Rezazadeh A. Distributed generation allocation to improve steady state voltage stability of distribution networks using particle swarm optimization and genetic algorithm. *Canadian Journal on Electrical and Electronics Engineering*, 2011, vol. 2, no. 6.

3. Herbadji O., Nadhir K., Slimani L., Bouktir T. Optimal power flow with emission controlled using firefly algorithm.

2013 5th International Conference on Modeling, Simulation and Applied Optimization (ICMSAO), Apr. 2013. **doi: 10.1109/icmsao.2013.6552559.**

4. Gkaidatzis P.A., Bouhouras A.S., Doukas D.I., Sgouras K.I., Labridis D.P. Load variations impact on optimal DG placement problem concerning energy loss reduction. *Electric Power Systems Research*, 2017, vol. 152, pp. 36-47. **doi: 10.1016/j.epsr.2017.06.016**.

5. Baghipour R., Hosseini S.M. Placement of DG and capacitor for loss reduction, reliability and voltage improvement in distribution networks using BPSO. *International Journal of Intelligent Systems and Applications*, 2012, vol. 4, no. 12, pp. 57-64. **doi: 10.5815/ijisa.2012.12.08.**

6. Kumar Injeti S., Shareef S.M., Kumar T.V. Optimal allocation of DGs and capacitor banks in radial distribution systems. *Distributed Generation & Alternative Energy Journal*, 2018, vol. 33, no. 3, pp. 6-34. **doi: 10.1080/21563306.2018.12016723.**

7. Kannan S.M., Renuga P., Kalyani S., Muthukumaran E. Optimal capacitor placement and sizing using Fuzzy-DE and Fuzzy-MAPSO methods. *Applied Soft Computing*, 2011, vol. 11, no. 8, pp. 4997-5005. **doi: 10.1016/j.asoc.2011.05.058.**

8. Yang X.-S. Firefly Algorithms for Multimodal Optimization. In: Watanabe O., Zeugmann T. (eds) Stochastic Algorithms: Foundations and Applications. SAGA 2009. *Lecture Notes in Computer Science*, vol. 5792. **doi: 10.1007/978-3-642-04944-6_14.**

9. Aydin I. A new approach based on firefly algorithm for vision-based railway overhead inspection system. *Measurement*, 2015, vol. 74, pp. 43-55. **doi: 10.1016/j.measurement.2015.07.022.**

10. Gao M.-L., Li L.-L., Sun X.-M., Yin L.-J., Li H.-T., Luo D.-S. Firefly algorithm (FA) based particle filter method for visual tracking. *Optik*, 2015, vol. 126, no. 18, pp. 1705-1711. **doi: 10.1016/j.ijleo.2015.05.028.**

11. Syahputra R., Soesanti I., Ashari M. Performance enhancement of distribution network with DG integration using modified PSO algorithm. *Journal of Electrical Systems*, 2016, vol. 12, iss. 1, pp. 1-19.

12. Rezaei M., Ghanbari M. Optimization of sizing and placement of photovoltaic (PV) system in distribution networks considering power variations of PV and consumers using dynamic particle swarm optimization algorithm (DPSO). *Indian Journal of Fundamental and Applied Life Sciences*, 2015, vol. 5(S1), pp. 3321-3327.

13. Siavash M., Pfeifer C., Rahiminejad A., Vahidi B. Reconfiguration of smart distribution network in the presence of renewable DG's using GWO algorithm. *IOP Conference Series: Earth and Environmental Science*, 2017, vol. 83, p. 012003. **doi: 10.1088/1755-1315/83/1/012003**.

14. Ajenikoko G.A., Ajenikoko O.E.O., Adedoyin A., Badmus B.E., Lawal E.A. Application of genetic algorithm to network feeder reconfiguration in radial distribution system. *International journal of advanced scientific and technical research*, 2018, vol. 5, no. 8, pp. 15-29. **doi: 10.26808/rs.st.i8v5.02.**

15. El-Fergany A.A., Abdelaziz A.Y. Cuckoo search-based algorithm for optimal shunt capacitors allocations in distribution networks. *Electric Power Components and Systems*, 2013, vol. 41, no. 16, pp. 1567-1581. **doi: 10.1080/15325008.2013.834525.**

16. Mohamed Shuaib Y., Surya Kalavathi M., Christober Asir Rajan C. Optimal capacitor placement in radial distribution system using Gravitational Search Algorithm. *International Journal of Electrical Power & Energy Systems*, 2015, vol. 64, pp. 384-397. **doi: 10.1016/j.ijepes.2014.07.041.**

17. Sambaiah K.S., Jayabarathi T. Optimal allocation of renewable distributed generation and capacitor banks in distribution systems using salp swarm algorithm. *International journal of renewable energy research*, 2019, vol. 9, no. 1, pp. 96-107.

18. Mohamed E.A., Mohamed A.-A.A., Mitani Y. Hybrid GMSA for optimal placement and sizing of distributed generation and shunt capacitors. *Journal of Engineering Science and Technology Review*, 2018, vol. 11, no. 1, pp. 55-65. **doi: 10.25103/jestr.111.07**.

19. Duong M., Pham T., Nguyen T., Doan A., Tran H. Determination of optimal location and sizing of solar photovoltaic distribution generation units in radial distribution systems. *Energies*, 2019, vol. 12, no. 1, p. 174. **doi: 10.3390/en12010174.**

20. Sajjadi S.M., Haghifam M.-R., Salehi J. Simultaneous placement of distributed generation and capacitors in distribution networks considering voltage stability index. *International Journal of Electrical Power & Energy Systems*, 2013, vol. 46, pp. 366-375. **doi: 10.1016/j.ijepes.2012.10.027.**

21. Xin J., Zhong J., Yang F., Cui Y., Sheng J. An improved genetic algorithm for path-planning of unmanned surface vehicle. *Sensors*, 2019, vol. 19, no. 11, p. 2640. **doi: 10.3390/s19112640.**

22. Khanra A., Pal T., Maiti M.K., Maiti M. Multi-objective four dimensional imprecise TSP solved with a hybrid multi-objective ant colony optimization-genetic algorithm with diversity. *Journal of Intelligent & Fuzzy Systems*, 2019, vol. 36, no. 1, pp. 47-65. **doi: 10.3233/jifs-172127.**

23. Mirjalili S., Gandomi A.H., Mirjalili S.Z., Saremi S., Faris H., Mirjalili S.M. Salp Swarm Algorithm: A bio-inspired optimizer for engineering design problems. *Advances in Engineering Software*, 2017, vol. 114, pp. 163-191. **doi: 10.1016/j.advengsoft.2017.07.002.**

24. Mafarja M., Eleyan D., Abdullah S., Mirjalili S. S-Shaped vs. V-Shaped Transfer Functions for Ant Lion Optimization Algorithm in Feature Selection Problem. *Proceedings of the International Conference on Future Networks and Distributed Systems - ICFNDS'17*, 2017. **doi: 10.1145/3102304.3102325.**

25. Hegazy A.E., Makhlouf M.A., El-Tawel G.S. Improved salp swarm algorithm for feature selection. *Journal of King Saud University – Computer and Information Sciences*, 2020, vol. 32, no. 3, pp. 335-344. **doi: 10.1016/j.jksuci.2018.06.003.**

26. Amrane Y. *Optimal reactive power compensation in the transport and distribution networks*. Doctoral Thesis, University of Science and Technology Houari Boumediene, Algeria, 2014.

27. Chandramohan S., Atturulu N., Devi R.P.K., Venkatesh B. Operating cost minimization of a radial distribution system in a deregulated electricity market through reconfiguration using NSGA method. *International Journal of Electrical Power & Energy Systems*, 2010, vol. 32, no. 2, pp. 126-132. **doi: 10.1016/j.ijepes.2009.06.023.**

Received 24.06.2020

Chabane Djabali[1], *Ph.D Student,*
Tarek Bouktir[1], *Professor,*
[1] Department of Electrical Engineering,
University of Ferhat Abbes Setif 1,
19000, Setif, Algeria.
e-mail: Djabali.chabane@gmail.com, tbouktir@univ-setif.dz

How to cite this article:
Djabali C., Bouktir T. Simultaneous allocation of multiple distributed generation and capacitors in radial network using genetic-salp swarm algorithm. *Electrical engineering & electromechanics*, 2020, no. 4, pp. 59-66. **doi: 10.20998/2074-272X.2020.4.08.**

UDC 621.316.925 **doi: 10.20998/2074-272X.2020.4.09**

V.F. Syvokobylenko, V.A. Lysenko

IMPROVING THE EFFICIENCY OF FAULT PROTECTION SYSTEMS OF ELECTRICAL GRIDS BASED ON ZERO SEQUENCE VOLTAGES AND CURRENTS WAVELET TRANSFORMS

Introduction. A significant proportion of earth faults in medium voltage networks represents a short-lived and transient process. Problem. In such cases, earth fault protection that responds to steady-state current and voltage is not able to operate properly. Purpose. To develop earth faults protection selective algorithm using transient components, that occur in zero-sequence currents and voltage in the fault process. Method. A mathematical model of the power supply system was applied to study the transient components of currents and voltage of zero sequence in compensated electrical networks with phase-to-earth faults, and a those model also is used to test the operation of the developed protection algorithm. The results showed that, the reactive power for transient components, of the frequency greater by 4-6 times, than fundamental frequency, which are extracted from the current and voltage of zero sequence by wavelet transform in compensated electrical networks on the damaged feeder, is positive regardless of the degree of compensation of the capacitive current. That may be the basis of the principle of directional protection. Originality. Phase-to-earth fault selective protection algorithm has been developed. In that algorithm, first derivatives of currents and voltages of zero sequence are found, to reduce the influence of aperiodic components. And then, by using of the wavelet transform with Morlet mother function, an orthogonal components are extracted from them. Reactive power is calculated for transient component. If that reactive power excess of threshold, the relay will make a decision. The reliability of the developed protection algorithm is confirmed by the results of mathematical modelling and verification of the test sample at the laboratory stand and by means of field signals that were recorded by digital loggers at the substations. References 10, figures 5.
Key words: **electrical grid, earth fault protection, current, voltage, zero sequence, wavelet transform, reactive power.**

Для електричних мереж напругою 6-35 кВ, що працюють з компенсованою або ізольованою нейтраллю, розроблено селективний захист від замикань фази на землю, який реагує на напрям реактивної потужності, яка визначається за допомогою коефіцієнтів вейвлет-перетворень струму і напруги нульової послідовності, а також їх похідних, введених для забезпечення фазового зсуву на 90 градусів і підвищення чутливості захисту. Коефіцієнти знаходять шляхом згортки дискретних значень струму, напруги та їх похідних із сигналами материнської функції Морле, обчислення яких проводиться за допомогою квадратної матриці, для якої викладено правила її формування. Реактивна потужність визначається на кожному кроці розрахунку як сума добутків вейвлет-коефіцієнтів струму і похідної від напруги, а також напруги і похідної від струму, тобто коефіцієнтів, що мають однаковий порядковий номер. Пуск захисту відбувається за фактом перевищення амплітудою напруги нульової послідовності заданого значення. За допомогою математичної моделі мережі виконано дослідження поведінки захисту за глухих і дугових замикань фази на землю, для різного ступеня компенсації ємнісних струмів, для різних значень напруги в момент замикання. У всіх режимах отримано надійну роботу захисту, чутливість якого в 5-8 разів перевищує чутливість захисту за алгоритмом, заснованим на перетворенні Фур'є. Бібл. 10, рис. 5.
Ключові слова: **електрична мережа, захист від замикань на землю, струм, напруга, нульова послідовність, вейвлет-перетворення, реактивна потужність.**

Для электрических сетей напряжением 6-35 кВ, работающих с компенсированной или изолированной нейтралью, разработана селективная защита от замыканий фазы на землю, которая реагирует на направление реактивной мощности, определяемое с помощью коэффициентов вейвлет-преобразований тока и напряжения нулевой последовательности, а также их производных, введенных для обеспечения фазового сдвига на 90 градусов и повышения чувствительности защиты. Коэффициенты находят путем свертки дискретных значений тока, напряжения и их производных с сигналами материнской функции Морле, вычисление которых производится с помощью квадратной матрицы, для которой изложены правила её формирования. Реактивная мощность определяется на каждом шаге расчета как сумма произведений, совпадающих по фазе и имеющих одинаковый порядковый номер вейвлет-коэффициентов тока и производной от напряжения, а также напряжения и производной от тока. В качестве пускового органа защиты используется превышение амплитудой напряжения нулевой последовательности заданного значения. С помощью математической модели сети выполнены исследования поведения защиты при глухих и дуговых замыканиях фазы на землю, при различной степени компенсации емкостных токов, при различных значениях напряжения в момент замыкания. Во всех режимах получена надежная работа защиты, чувствительность которой в 5-8 раз выше чувствительности защиты, основанной на преобразованиях Фурье. Библ. 10, рис. 5.
Ключевые слова: **электрическая сеть, защита от замыканий на землю, ток, напряжение, нулевая последовательность, вейвлет-преобразование, реактивная мощность.**

The urgency of the problem and its connection with the applied tasks. In medium voltage power supply systems, damage to the phase insulation leads to single-phase earth faults. In this case, the load current is usually significantly higher than the steady-state earth fault current, which complicates the operation of protection against such faults. Nevertheless, a single-phase earth fault can be extremely dangerous. It can cause fires, damage to electrical equipment as a result of overvoltages or heating by fault current, electric shock to people and animals. According to regulations in force in Ukraine, a section of the electrical grid with a single-phase earth fault must be immediately disconnected if it is located in

© V.F. Syvokobylenko, V.A. Lysenko

high-risk areas, such as coal mines or enterprises processing fire-hazardous raw materials. The use of a resonantly grounded neutral further complicates the operation of protection devices, as it significantly reduces the already insignificant current of a single-phase earth fault. Another important consequence of a small current of a single-phase earth fault is that such a fault is often unstable, the electric arc at the site of insulation damage can be repeatedly extinguished and ignited again, which gives a single-phase earth fault a permanent transient nature.

Review of publications and shortcomings of known solutions. There is a significant array of sources that investigate the protection of power supply systems against single-phase earth faults. A large number of reviews of publications on the considered problem [1-4] are evidence that the topic of protection against single-phase earth faults today remains a serious challenge for both scientific and theoretical research and engineering and practical developments. In particular, the new methods of signal processing and analysis that have been developed in connection with the development of modern communication systems remain not fully implemented.

Since it is very difficult to obtain information about such a fault from the steady-state current of the zero sequence of the feeder in a single-phase earth fault, much attention is paid to the transient current.

In particular, in [5] it is proposed to use digital filters with infinite pulsed response to extract the information parameter from currents and voltages of zero sequence. In [6], it is proposed to use the Fourier transform to obtain the phase and amplitude characteristics of the voltage and current of zero sequence. In [7], the properties of Fourier transform and wavelet transform are compared on the example of electric arc detection. In [8], it is proposed to detect faults based on the coefficients obtained by wavelet transform. In [9], single-phase faults in a grid with an unearthed neutral are simulated using ATP/EMTP software, and an algorithm for detecting such a fault using wavelet transform is also proposed. But the characteristics of protection algorithms in [7-9] are not considered.

The goal of the paper is to increase the sensitivity and speed of selective protection systems of electrical grids with isolated or compensated neutral based on the use of wavelet transforms of transient components of zero sequence voltages and currents that occur when a phase-to-earth faults occurs during discharge and recharge of grid capacities.

The main material and the results obtained. The study of transients in single-phase earth faults (SEFs) and analysis of the protection operation is performed using a mathematical model, the description of which is given in [10]. Consider a typical two-transformer substation for a 6 kV power supply system, which consists of two 110/6 kV step-down power transformers T1 and T2, busbars of the first СШ-1 and the second СШ-2 sections, which supply cable lines Ф1-Ф3, on each of which zero-sequence current transformers (ZSCTs) are installed. Measuring voltage transformers TH1, TH2 are connected to busbars. The earth fault protection of the phase is connected to the secondary circuits of ZSCTs and THs. The neutral of the grid of the first section is grounded through a reactor with resonant inductance of 0.161 H, and the phase capacitances to ground for feeders Ф1-Ф3 connected to this section are 1, 8 and 12 μF, respectively, interphase capacitances are 2 μF, steady-state earth fault current is 72.3 A. The solution of differential equations in the mathematical model is performed by the implicit method with a calculation step h = 0.667 ms. The calculated values in the simulation are presented in per-unit (p.u.) values to the basic:

$$U_b = \frac{\sqrt{2}\cdot 6000}{\sqrt{3}} = 4899 \text{ V};$$

$$I_b = \sqrt{2}\cdot I_{0f} = \sqrt{2}\cdot 72.36 = 102.33 \text{ A};$$

$$Q_b = U_b \cdot I_b = 501\cdot 10^3 \text{ VA},$$

where U_b, I_b, Q_b are the basic voltage, current and power, respectively; I_{0f} is the single-phase earth fault current.

The frequency [5] and multifrequency [6] protections against SEFs proposed in recent years are based on the use of higher harmonics in currents and voltages that occur in the first moment of the fault and therefore depend on the instantaneous value of the phase voltage on the damaged phase. The degree of distortion of sinusoidal voltages and currents depends on this voltage, which can be seen, for example, from Fig. 1,*a*,*b*, which shows the results of modelling the SEF at the initial voltage on the damaged phase, equal to the amplitude one (Fig. 1,*a*), as well as to zero one (Fig. 1,*b*). In the first case, there is a fairly long-term coincidence in the phase of current and voltage, while in the second one, the phase coincidence in phase of these signals is much shorter. The sensitivity of the protection algorithm, which is based on the use of the product of these signals, which is proportional to the reactive power, depends on the indicated initial conditions, which must be taken into account when developing new methods of protection.

In 6-35 kV electrical grids operating with neutral isolated or grounded through a Petersen coil, the transients in arc phase-to-ground faults are transient, and therefore there are questions about the correctness of the application of protection algorithms based on the use of frequency [5] and multifrequency [6] components in currents $3i_0$ and voltages $3u_0$ of zero sequence obtained by means of Fourier spectral transforms. For such processes it is more rational to use wavelet transforms (WTs), which allow to decompose the input, time-varying signal $x(t)$ into frequency-time components in the form of coefficients $CW(a,b,t)$ which depend on the selected mother function $g(a,b,t)$ as well as on the coefficients of frequency scale a and time shift b [8]. The study of the characteristics of WTs of currents and voltages and the possibility of using the phase spectrum (phase shift angle) or resistances to build a group protection against phase faults to earth is considered in [1-4]. However, an important task is to develop a stand-alone protection for each feeder, which operates at both arc and steady-state faults, uses the ratio between currents and voltages and has a higher sensitivity.

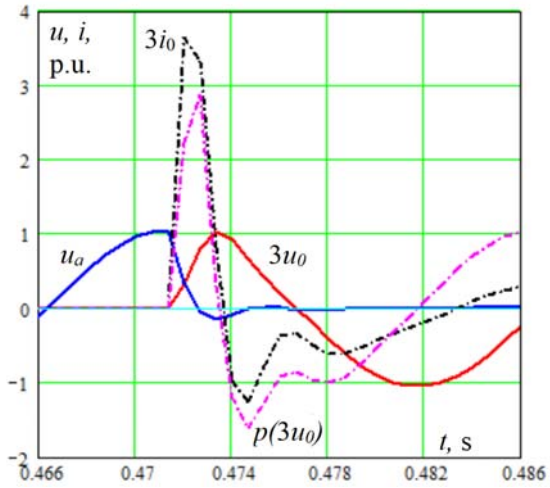

a

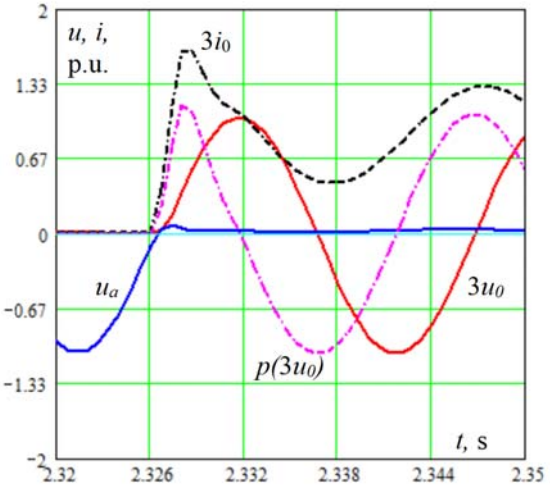

b

Fig. 1. Results of simulation of SEF which occurred at the maximum (*a*) and zero (*b*) instantaneous voltage value on the damaged phase u_a

As shown in [8], the continuous wavelet transform of signals is performed using an integral expression containing the product of this signal and some basic function called the mother wavelet:

$$CW(a,b)=\frac{1}{\sqrt{a}}\int_{-\infty}^{\infty}x(t)\cdot g\left(\frac{t-b}{a}\right)dt\,. \qquad (1)$$

The input signals, in our case, are arrays of dimension N, consisting of discrete values of voltages and currents recorded by analog-to-digital converters during the fundamental frequency period (50 Hz) with discreteness with frequency f_s, as well as values derived from current $pi = p(3i_0)$ and voltage $pu = p(3u_0)$. They are used to compensate the angular phase shift of 90 degrees between the signals of current and voltage of zero sequence (Fig. 1). Numerical determination of derivatives, for example, by three instantaneous values of current (voltage) is performed by expressions that also use the calculation step and the angular frequency ω, which in our case were taken equal respectively 0.667 ms and 314 s^{-1}

$$px=\frac{dx}{dt}=\frac{1}{2\omega h}(3x_n-4x_{n-1}+x_{n-2})\,. \qquad (2)$$

As a mother wavelet, we take the complex Morlet wavelet [8], which is a plane wave modulated by the Gaussian curve

$$g(t)=\exp\left(-\frac{\pi\cdot t^2}{2}\right)\cdot\exp(j2\pi\cdot t)\,. \qquad (3)$$

To write (1) and (3) in discrete form, we substitute in (3) instead of time t the expression $(t - b)/a$ which contains the coefficients of frequency scale a and time shift b. From the obtained expression we select one of the components of the mother function $g(t)$, for example, imaginary (sine) $gS(n)$. Then the expressions for determining the k-th values of the coefficients of wavelet transforms will look like:

$$CW(k,a,b)=\frac{1}{\sqrt{a}}\sum_{n=1}^{N}x(k-n)\cdot g\left(\frac{n-b}{a}\right);$$
$$a=\frac{f_s}{f_n};\quad b=\frac{\pi\cdot a}{2}; \qquad (4)$$

$$gS(n)=\mathrm{Im}\left[g\left(\frac{n-b}{a}\right)\right]=$$
$$=\exp\left(-\pi\frac{(n-b)^2}{a^2}\cdot\sin\left(\frac{2\pi(n-b)}{a}\right)\right). \qquad (5)$$

As an example, Fig. 2 shows the nature of the change of the mother wavelet $gS(n)$ and its amplitude component $J(n)$ at a = 8, b = 15, N = 30, f_n = 250 Hz, f_s = 1500 Hz. Note that the frequency scale coefficient a is used to set the wavelet duration in the region of the desired frequency range f_n, the value of which we take equal to 250 Hz, which corresponds to the preferred harmonics at arc faults [6].

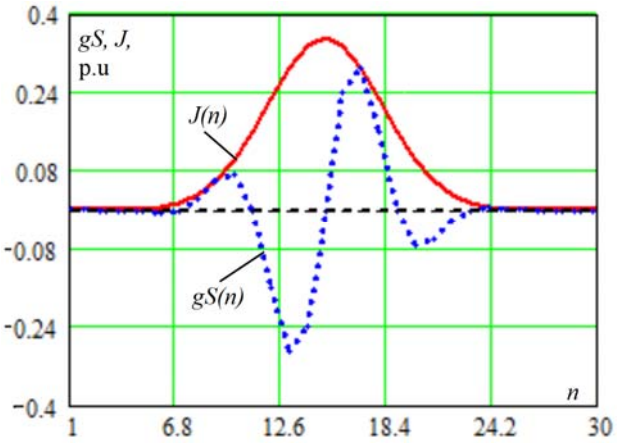

Fig. 2. Nature of the change of the mother wavelet $gS(n)$ and its amplitude $J(n)$

As can be seen from (4), the wavelet transform is a convolution of the values of the input signal (current, voltage and their derivatives) with the same number of values of the mother wavelet function. Here, the convolution is defined as the mutual correlation of one of these sequences with the other one inverse in time. To calculate the convolution, we use the matrix form of representation the inverse in time sequence of values

calculated by (5) in the case of n = 1,..,N. The matrix of the convolution core is a square one with dimension $N \times N$ and on its main diagonal there are the elements $gS_1 = gS_{(n=1)}$, on the diagonal above the main one – $gS_{N-1} = gS_{(n=N-1)}$, then – $gS_{N-2} = gS_{(n=N-2)}$, etc. On the diagonal below the main one there are the elements $gS_2 = gS_{(n=2)}$, then – accordingly gS_3,…, gS_N. For an array of N elements, the matrix will look like:

$$\boldsymbol{G}(gS) = \begin{matrix} gS_1 & gS_N & gS_{N-1} & ... & gS_2 \\ gS_2 & gS_1 & gS_N & ... & gS_3 \\ gS_3 & gS_2 & gS_1 & ... & gS_4 \\ ... & ... & ... & ... & ... \\ gS_N & gS_{N-1} & gS_{N-2} & ... & gS_1 \end{matrix}. \quad (6)$$

Vectors of wavelet transforms of voltages $\boldsymbol{W}_u$ and currents $\boldsymbol{W}_i$ of zero sequence, as well as derivatives of voltages $\boldsymbol{W}_{pu}$ and currents $\boldsymbol{W}_{pi}$ can be found as:

$$\begin{aligned} \boldsymbol{W}_u &= \boldsymbol{G}(gS) \times \boldsymbol{u}; \quad \boldsymbol{W}_i = \boldsymbol{G}(gS) \times \boldsymbol{i}; \\ \boldsymbol{W}_{pu} &= \boldsymbol{G}(gS) \times \boldsymbol{pu}; \quad \boldsymbol{W}_{pi} = \boldsymbol{G}(gS) \times \boldsymbol{pi}. \end{aligned} \quad (7)$$

The results of the calculation by expressions (7) of the coefficients of WT with the ordinal number n = 3 are presented in Fig. 3,*a*,*b*, from which it follows that in the initial section of the transient at the SEF there is a close coincidence in phase of the vectors $\boldsymbol{W}_i$ and $\boldsymbol{W}_{pu}$, as well as $\boldsymbol{W}_u$ and $\boldsymbol{W}_{pi}$. Here, by means of their product for signals with identical serial number it is possible to define value and a sign of reactive power (Fig. 3,*a*,*b*). The resulting reactive power Q can be defined as the sum of the products for all N coefficients, which significantly increases the sensitivity of the protection

$$Q = \sum_{k=1}^{N} W_u^k \times W_{pi}^k - \sum_{k=1}^{N} W_{pu}^k \times W_i^k. \quad (8)$$

The block diagram of the developed protection algorithm is shown in Fig. 4. It contains analog-to-digital converters (ADCs) to obtain discrete values of voltages $3u_0$ and currents $3i_0$, blocks *d*/*dt* to calculate by (2) the derivatives from these signals, the calculation unit for (5) of the mother wavelet function $g(S)$, unit for forming by (6) of the matrix $G(gS)$ of convolution nucleus, units W_u, W_i, W_{pu}, W_{pi} for calculation by (7) of the wavelet transform of voltages, currents and their derivatives, respectively, units of products for calculation by (8) of components of reactive power $Q_1 = Q_{upi} = W_u \times W_{pi}$ and $Q_2 = Q_{ipu} = W_{pu} \times W_i$, as well as an adder to determine the power $Q = Q_1 - Q_2$, at the exceeding which of the positive threshold value Q_t in the comparator, the corresponding signal enters the output relay through a number of logic elements AND, OR. The protection algorithm uses the voltage amplitude exceeding of the threshold value U_t as the starting body. The amplitude is determined in the unit U_a by its orthogonal components such as $\sqrt{(3u_0)^2 + (p3u_0)^2}$. After the protection has tripped, the relay is self-holding for the duration of its existence $U_m > U_t$ that provides reliable operation of protection after transition of an arc fault in a steady-state one.

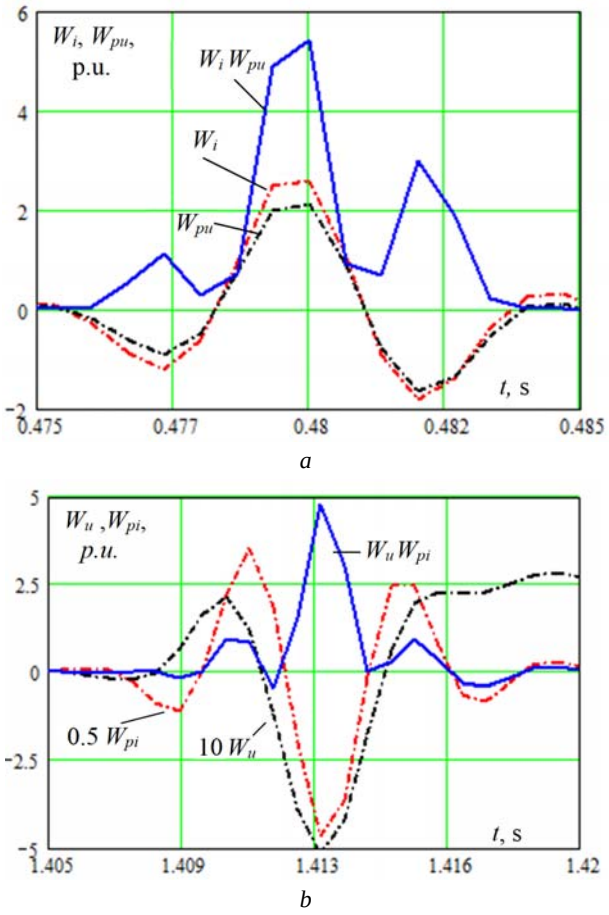

Fig. 3. Coefficients of wavelet transforms of current and voltage derivative (*a*), current derivative and voltage (*b*) and the component of reactive power obtained with their help

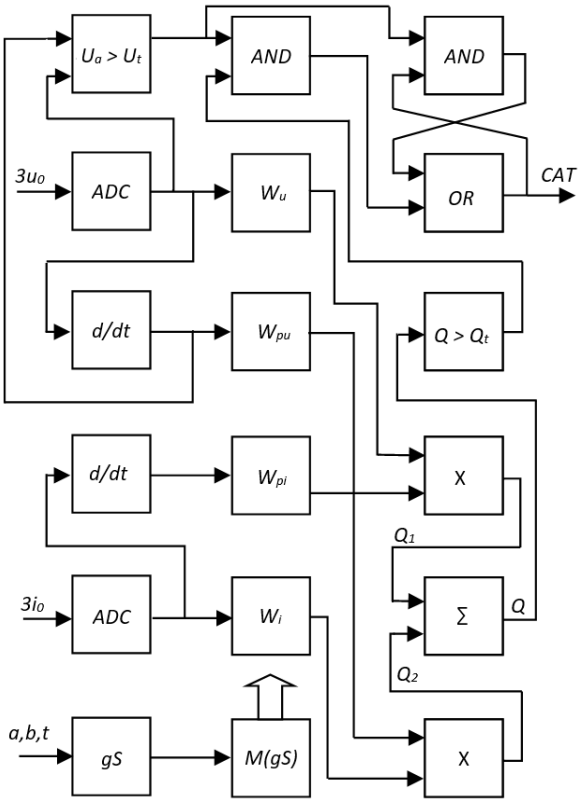

Fig. 4. Block diagram of the «wavelet-protection» algorithm against phase-to-ground fault

During the development of protection, the issue of increasing its speed by reducing the computational costs of wavelet transform was considered. It is established that for this purpose it is possible to use only fixed values $a = 8$, $b = 15$ for calculations by formula (5).

The results of the calculation of the resulting reactive power at the SEF with different initial voltages are shown in Fig. 5. From the given data it follows that the sensitivity of the developed protection in this case is 8 times higher than the sensitivity of the protection built on the basis of Fourier transforms, and the operation time of the protection is about 5-7 ms. The threshold value of reactive power is taken equal to the base value Q_b.

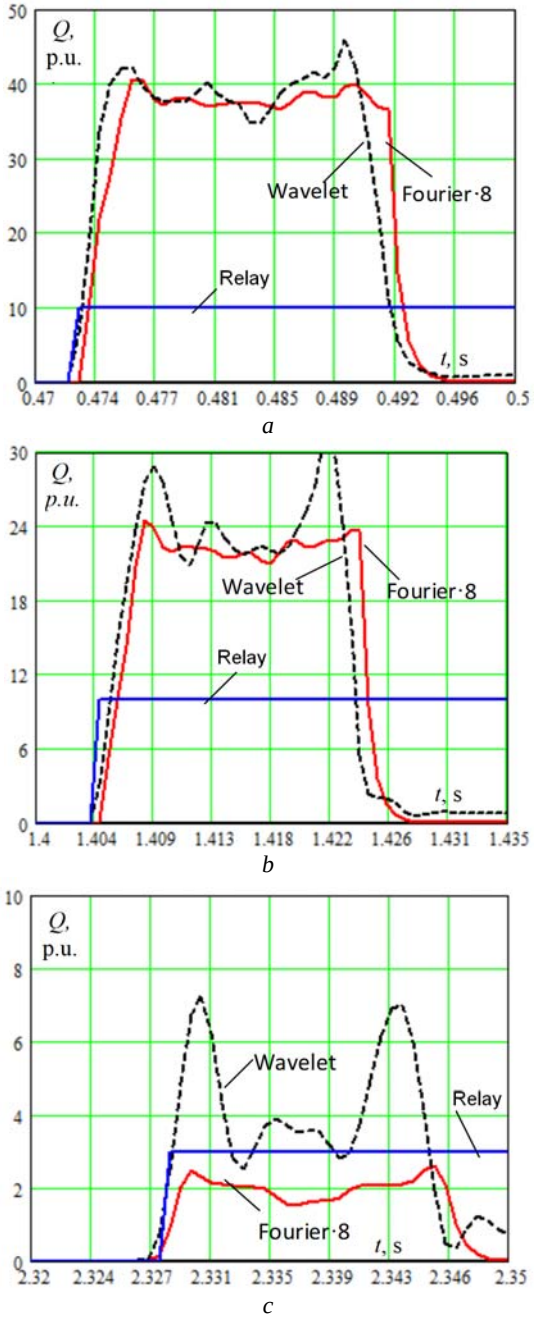

Fig. 5. Reactive power at the SEF determined by wavelet transform and Fourier transform at different initial voltages on the damaged phase:
u_{max} (*a*); 0.5 u_{max} (*b*); 0.01 u_{max} (*c*)

Using a mathematical model, the behavior of protection at different modes of occurrence of SEFs was studied: at resonant tuning of the reactor, over- and under-compensation, at different values of the initial voltage on the damaged phase and different resistances at the fault place. In all these modes there is a clear operation of the output body of the relay.

The lowest sensitivity of protection takes place (Fig. 5,*c*) at zero initial voltage. Compared to multifrequency protection based on Fourier transform [6], the developed protection has sensitivity almost an order of magnitude higher.

Positive results of protection operation were also obtained when the emergency files of the SEF recorded in the real operation were given to the input, as well as during the tests on the laboratory stand.

Conclusions.

1. The method of protection of electric grids with isolated or compensated neutral from phase-to-ground faults is improved and a new algorithm of realization of a method on the basis of use of wavelet transforms (WTs) of transient components of voltages and currents of zero sequence is developed that have experimental confirmation and allows to increase the efficiency of operation of electrical grids.

2. Using the coefficients of wavelet transforms, which are found by convolution of discrete values of current, voltage and their derivatives with the signals of the mother Morlet function, the reactive power is calculated, the positive value of which determines the damaged connection.

3. The efficiency of the protection algorithm is confirmed by the results of mathematical modelling and full-scale tests on a laboratory stand.

REFERENCES

1. Ghaderi A., Ginn H.L., Mohammadpour H.A. High impedance fault detection: A review. *Electric Power Systems Research*, 2017, vol. 143, pp. 376-388. **doi: 10.1016/j.epsr.2016.10.021.**

2. Farughian A., Kumpulainen L., Kauhaniemi K. Review of methodologies for earth fault indication and location in compensated and unearthed MV distribution networks. *Electric Power Systems Research*, 2018, vol. 154, pp. 373-380. **doi: 10.1016/j.epsr.2017.09.006.**

3. Gururajapathy S.S., Mokhlis H., Illias H.A. Fault location and detection techniques in power distribution systems with distributed generation: A review. *Renewable and Sustainable Energy Reviews*, 2017, vol. 74, pp. 949-958. **doi: 10.1016/j.rser.2017.03.021.**

4. Raza A., Benrabah A., Alquthami T., Akmal M. A Review of Fault Diagnosing Methods in Power Transmission Systems. *Applied Sciences*, 2020, vol. 10, no. 4, p. 1312. **doi: 10.3390/app10041312.**

5. Syvokobylenko V.F., Lysenko V.A. Earth fault protection for compensated electric networks based on frequency filters. *Naukovyi Visnyk Natsionalnoho Hirnychoho Universytetu*, 2020, no. 1, pp. 69-74. **doi: 10.33271/nvngu/2020-1/069.**

6. Syvokobylenko V.F., Lysenko V.A. Multifrequency protecting method against earth-faults of phase in the compensated electric networks. *Electrical engineering & electromechanics*, 2020, no. 1, pp. 56-60. **doi: 10.20998/2074-272X.2020.1.09.**

7. Wang Z., McConnell S., Balog R.S., Johnson J. Arc fault signal detection – Fourier transformation vs. wavelet

decomposition techniques using synthesized data. *2014 IEEE 40th Photovoltaic Specialist Conference (PVSC)*, 2014, pp. 3239-3244. **doi: 10.1109/PVSC.2014.6925625**.

8. Michalik M., Rebizant W., Lukowicz M.R., Lee S.-J., Kang S.-H. High-impedance fault detection in distribution networks with use of wavelet-based algorithm. *IEEE Transactions on Power Delivery*, 2006, vol. 21, no. 4, pp. 1793-1802. **doi: 10.1109/TPWRD.2006.874581.**

9. Elkalashy N.I., Lehtonen M., Darwish H.A., Taalab A.-M.I., Izzularab M.A. DWT-Based Detection and Transient Power Direction-Based Location of High-Impedance Faults Due to Leaning Trees in Unearthed MV Networks. *IEEE Transactions on Power Delivery*, 2008, vol. 23, no. 1, pp. 94-101. **doi: 10.1109/TPWRD.2007.911168.**

10. Syvokobylenko V.F., Lysenko V.A. Mathematical modeling of new algorithms for single-phase earth faults protection in a compensated electrical network. *Problemele Energeticii Regionale*, 2019, no.1-2(41), pp. 1-11. **doi: 10.5281/zenodo.3239135.**

Received 01.06.2020

V.F. Syvokobylenko[1], *Doctor of Technical Science, Professor,*
V.A. Lysenko[1], *Candidate of Technical Science,*
[1] Donetsk National Technical University,
2, Shybankova Square, Pokrovsk, Donetsk region, 85300, Ukraine,
e-mail: svf1934@gmail.com, viktor.lysenko@donntu.edu.ua

How to cite this article:
Syvokobylenko V.F., Lysenko V.A. Improving the efficiency of fault protection systems of electrical grids based on zero sequence voltages and currents wavelet transforms. *Electrical engineering & electromechanics*, 2020, no. 4, pp. 67-72. **doi: 10.20998/2074-272X.2020.4.09.**

Матеріали приймаються за адресою:
Кафедра "Електричні апарати", НТУ "ХПИ", вул. Кирпичова, 21, м. Харків, 61002, Україна
Електронні варіанти матеріалів по e-mail: a.m.grechko@gmail.com

Довідки за телефонами: +38 050 653 49 82 Клименко Борис Володимирович
+38 067 359 46 96 Гречко Олександр Михайлович

Передплатний індекс: 01216